Analytic solutions for linear waves propagating in an ocean with variable bottom topography and their applications in renewable wave energy

Fatimah Noor Harun
University of Wollongong

Analytic solutions for linear waves propagating in an ocean with variable bottom topography and their applications in renewable wave energy

Fatimah Noor Harun

A Thesis submitted for the degree of Doctor of Philosophy

School of Mathematics and Applied Statistic

University of Wollongong

August 2009

Declaration

In accordance with the regulations of the University of Wollongong, I hereby state that the work described herein is my original work, except where due references are made, and has not been submitted for a degree at any other universities or institutions.

Fatimah Noor Harun

August 2009

Abstract

Studies about ocean waves have been evolving over a period of time. Recently, there has been renewed interest in problems of refraction, diffraction and radiation of ocean waves around structures. In this thesis, the analytic solutions for linear waves propagating in an ocean with variable bottom topography and their applications in renewable wave energy are presented. In the first part, we present an analytic solution to the shallow water wave equation for long waves propagating over a circular hump. As a useful tool in coastal engineering, the solution may be used to study the refraction of long waves around a circular hump. It may also be used as a validation tool for any numerical model developed for coastal wave refraction. To validate the new analytic solution, we have compared our new analytical solution with a numerical solution obtained by using the finite difference method. The agreement between these two solutions is excellent. By using the analytic solution, the effect of the hump dimensions on wave refraction over the circular hump are examined.

In the second part of this thesis, based on the mild-slope equation derived by Smith and Sprinks [1] and the extended refraction-diffraction equation developed by Massel [2], we have constructed a two-layer mild-slope equation for interfacial waves propagating on the interface of a two-layer ocean model. First, we follow Smith and Sprinks's [1] approach to derive the mild-slope equation for the propagation of interfacial waves, with the higher-order terms proportional to the bottom slope and bottom curvature all being neglected. We then derived the extended version of the mild-slope equation with the higher-order terms included. While we were able to solve the first equation

analytically, we presented a numerical solution for the second equation. As a part of the verification process, both solutions were compared with each other and also with the single-layer mild-slope equation when the density of the upper layer goes to zero. We then used the new solution to study the effect of the hump dimensions on the refraction of the interfacial waves over a circular hump.

Finally, in the final section of this thesis, we have used what we have developed before to construct the two-layer mild-slope equation with free surface on top. By utilizing this equation, we then derived an analytic solution for long waves propagating over a circular hump with a hollow circular cylinder floating in the free surface. In order to validate our new analytic solution, we have compared our problem with Mac Camy and Fuchs [3] solution, because our solution has reduced to their solution when the lower water depth, h_2, goes to zero. We have also compared our solution with the flat bottom case in order to further verified our solution. Finally, by using the new solution, both diffraction and refraction effects from the hollow cylinder and hump dimensions are examined and discussed.

Acknowledgements

I would like to express profound gratitude to my supervisor, Prof. Song-Ping Zhu, for his invaluable support, encouragement, supervision and useful suggestions throughout this research work. His moral support and continuous guidance enabled me to complete my work successfully.

I would also like to thank all staff and fellow friends in School of Mathematics and Applied Statistics, especially Carolyn Silveri for helping me in Latex, Dr. Xiao-ping Lu for her help when I get some trouble in my calculations and Jean-Roch for his help in my programming.

Special thanks must go to my lovely husband, Mr. Fathy Kameel Mohd Fadzil for his encouragement and patience, my dear parent, Mr. Harun Mat and Mrs. Zaini Rasdi, and all my family members for their love and support throughout my life.

My indebtedness must be expressed to the financial support from Universiti Malaysia Terengganu, which allow me to pursue a Ph.D at The University of Wollongong.

Contents

List of Figures

List of Tables

Chapter 1

Introduction

Studies about ocean waves have been evolving over a period of time. Even though it is not a branch of new knowledge, many new theories, applications and technologies based on ocean waves have been discovered, developed and discussed among the researchers until today. Many unsolved problems, now can be solved using the new techniques and methods [4, 5].

In recent years, there has been a great deal of interest in solving various problem involving tsunamis. Tsunamis are a very large waves, included in long waves or shallow water waves categories. It is cause by earthquakes, the eruption of volcanoes and any other kind of land movement on the ocean floor such as landslide, explosion, impact etc [6]. In the deep ocean, the amplitude of the tsunamis are about half a meter, however, when these waves approach some obstacles such as an island, their amplitudes increase drastically due to decrease in depth. The most recent tsunami was recorded on December 26, 2004. It attacked coastlines of nearly every Indian ocean country and resulted in the largest toll of tsunami ever recorded. More than 225,000 people were killed and millions became homeless as an impact of this tragedy [7].

Due to undoubted practical importance in understanding the propaga-

tion of tsunami waves and their impact in human life, the research interest in studying this kind of waves have been renewed [8]. There is a lot of equations that already exist to model this kind of problem. Navier-Stokes equations are the first equations that govern the motion of tsunamis. However, it is difficult to solve a free-surface geophysical flows. Therefore, an approximations are introduced and resulting in a new equations such as nonlinear shallow water wave equation, Boussinesq equations and also Euler equations for the nonlinear regime. In the linear regime, some of the equations that have been used are the Hemholtz equation, the linear shallow water equation and the mild-slope equation.

In this thesis, we are interested in mild-slope equations. This equation was firstly derived by Berkhoff [9], which is a powerful tool to study the phenomenon of combined refraction-diffraction of ocean waves over a mild topography. The mild-slope equation has also been studied by many researchers since it was introduced, mainly due to its advantage in dimensionality reduction, i.e., by reducing a three-dimensional problem to a two-dimensional problem with the calculated velocity as an average velocity across the water column. For example, Johnson *et al.* [10] solved the mild-slope equation numerically for the diffraction and refraction around the island and later on, Smith and Sprinks [1], gave a formal derivation of the equation.

This thesis is organized as follows, in Chapter 2, the basic wave theory is presented to give a better understanding to the readers. The derivation given by Smith and Sprinks is also briefly presented in this chapter. Then, in Chapter 3, by using the mild-slope equation given by Smith and Sprinks [1], the analytical solution for long waves propagating over a circular hump is presented. The solution that obtained from this chapter can be used to study the refraction of long waves around a circular hump, as a useful tool in

coastal engineering. It may also be used as a validation tool for any numerical model develop for coastal wave refraction. For readers information, most of the work described in Chapter 3 have been published in Zhu and Harun [11].

Then, in Chapter 4, we constructed a two-layer mild-slope equation for interfacial waves propagating on the interface of a two-layer ocean model with rigid-lid approximation being imposed at the free surface. Replacing the free surface with a rigid-lid approximation is reasonable in many cases, especially at the regional ocean scale, because "internal-wave mode" only induces small deformation on the free surface and thus a rigid-lid approximation would exclude the fast mode associated with barotropic free surface waves and greatly simplify the theoretical analysis without loss of a great deal of accuracy. To constructed the equation for this chapter, first, we follow Smith and Sprinks' [1] approach to derive the mild-slope equation for the propagation of interfacial waves, with the higher-order terms proportional to the bottom slope and bottom curvature all being neglected. We then derive the extended version of the mild-slope equation with the higher-order terms included. While we were able to solve the first equation analytically, we present a numerical solution for the second equation. More literature and the significance of internal wave will be discussed in this chapter. Some details discussed in Chapter 4 are also given in Zhu and Harun [12] and Harun and Zhu [13].

The awareness of the importance of a renewable energy to substitute the existing energy resources in order to combat climate changes has made the study about ocean waves become very popular among the researchers. Ocean waves can produce a lot of energy through the process of refraction, diffraction, reflection and also shoaling. However, this energy could easily disappear due to friction and other waves processes. Therefore, the energy that comes from the ocean waves have to be captured, before it is gone to

waste. Having realized about this, more studies have been done to determine which methods and devices are suitable in order to capture and extract more energy from waves [14, 15].

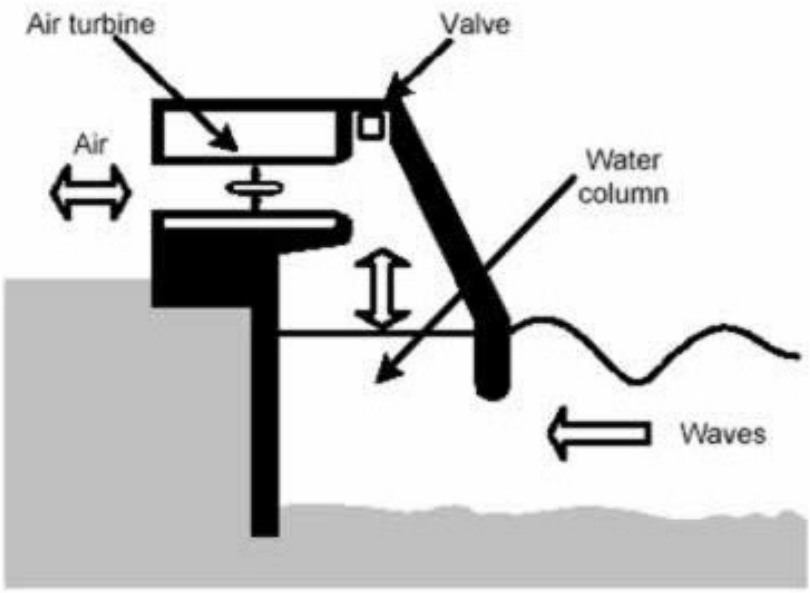

Figure 1.1: A definition sketch showing how an OWC works

One of the popular devices that can capture the energy from the waves is oscillating water column (OWC)[16]. The OWC consists of a partially submerged concrete or steel structure that has an opening to the sea below the waterline as shown in Fig. 1.1. It encloses a column of air above a column of water. As waves enter the air column, they cause the water column to rise and fall. This alternately compresses and depressurizes the air column. As the wave retreats, the air is drawn back through the turbine as a result of the reduced air pressure on the ocean side of the turbine. One of the company that have used and studied this device is Oceanlinx Limited Australia. This company has successfully installed this prototype at Port Kembla, NSW,

Australia as shown in Fig. 1.2. This device has successfully converted ocean wave energy into electricity in a number of tests being executed since it was installed.

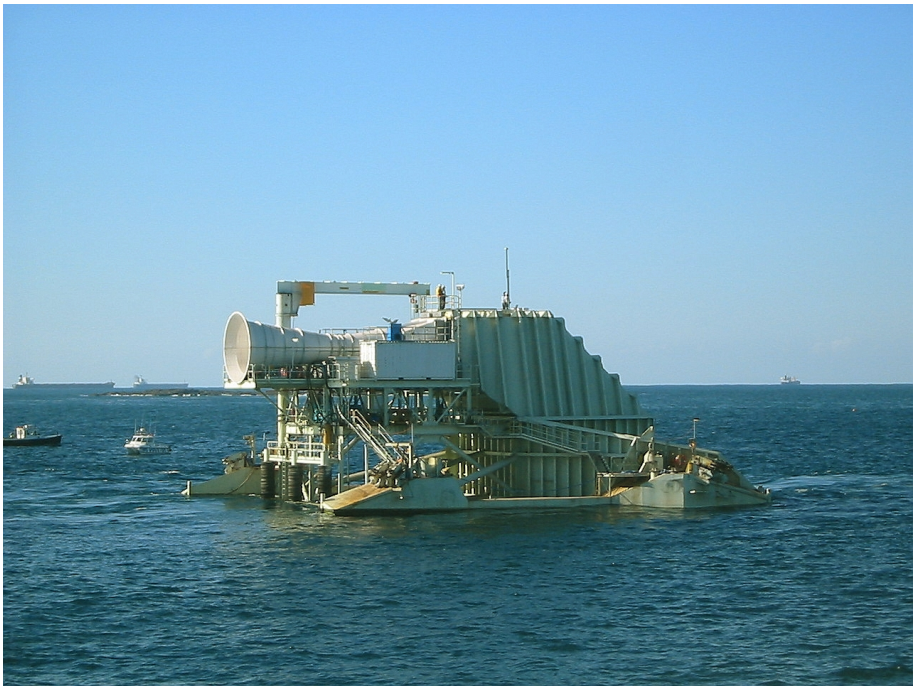

Figure 1.2: An OWC prototype locate at Port Kembla, NSW, Australia

Therefore, as the last object in this thesis, the mild-slope equation is further extended to be applied to the OWC problem. By removing the rigid lid approximation that we used in Chapter 4, the two-layer mild-slope equation for two-layer fluid with free surface on the top is derived. The reason that we have solved our problem using the two-layer model is, we need to satisfy all the boundary conditions that exist in this case. By using the two-layer fluid model, it is much easier to determine the boundary condition in both layers. Furthermore, by utilizing this equation, we then construct an analytic solution for long waves propagating over a circular hump located at the bottom of an ocean with a hollow circular cylinder floating on the top of the free

surface. Then, by using the new solution, we then discuss the effects of the hump dimensions and the hollow cylinder structures on the wave diffraction. The main findings in this chapter will be briefly summarized at the end of this chapter.

Finally, a summary of the work presented, together with the concluding remarks and suggestions for future research is concludes in Chapter 6 of this thesis.

Chapter 2

Basic Wave Theory

2.1 Introduction

Waves are very importance in our lives. They have an impact to anything that is near or in the body of water. For example, waves-induced currents can cause the erosion of the coastline as a result of the sand movement along the shore. It could also damage houses, destroy structures during the storms and even cause casualties when very large waves struck the coastlines. In the water, when very rogue waves occur especially during the bad weather, it can be very devastating too. A lot of people and ships have been missing due to the disastrous waves. On the other hand, the waves also can create a lot of activities for us, such as surfing. Furthermore, waves provide us with a source of renewable energy that has been actively studied recently.

Ocean wave theory is an attempt to explain the nature of ocean waves. Because the irregularity of these waves, it is hard to determine their true nature. There are many conditions which impact waves from local wind and ocean bottom structures to distant events like earthquake, tsunamis and storms. The speed, the length, the force and the magnitude of the object

impacting the water surface would create vast difference in the sizes of waves. Therefore, the linear wave equations and a number of assumption is used to help explain these waves with recognition that even with these assumptions, it may still not cover the totality of the explanation [17]. Thus, in the next section, the basic waves characteristics and equations for the linear waves are briefly discussed.

2.2 Basic Wave Characteristic

Ocean waves come in many shapes and sizes. They range in length from a fraction of a centimeter for the smallest ripples to half the circumference of Earth for the tides. They are formed by wind, gravitation, earthquakes, and submarine landslides disturbing the water surface. Once formed, and regardless of origin, ocean waves can travel great distances before reaching the coast. Ocean waves have characteristics that can be measured and used to describe each wave. Among the most useful of these are wave height,H, and wavelength, L. From these two parameters, we can determine the waves velocities, accelerations and all other parameters theoretically [5].

Fig. 2.1 shows the water waves characteristic for wave propagating in the x-direction. From this figure, the wavelength, L, is the horizontal distance measured between any two adjacent wave crests (wave crests that are next to each other) or any two adjacent wave troughs in a wave. The wave height, H, is the vertical distance between the crest and the trough of the waves. The wave period, T, is the time required for two consecutive crests or troughs to pass a particular point. From the wavelength, L, and wave period, T, we then can define the phase velocity, or celerity, C, as the wavelength, L divided by the wave period, T, because the waves are move in one wavelength

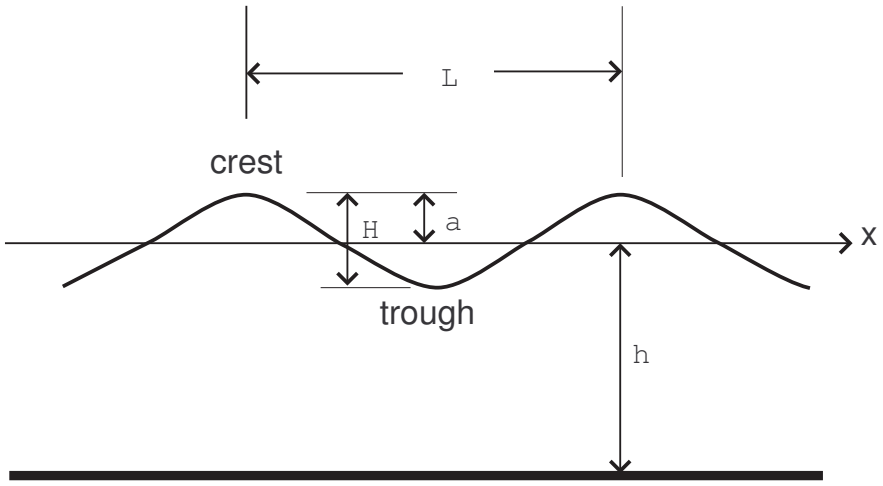

Figure 2.1: Waves characteristic

at a time.

There are four main waves phenomena that can occur during the propagation of the water waves. They are wave shoaling, diffraction, refraction and reflection. Shoaling and refraction of waves occur when the waves are in shallow water. Generally, when the water depth, h, is less than half of the wavelength, L, then the waves are considered to be in shallow water. When the waves move into shallow water, they begin to feel the bottom of the ocean.

Shoaling occurs as the waves enter shallower water. This significantly affects their motion and shape. As the wave speed and wavelength decrease in shallow water, the energy per unit area of the wave has to increase, so the wave height increases. The wave period remains the same in shoaling (the wave period is the time taken by a wave crest to travel the distance of one wave length). When the wave crest becomes too steep, it becomes unstable, curling forward and breaking. This usually happens when the height of the wave becomes about the same size as the local water depth.

The bending of the wave crest in response to changes in the wave speed, results in wave refraction. As waves travel from the deep water into the shallower water, the part of the waves in a shallow water moves slower than the part of the waves in a deeper water. This differential speed along the crest causes the wave to bend and wave direction changes. For example, as waves approach a straight shoreline at an angle, the water depth beneath the crest varies. It is because the speed of shallow water waves depends on the depth, different parts of the same crest, which lies at an angle to the shore and to the bottom contours, are traveling shoreward at various speeds.

Diffraction normally occurs when waves encounters an obstacle such as an even seabed. It involves a change in direction of waves as they pass through an opening or around a barrier in their path. Water waves have the ability to travel around corners, around obstacles and through openings. This ability is most obvious for water waves with longer wavelengths. The amount of diffraction (the sharpness of the bending) increases with the increase of the wavelength and decreases with the decrease of the wavelength. In fact, when the wavelengths of the waves are smaller than the obstacle, no noticeable diffraction occurs. Diffraction of water waves is observed in a harbor as waves bend around small boats and are found to disturb the water behind them. The same waves however are unable to diffract around larger boats since their wavelengths are smaller than the boat.

Like sound waves, surface waves can be bent (refracted) or bounced back (reflected) by solid objects. Waves do not propagate in a strict line but tend to spread outward while becoming smaller. Where a wave front is large, such spreading cancels out and the parallel wave fronts are seen traveling in the same direction. Where a lee shore exists, such as inside a harbour or behind an island, waves can be seen to bend towards where no waves are. In the

lee of islands, waves can create an area where they interfere, causing steep and hazardous seas. When approaching a gently sloping shore, waves are slowed down and bent towards the shore. When approaching a steep rocky shore, waves are bounced back, creating a 'confused sea' of interfering waves with twice the height and steepness. Such places may become hazardous to shipping in otherwise acceptable sea conditions.

2.3 Governing Equations for Water Waves

Consider now the problem which is depicted in Fig. 5.1 under a Cartesian Coordinate system in which x and y denote a pair of orthogonal horizontal coordinates and z denotes the vertical coordinate measured positively upward from the mean surface level (MSL). By assuming that the fluid is incompressible and the flow is irrotational, the governing equation for the wave field $\Phi(x, y, z, t)$, is the Laplace equation and can be written as

$$\frac{\partial^2 \Phi}{\partial z^2} + \nabla^2 \Phi = 0, \tag{2.1}$$

where Φ is defined as a velocity potential. The Laplace equation is an elliptic-type of the differential equation and to solve it we need the following conditions on all the boundaries of the domain:

$$\frac{\partial \Phi}{\partial z} + \nabla h \nabla \Phi = 0, \qquad z = -h(x, y) \tag{2.2}$$

$$\frac{\partial \zeta}{\partial t} + \nabla h \nabla \zeta = \frac{\partial \Phi}{\partial z}, \qquad z = \zeta(x, y, t) \tag{2.3}$$

$$\frac{\partial \Phi}{\partial t} + \frac{1}{2}[|\nabla \Phi|^2 + (\frac{\partial \Phi}{\partial z})^2] + g\zeta = 0 \qquad z = \zeta(x, y, t) \tag{2.4}$$

where h is the water depth and g is the gravity acceleration. This system of differential equations has nonlinear free surface boundary conditions, so it is

not possible to use standard technique to find an analytic solution. However, for simple harmonic motion with frequency ω, linearity of the problem allows separation of the time factor $e^{-i\omega t}$, and the Laplace equation (2.1) can be reduced to the two-dimensional version. In linear regime, the most powerful approximation is the mild-slope wave equation(MSWE), and in nonlinear regime, the most popular one is the Boussinesq equation.

2.4 The mild-slope equation

The mild-slope equation is one of the most powerful equation for solving a three-dimensional Laplace equation in the linear regime. This equation, which has a combining effects of diffractive and refractive, was originally proposed by Eckart [18], but with a shallow water restriction. Then, in 1967, Svendsen [19], rederived this equation independently in one dimension and later on, Berkhoff [9] presented this equation in two-dimension without restriction on the water depth. The mild-slope equation derived by Berkhoff [9] is a depth-integrated version of the Laplace equation. Since then, many researchers, such as Schonfeld [20], Jonsson *et. al.* [10], Smith and Sprinks [1], Lozano and Meyer [21], and Booij [22], have also studied this equation. To give a better understanding about mild-slope equation to our readers, the derivation of mild-slope equation given by Smith and Sprinks [1] is presented.

In the linear regime, for simple harmonic motion, the assumption that the wave slope $\epsilon = kA$ is small, i.e., $\epsilon \ll 1$ allows the separation of the time factor $e^{-i\omega t}$ from $\zeta(x, y, t)$ and $\Phi(x, y, z, t)$, i.e.,

$$\zeta(x, y, t) = \eta(x, y)e^{-i\omega t}, \qquad \Phi(x, y, z, t) = \phi(x, y, z)e^{-i\omega t}, \tag{2.5}$$

lead the Laplace equation in Eq. (2.1) and the nonlinear boundary condition

in Eqs. (2.2)-(2.4) to be simplified into

$$\frac{\partial^2\phi}{\partial z^2} + \nabla^2\phi = 0, \qquad -h(x,y) \le z \le 0 \tag{2.6}$$

$$\frac{\partial\phi}{\partial z} + \nabla h \nabla\phi = 0, \qquad z = -h(x,y) \tag{2.7}$$

$$\frac{\partial\phi}{\partial z} - \frac{\omega^2}{g}\phi = 0, \qquad z = 0 \tag{2.8}$$

By assuming that the water depth variation is moderate, i.e., $|\nabla h|/(kh) \ll 1$, the velocity potential may be written as

$$\phi(x,y,z) = \frac{ig}{\omega}\eta(x,y)f, \tag{2.9}$$

where

$$f = \frac{\cosh k(z+h)}{\cosh(kh)}, \qquad \omega^2 = gk\tanh(kh) \tag{2.10}$$

with f satisfying

$$\frac{\partial^2 f}{\partial z^2} - k^2 f = 0, \qquad -h(x,y) \le z \le 0 \tag{2.11}$$

$$\frac{\partial f}{\partial z} = 0, \qquad z = -h(x,y) \tag{2.12}$$

$$\frac{\partial f}{\partial z} - \frac{\omega^2}{g} f = 0, \qquad z = 0 \tag{2.13}$$

where k is a wave number. Considering Eq. (2.6) as an ordinary differential equation in z, and applying Green's formula for ϕ and f, and using Eqs. (2.6) - (2.8) and (2.11) - (2.13), we obtain

$$\int_{-h}^{0} (k^2\phi f + f\nabla^2\phi)dz = -(f\nabla h \cdot \nabla\phi)_{-h} \tag{2.14}$$

By invoking Eqs. (2.9) and (2.10) and calculating $\nabla\phi$ and $\nabla^2\phi$, and inserting in Eq. 2.14), we have

$$\begin{aligned}
&\int_{-h}^{0}[f^2\nabla^2\eta + 2f\frac{\partial f}{\partial h}\nabla\eta\cdot\nabla h \\
&+\eta f\frac{\partial^2 f}{\partial h^2}(\nabla h)^2 + \eta f\frac{\partial f}{\partial h}\nabla^2 h + k^2\eta f^2]dz \\
&= -\nabla h\cdot\nabla\eta f^2|_{-h} - \eta(\nabla h)^2 f\frac{\partial f}{\partial h}|_{-h}
\end{aligned} \tag{2.15}$$

Since $|\nabla h|/(kh) \ll 1$, all the higher order terms $(\nabla h)^2$ and $\nabla^2 h$ can be neglected and we can rewrite Eq (2.15) as

$$\nabla\cdot[(\int_{-h}^{0} f^2 dz)\nabla\eta] + k^2(\int_{-h}^{0} f^2 dz)\eta = 0 \tag{2.16}$$

this equation also can be written as

$$\nabla\cdot(CC_g\nabla\eta) + k^2 CC_g\eta = 0 \tag{2.17}$$

where

$$C = \sqrt{\frac{g}{k}\tanh(kh)} \tag{2.18}$$

$$C_g = \frac{C}{2}(1 + \frac{2kh}{\sinh(2kh)}) \tag{2.19}$$

are the phase velocity and the group velocity, respectively.

Eq. (2.17) is known as the mild-slope equation. This equation can be reduced to the linear shallow water equation,

$$\nabla\cdot(h\nabla\eta) + \frac{\omega^2}{g}\eta = 0 \tag{2.20}$$

because the phase velocity, C and group velocity, C_g, have reduced to $C = C_g = \sqrt{gh}$ and $\omega^2 \approx k^2 gh$ in shallow water.

On the other hand, for short waves or in deep water, Eq. (2.17) reduces to Hemholtz equation

$$\nabla^2 \eta + k^2 \eta = 0 \tag{2.21}$$

with the assumption $C \approx \sqrt{\frac{g}{k}}$, $C_g \approx \frac{1}{2}C$, and $\omega \approx \sqrt{gk}$ in deep water.

By utilizing the mild-slope equation presented in this chapter, we have further extended this equation to solve the two-layer fluid with the rigid lid assumption being imposed on the free surface in Chapter 4. Furthermore, we have also added the higher-order terms that was neglected before in our solution to study the influence of the terms in our solution. Both derivations are discussed in Chapter 4 of this thesis. Finally, in Chapter 5, by removing the rigid-lid assumption on the free surface, the mild-slope equation in two-layer fluid model with free surface on top is presented.

Chapter 3

Long Wave Refraction Over a Circular Hump

3.1 Overview

On December 26, 2004, a never-forgotten tsunami attacked the coastlines of nearly every Indian Ocean countries and resulted in the largest toll of tsunami ever recorded. According to Geist *et. al.* [7], more than 225,000 people were killed within a matter of hours and millions became homeless as a result of this tragedy. Since then, the research interest in studying long waves propagating in shallow water, such as tsunami, has been renewed [8].

Studies on long waves propagating over waters of variable depth have been conducted by many researchers for more than five decades. Some of the previous studies include Homma [23] who obtained an analytical solution in 1950 for the scattering of long waves around a cylindrical island mounted on a parabolic shoal. An exact solution was given by MacCamy and Fuch [3] for plane waves diffracted by a large surface-piercing vertical circular cylinder in an open sea of constant depth.

In early 1970s, Berkhoff [9] derived a two-dimensional equation which describes the phenomenon of combined refraction-diffraction for simple harmonic waves and also a method to solve it. Jonsson *et. al.* [10] then solved the mild-slope equation [9] numerically for the diffraction and refraction around the island studied by Homma [23]. Based on the mild-slope equation initially derived by Berkhoff, Bettess and Zienkiewicz [24] proposed a general approach to solve wave diffraction and refraction problems numerically using finite and infinite elements.

In early 1990s Zhang and Zhu [25] derived analytical solutions for the propagation of long surface waves around a conical island and over a paraboloidal shoal, based on the linearized long-wave equation. Then in 1996, Zhu and Zhang [26] derived another analytical solution for scattering of simple harmonic waves by a cylindrical island mounted on a conical shoal in an otherwise open sea of constant depth based on shallow water wave theory. Recently, Yu and Zhang [27] further extended Zhu and Zhang's [26] approach and presented an analytic solution for the wave motion with combined refraction and diffraction around a circular island mounted on the top of a hyperparabolic shoal.

There are also several authors who have experimentally studied the wave propagation over a shoal before. However, most of them concentrated on the short waves or irregular waves. For example, Ito and Tanimoto [28] conducted an experiment for the short waves propagating over a shoal and Williams *et. al.* [29] solved the same problem numerically using the finite difference method. On the other hand, Panchang *et. al.* [30] and Chawla *et. al.* [31] focused on the propagation of irregular and breaking waves over a circular shoal.

More recently, Suh *et. al.* [32] developed an analytical solution for long

waves propagating over a circular, bowl-shaped pit located on the floor of an ocean with otherwise constant water depth. In fact, their solution was an extension of Lamb's [33] solution for a hemisphere with specific values of the coefficients in the first two terms of Lamb's series solution. In order to verify their solution, Suh *et. al.* [32] constructed a numerical solution based on a similar finite difference method used by Copeland [34], and they found that their results with the analytical solutions were nearly identical.

In this chapter, we present an analytical solution for long waves propagating over a circular hump. The solution technique that we have adopted in order to solve this problem is similar to that given by Suh *et. al.* [32]. However, the different bottom geometry in our case has introduced some additional difficulties in the solution process and care must be taken before a final solution can be worked out. In addition, we have also worked out a numerical solution for long waves propagating over a circular hump in the variable depth region using the finite difference method. In Section 3.2, we derived an analytic solution for long waves propagating over a circular hump. Then, in Section 3.3, an example is presented to compare our new analytic solution with Suh *et. al.*'s [32] solution. As a part of the verification process, we have also compared our new analytical solution with a numerical solution obtained by using the finite difference method. Utilizing the new solution, we then discussed the effects of the hump dimensions on the wave refraction. Finally, the main findings in this chapter are briefly summarized in the last section.

3.2 Analytic solution

Consider a train of plane waves which propagate in an open sea of constant depth h_1 and is refracted by an axi-symmetric hump-shaped shoal located on the ocean floor. The cross-section of the hump is of the shape of a parabola and the surface of the hump is formed through revolving the parabola around the vertical axis of revolution, which is marked with the z coordinate of a Cartesian coordinate system chosen with its origin located at the center of the hump as demonstrated in Fig. 3.1. The parabolic hump surface intersects with the ocean floor at $z = 0$, resulting a circle with its radius denoted as b. The maximum height of the hump is controlled by a parameter h_0, which simply denotes the still water depth right above the point of maximum hump height as shown in Fig. 3.1. In the corresponding cylindrical coordinate system with r being the radial distance from the origin and θ being the angle measured counterclockwise from the positive x-axis, the water depth is prescribed by a parabolic function

$$h = \begin{cases} h(r) = h_0(1 + \frac{r^2}{a^2}), & r < b, \\ h_1 = h_0(1 + \frac{b^2}{a^2}), & r \geq b. \end{cases} \tag{3.1}$$

in which a is determined by $a = b\sqrt{\frac{h_0}{h_1 - h_0}}$, for a given set of h_1 and h_0, with $h_0 \neq 0$ and $a > b$. Therefore, geometrically, a is the radius of the cross-sectional circle of the paraboloid intersecting with a horizontal plane located below the seabed. While h_0 is used to control the height of a hump, either b or a is used to control the horizontal dimension of the hump. The steepness of a hump is then represented by the ratio of h_0/b.

The propagation of water waves over a topography with gentle variation can be modeled by the mild-slope equation, which is a depth-integrated version of Laplace equation [9] and has been studied by many researchers since

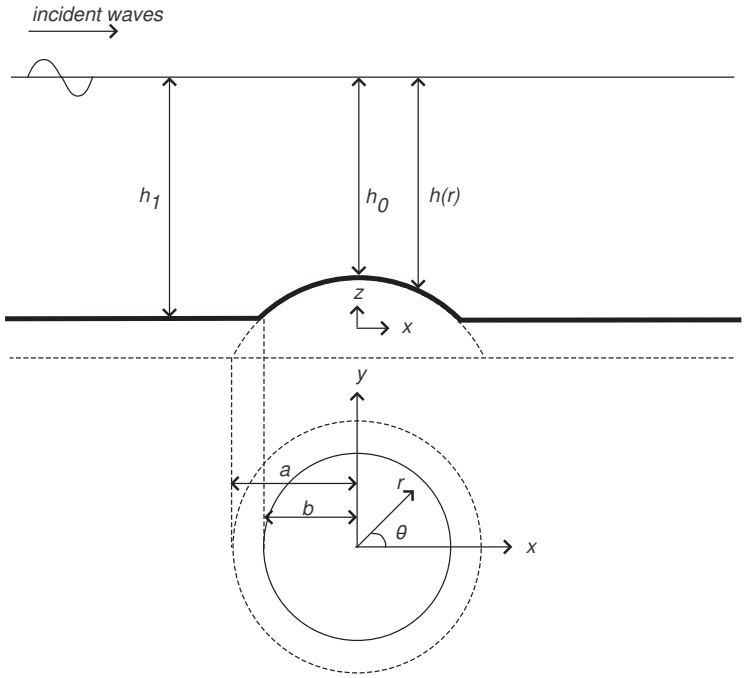

Figure 3.1: A definition sketch of a hump located on the floor of an ocean with otherwise constant water depth (top figure: side view, bottom figure: top view)

it was originally derived by Berkhoff in 1972. This is mainly due to its advantage in reducing a three-dimensional problem to a two-dimensional problem. With the water surface elevation, η, being expressed as a complex variable, the mild-slope equation is written as

$$\nabla \cdot (CC_g \nabla \eta) + k^2 CC_g \eta = 0, \tag{3.2}$$

where C is the phase speed, C_g the group velocity and ∇ is a horizontal gradient operator $(\frac{\partial}{\partial x}, \frac{\partial}{\partial y})$. If we further assume that the incident waves are long in wavelength in comparison with the constant water depth h_1, this equation can be reduced to long (shallow water) waves equation which is of

the form

$$\nabla \cdot (h\nabla\eta) + \frac{\sigma^2}{g}\eta = 0, \tag{3.3}$$

under the long waves assumptions $C \cong C_g \cong \sqrt{gh}$ and $\sigma^2 \cong gk^2h$, where g is the gravitational acceleration, h is the local water depth, σ is the angular velocity of the incident plane waves and k is the wave number.

Under the polar coordinates, Eq. (3.3) can be written as

$$h(\frac{\partial^2\eta}{\partial r^2} + \frac{1}{r}\frac{\partial\eta}{\partial r} + \frac{1}{r^2}\frac{\partial^2\eta}{\partial\theta^2}) + \frac{\mathrm{d}h}{\mathrm{d}r}\frac{\partial\eta}{\partial r} + \frac{\sigma^2}{g}\eta = 0. \tag{3.4}$$

This equation can be solved using the method of separation of variables with η being of the form

$$\eta(r,\theta) = R(r)\Theta(\theta). \tag{3.5}$$

Upon substituting Eq. (3.5) into Eq. (3.4), we can obtain the eigen-function in the θ as

$$\Theta_n = C_{1n}\cos n\theta + C_{2n}\sin n\theta, \tag{3.6}$$

where C_{1n} and C_{2n} are arbitrary constants.

We divide the fluid domain on the r-θ plane into two subdomains: a region with variable water depth ($r < b$) and the remaining region with constant water depth ($r \geq b$).

In the far field, the undisturbed long-crested incident waves propagate towards the positive x- direction and its surface elevation is given by [4]:

$$\eta_0 = a_i e^{ikx}, \tag{3.7}$$

where a_i is the incident wave amplitude and $i = \sqrt{-1}$. Eq. (3.7) can be expanded as

$$\eta_0 = a_i \sum_{n=0}^{\infty} i^n \varepsilon_n J_n(kr)\cos n\theta, \tag{3.8}$$

where J_n is the Bessel function of the first kind of order n, and ε_n is the Jacobi symbol defined by

$$\varepsilon_n = \begin{cases} 1, & n = 0, \\ 2, & n \geq 1. \end{cases} \tag{3.9}$$

In the constant depth region ($r \geq b$), the general solution is well known [3], and is given by

$$\eta_1 = \eta_0 + \sum_{n=0}^{\infty} D_n H_n^{(1)}(kr) \cos n\theta, \tag{3.10}$$

where D_n is a set of complex constants yet to be determined, and $H_n^{(1)}$ is the Hankel function of the first kind of order n.

In the near field, the water depth is varying and we need to solve Eq. (3.4). By substituting Eq. (3.1) into Eq. (3.4) and solving the resulting equation, we can obtain a differential equation for $R_n(r)$ of each wave mode n to be satisfied as

$$(a^2 + r^2)r^2 \frac{\mathrm{d}^2 R_n}{\mathrm{d}r^2} + (a^2 r + 3r^3)\frac{\mathrm{d}R_n}{\mathrm{d}r} + (v^2 r^2 - n^2 a^2 - n^2 r^2)R_n = 0, \tag{3.11}$$

where v is defined as

$$v = \frac{\sigma a}{\sqrt{g h_0}}. \tag{3.12}$$

Eq. (3.11) then can be solved using the method of Frobenius [35]:

$$R_n(r) = \sum_{m=0}^{\infty} \alpha_{m,n} r^{m+c}, \tag{3.13}$$

with $\alpha_{0,n}$ being unity and c being a constant to be determined by the indicial equation. As shown in [35], the series solution converges when $r < a$. Therefore, the solution always converges in the hump region with $r < b$. Solving Eq. (3.11) using the method of Frobenius, we obtain the indicial equation, $c^2 - n^2 = 0$, which yields two roots:

$$c = \pm n. \tag{3.14}$$

These two distinct roots of the indicial equation lead to two sets of linearly independent solutions:

$$R_{n,1} = \sum_{m=0}^{\infty} \alpha_{m,n} r^{m+n}, \tag{3.15}$$

$$R_{n,2} = R_{n,1} \ln r + \beta_{m,n} r^{m-n}. \tag{3.16}$$

The imposition of the regularity condition at $r = 0$ differs the current solution from Suh *et. al*'s solution. The condition that water surface elevation must be finite at the origin implies that $R_{n,2}$ has to be discarded. Otherwise, the solution would be singular at $r = 0$.

Now, substituting Eq. (3.13) with $c = n$ into Eq. (3.11) and collecting the terms of the same order of r, we obtain

$$\alpha_{1,n} = 0, \tag{3.17}$$

$$\alpha_{m+2,n} = \frac{-[(m+n)(m+n+2) + v^2 - n^2]}{a^2(m+2)(m+2n+2)} \alpha_{m,n}, \tag{3.18}$$

and $m = 0, 1, 2, ...$

Finally, the water surface elevation for long waves over a hump can be written as

$$\eta = \sum_{n=0}^{\infty} A_n R_n (C_{1n} \cos n\theta + C_{2n} \sin n\theta), \tag{3.19}$$

where A_n, C_{1n} and C_{2n} are arbitrary constants to be determined. One should note that there is no need to have A_n as an arbitrary constant in addition to the introduction of two arbitrary constants C_{1n} and C_{2n}. However, the reason we did this is for the easiness of comparing our solution with that of Suh *et. al.* [32], who used this additional constant A_n at this stage of the derivation. For the general solution in the finite region with variable depth $r < b$, the water surface elevation can be written as:

$$\eta_2 = \sum_{n=0}^{\infty} B_n R_n \cos n\theta, \tag{3.20}$$

where $B_n = A_n C_{1n}$ is a set of complex constants to be determined. The terms associated with $\sin n\theta$ in Eq. (3.19) have been dropped based on the symmetry condition.

The solutions in two sub-regions must be matched on the common boundary $r = b$ to ensure the continuity of wave heights and the hydrodynamic pressure across it [5]. At $r = b$, the dynamic and kinematic matching conditions are

$$\eta_1 = \eta_2, \tag{3.21}$$

$$\frac{\partial \eta_1}{\partial r} = \frac{\partial \eta_2}{\partial r}. \tag{3.22}$$

Therefore, from Eqs. (3.10), (3.20) - (3.22), the coefficients B_n and D_n can be determined as

$$B_n = a_i k i^n \varepsilon_n \frac{J_n(kb)H_n'^{(1)}(kb) - J_n'(kb)H_n^{(1)}(kb)}{kR_n(b)H_n'^{(1)}(kb) - R_n'(b)H_n^{(1)}(kb)}, \tag{3.23}$$

$$D_n = a_i i^n \varepsilon_n \frac{kJ_n'(kb)R_n(b) - J_n(kb)R_n'(b)}{H_n^{(1)}(kb)R_n'(b) - kH_n'^{(1)}(kb)R_n(b)}, \tag{3.24}$$

in which the primes denote the derivatives with respect to the argument. By substituting back these coefficients into Eqs. (3.10) and (3.20), the water surface elevation for the entire domain can be computed. Some results of specific calculations are presented in the next section.

3.3 Results and discussions

In this section, firstly, we present an example to compare our new analytic solution with the Suh *et. al.*'s [32] solution. Then, we compare our solution with a numerical solution obtained by using the finite difference method, as part of the verification process. Lastly, using the new solution, we discuss the effect of hump dimensions on the wave refraction process over a hump.

3.3.1 *Comparison with the circular pit*

Since the bottom shape in our case is exactly the same as that used in Suh *et. al.* [32], except they are the mirror reflection of each other, i.e. the pit has now become a hump, it would be very interesting to compare the two different refraction processes subject to the same incident waves.

However, if we try to do a direct flip over of the Suh *et. al.*'s profile while other parameters are kept the same, we run into problems. In Suh *et. al.*'s configuration, the water depth in the far field is 3.2 m, which is the same as the maximum depth of their pit. If this pit is flipped by 180^o to become a hump, the water depth right above the center of hump would become zero. Clearly, this means that if we want to have a direct comparison with their solution, we are forced to increase the water depth in the far field, resulting in a comparison that only serves the purpose of verification of our new solution. A much more meaningful comparison with physical significance is to adopt a much smaller size of bowl pit, and thus when it is flipped into a hump, the water depth directly above the hump is still much larger than the maximum height of hump. Such a case will be discussed later.

Therefore, in the first example presented here, we compare Suh *et. al.*'s [32] case with a case in which the hump is created by flipping their bowl pit 180^o and in the mean time, raise the constant water depth, h_1, to 4.8 m (the corresponding relative water depth becomes $k_1 h_1 = 0.167$). The rest of the parameters are set exactly the same as that for the pit case discussed in Suh *et. al.*'s [32] case, i.e., $b/L = 0.5$, the wavelength, $L = 120.4$ m.

Since, the analytic solution for η involves an infinite series, it must be truncated, for the purpose of numerical calculations. To have a meaningful comparison with Suh *et. al.* [32], we truncated our series solution in exactly the same way as they did, i.e., to set N= 70 and M= 30. Fig. 3.2 shows the

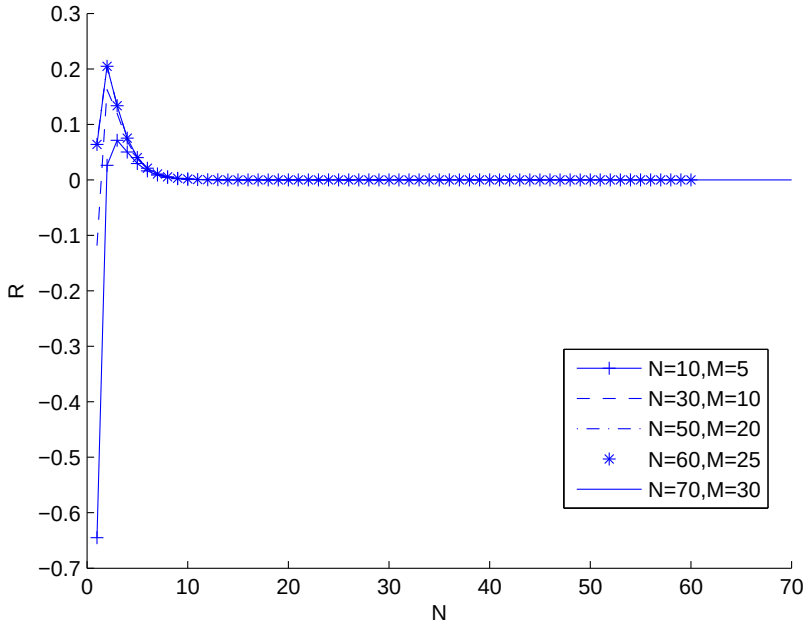

Figure 3.2: Convergence test for Frobenius series solution

convergence of the Frobenius series solution test for various values of N and M until it converged at the desired values. The Bessel and Hankel functions in the analytical solution were computed using the built-in subroutines in MATLAB.

Fig. 3.3 and Fig. 3.4 are the contour plots of the relative wave amplitudes (i.e. the wave amplitude relative to the incident amplitude) for long waves propagating over the hump and the circular bowl pit, respectively. The results in this comparison are presented in terms of dimensionless coordinates, x/L and y/L. The centers of the pit and the hump are located at the origin and the contour lines in the each plot show the values of the relative wave amplitude. As can be seen, the wave patterns are quite different for these two cases. For example, refraction effects for the hump case is weaker than those for the bowl pit case. The primary reason for this phenomenon is, the

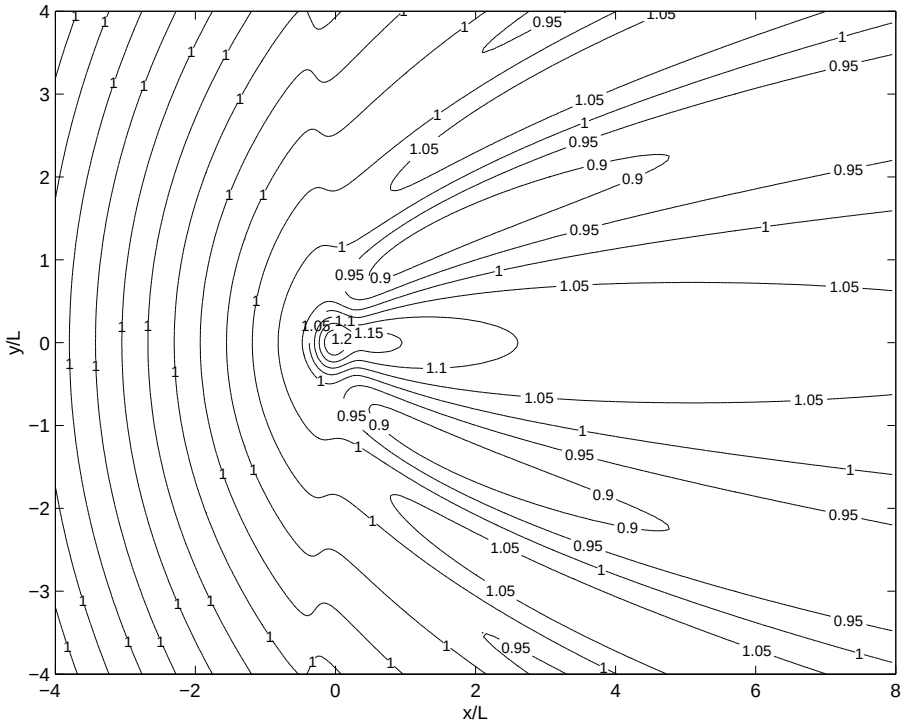

Figure 3.3: Contour plots of relative wave amplitude for waves propagating over a hump

water depth for the latter case is much larger, resulting a stronger diffraction.

We have also plotted out the relative wave amplitudes along the x- and y-axis, respectively, in Figs. 3.5 and 3.6. As expected, waves are amplified behind a hump, whereas there is a great suppression of waves behind a pit (see Fig. 3.5). Physically, this shows that the region behind a pit can be taken as if it was a harbor, whereas if a wave-energy conversion device is to be mounted, it would be far better to place it behind a hump. We also observed that behind the disturbance (i.e., the hump and pit in each case respectively), the relative wave amplitudes for both cases are no longer oscillating. Rather, they gradually reduce (for the hump case) or increase (for the pit case) towards the unity, which is supposed to be the relative wave amplitude far downstream.

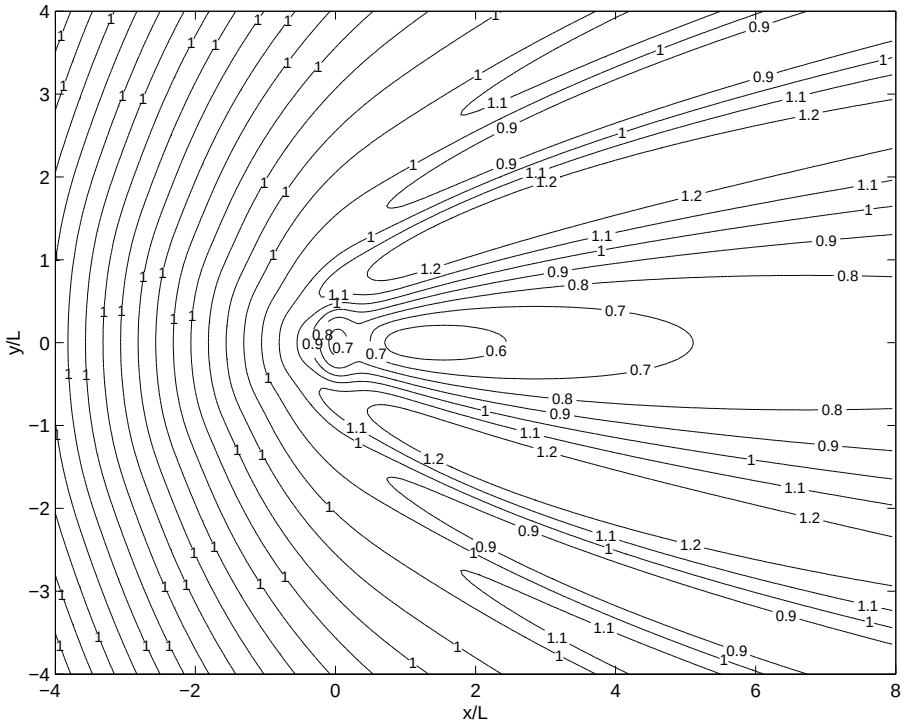

Figure 3.4: Contour plots of relative wave amplitude for waves propagating over a pit

Furthermore, from Fig. 3.6, one can clearly see that the variations of relative wave amplitude for these two distinct cases along the lateral direction are out of phase, which naturally corresponds to the system's response to the 180^o flip over of the bottom topography.

Next, we shall make a direct comparison of the influences of hump and pit to the wave refraction process by keeping all the physical conditions the same, except a pit is replaced by a hump. To do that, we have to choose a new set of parameters. The new set of parameters we chose are $h_1 = 3.2$ m, $b/L = 0.5$ and the maximum height for both shapes is set to 0.8 m. Therefore the value of h_0 for the pit case becomes 4.0 m, while it is 2.4 m for the hump case.

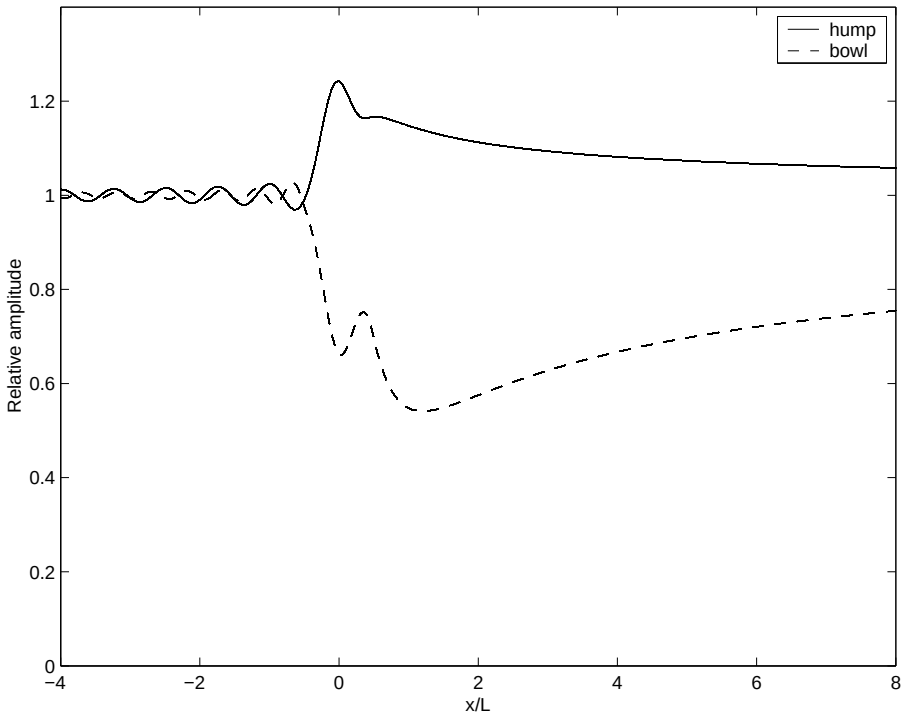

Figure 3.5: Comparison of relative wave amplitudes along the x-axis

Figs. 3.7 and 3.8 show the contour plots of the relative wave amplitudes generated with the new set of parameters for long waves propagating over the hump and the bowl pit, respectively.

To make a better comparison, we have also plotted out the relative wave amplitude along the $x-$ and $y-$ axis, respectively, in Figs. 3.9 and 3.10. From these two figures, one should notice that the relative wave amplitudes for these two physically completely opposite cases are almost symmetrical about the undisturbed free surface. For example, from Fig. 3.10, the relative wave amplitudes at the lateral cross section $x = 0$ for both solutions seem to be almost mirror reflection of each other. However, in the longitudinal cross section $y = 0$, the mirror reflection effects are not as strong as those in the lateral cross section $x = 0$; the maximum drop of the relative wave

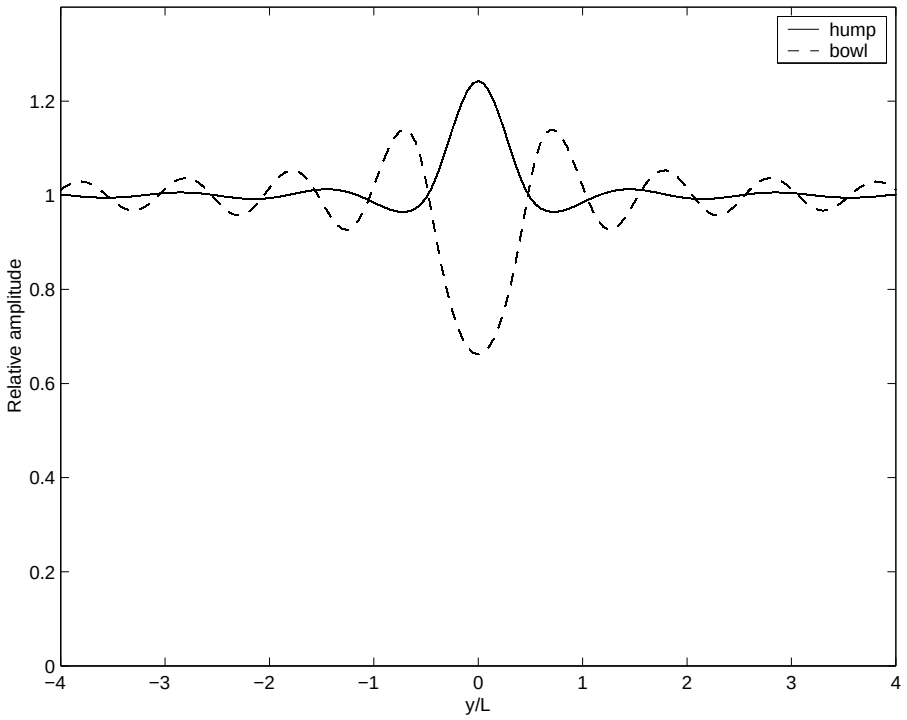

Figure 3.6: Comparison of relative wave amplitudes along the y-axis

amplitude for waves propagating over the pit case is now smaller than the maximum rise of the relative wave amplitude for the hump case. Therefore, we can conclude that, by using all the same of physical conditions, except the bottom profile being flipped over by 180^o, almost symmetrical relative wave amplitudes are obtained, which is within our expectation.

3.3.2 *Comparison with a numerical solution*

For the purpose of validation, the new analytic solution is also compared with a numerical solution.

Because in the outer region ($r \geq b$), or the constant depth region, the wave propagation is dictated by the incident waves from far left, the solution is already known [3] and is given in Eq. (3.10), we only need to solve Eq.

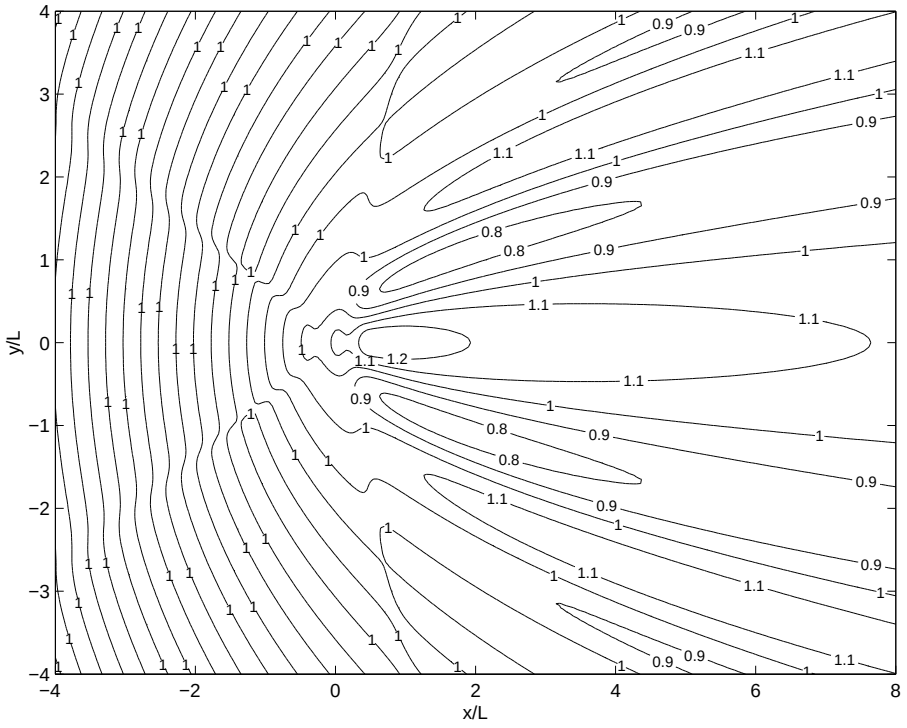

Figure 3.7: Contour plots of relative wave amplitude for waves propagating over a hump

(3.11) in the inner region ($r < b$) numerically. This equation is only a second-order linear ordinary differential equation, which can be easily solved numerically using the $2nd$-order central finite difference scheme, with two boundary conditions being imposed at the center of the region $r = 0$ and the outer boundary of the region $r = b$. At $r = 0$, the boundary condition is

$$\frac{dR_n}{dr} = 0, \tag{3.25}$$

which reflects the fact that the slope of the wave elevation at the origin must be continuous. The boundary condition at $r = b$ can be determined from the matching conditions Eq. (3.21) and (3.22).

Fig. 3.11 and Fig. 3.12 show the comparison between the analytic and numerical solutions for the case of $h_1 = 4.8$ m, $h_0 = 3.2$ m, $a/L = \sqrt{0.5}$,

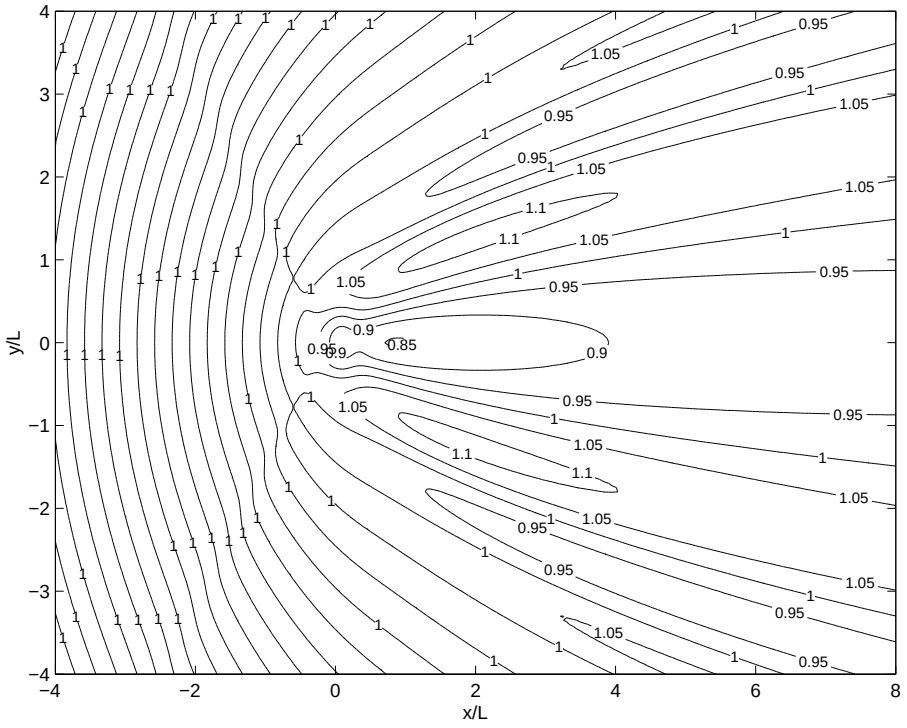

Figure 3.8: Contour plots of relative wave amplitude for waves propagating over a pit

$b/L = 0.5$, and the center of the hump is located at the origin along the $x-$ and $y-$axis, respectively. The numerical results were obtained with the grid spacing $\Delta r = 0.025$ m, when two solutions became hardly distinguishable. With the excellent agreement between the analytic and numerical solutions, as displayed in Fig. 3.11 and Fig. 3.12, we are confident that the derivation of our new analytical solution is correct.

3.3.3 *Effect of the hump size*

In this section, we discuss the effect of the hump size to the wave refraction when the radius and the maximum height of the hump are varied. As mentioned in Section 2, instead of using the value of $h_1 - h_0$ to specify the height

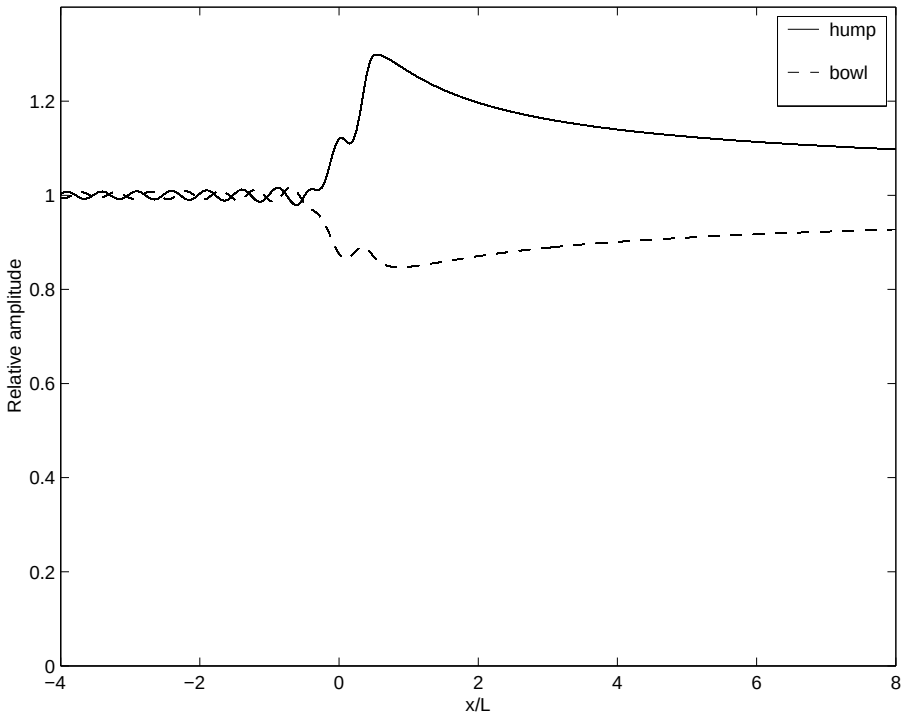

Figure 3.9: Comparison of relative wave amplitudes along the x-axis

of a hump, we used h_0 to control the height of a hump (cf, Fig. 3.1). This implies that for a fixed h_1, a smaller value of h_0 results in a larger hump height and a larger value of h_0 corresponds to a smaller hump height. In other words, both h_1 and h_0 are independent input parameters; when h_1 is changed to a different value, h_0 does not have to change accordingly. This is different from a traditional specification in which the hump height is given, independent from the value of h_1. Our specification of hump height with the values of both h_1 and h_0 involved is from the convenience of describing the hump shape profile with Eq. (3.1). So, to test the effect of the hump size, we have varied the hump height via changing h_0 while holding h_1 as well as all other parameters constant.

Fig. 3.13 and Fig. 3.14 show the relative wave amplitude along the x- and

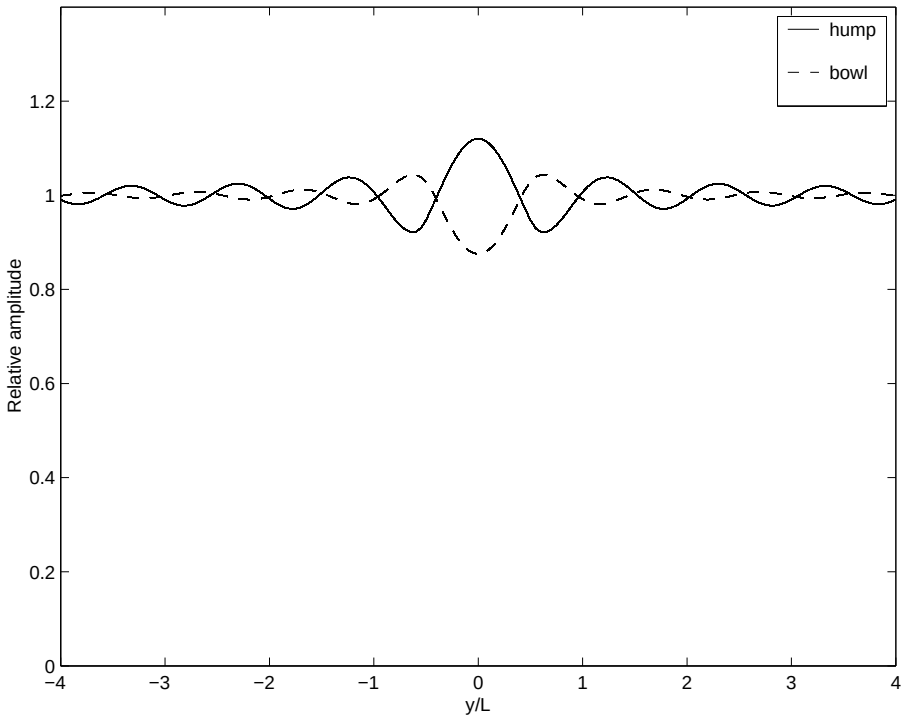

Figure 3.10: Comparison of relative wave amplitudes along the y-axis

y-axis, respectively, for the cases of $h_0 = 2.2$, 3.2 and 4.2 m with the hump radius being fixed at $b/L = 0.5$ and $h_1 = 4.8$ m. It is clearly seen that, as the height of the hump increases, the relative wave amplitude becomes larger, which is as expected. For example, along the x- axis, as we increase the water depth by 31.25% from 3.2 m to 4.2 m, the maximum value of relative wave amplitude has decreased by approximately 4.84%. In contrast, when the water depth is decreased by the same percentage from 3.2 m to 2.2 m, the maximum value of relative wave amplitude increases by about 8.87%, which is almost twice of the total percentage change of the relative wave amplitude as the case before. This shows that there is bias towards the reduction of water depth, as the refraction effects appear to have been amplified much more with an increase of the height of a hump.

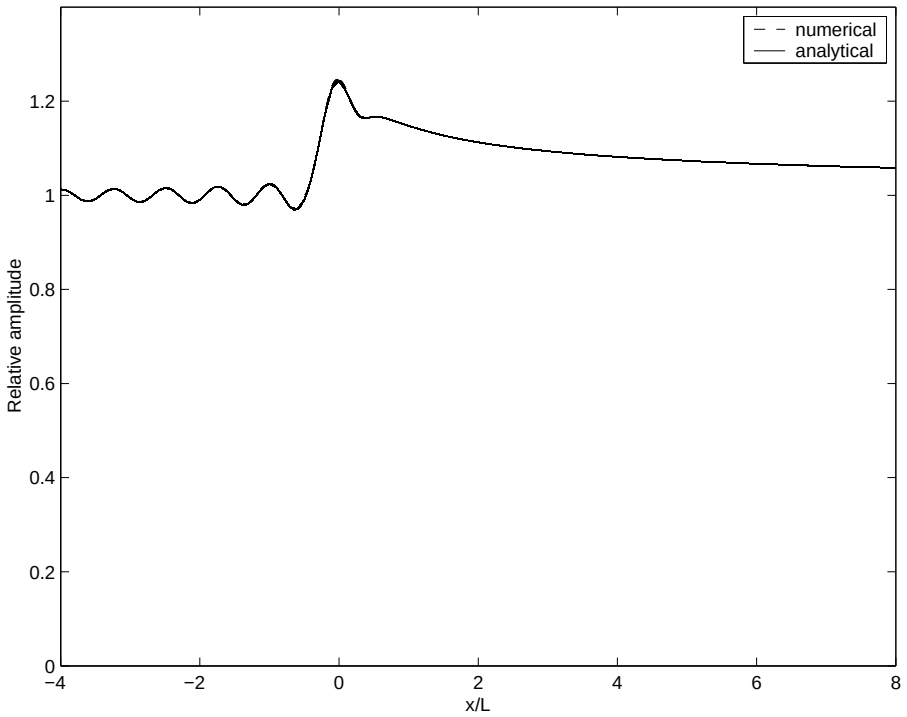

Figure 3.11: Comparison of relative wave amplitudes along the x-axis between the numerical and analytical solutions

It is quite interesting to have observed that for a given hump profile, a smaller h_0 induces a larger relative wave amplitude *behind* the hump, which is expected. But, what is not expected is that it also induces the smallest wave amplitude, in the three cases presented in Fig. 3.13 *in front of* the hump. This is because the incident waves can "feel" the hump more when the h_0 is small and thus the reaction to the disturbance (the hump in this case) behind the hump is larger in comparison with the other two cases. In the mean time, the reaction to the disturbance in front of the hump has little to do with the hump itself. Thus, a smaller h_0 corresponds to a greater relative wave amplitude behind the hump, or from the viewpoint of energy conservation, we can say that, the bigger the hump size, the more energy

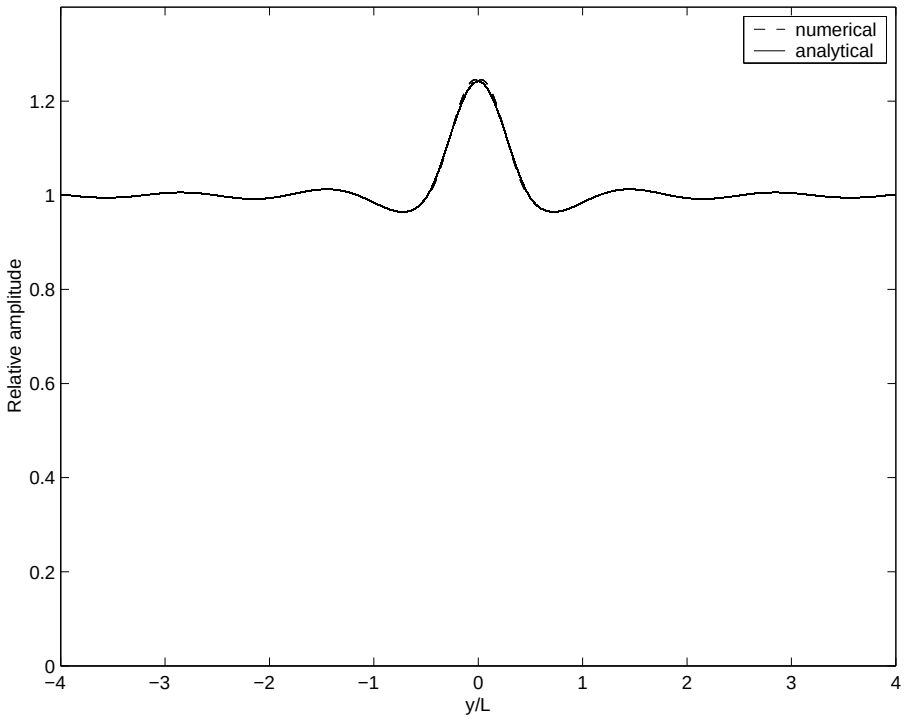

Figure 3.12: Comparison of relative wave amplitudes along the y-axis between the numerical and analytical solutions

from waves can be captured.

In Fig. 3.15 and Fig. 3.16, we have also plotted the relative wave amplitudes along the x- and y-axis, respectively, for different hump radii, b/L = 0.25, 0.5, 0.75, and 1.0 with a fixed h_0 = 3.2 m and h_1 = 4.8 m. As the radius of the hump increases, the relative wave amplitude behind the hump also increases. For instance, in the both cross-sections where we have output the relative wave amplitude, the maximum value of relative wave amplitude is about 1.1 with b/L = 0.25. Then when we have increased the radius to 0.5, the increment of the maximum value of relative wave amplitude is about 11.8%. When we further increase the radius to b/L = 0.75 and 1.0, respectively, we can obviously observe that two peaks of the relative wave

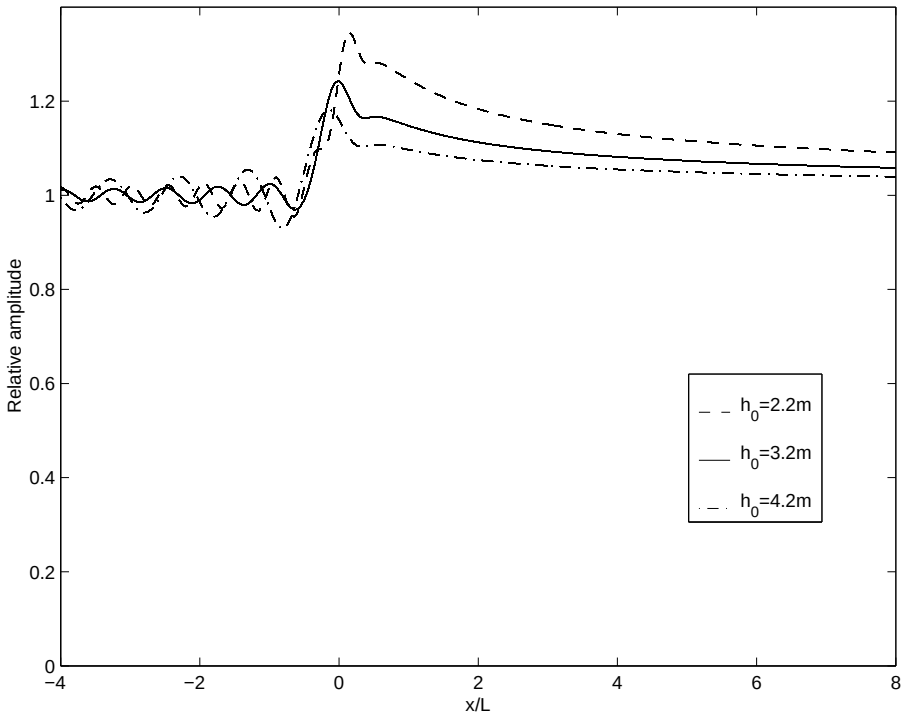

Figure 3.13: Comparison of relative wave amplitudes along the x-axis with different h_0 values

amplitude form behind the hump in the longitudinal direction as shown in Fig. 3.15, whereas such two-peak structure in the relative wave amplitude cannot be prominently observed for smaller hump radius.

A similar two-peak relative wave amplitude structure can be seen in Fig. 3.16 when $b/L = 1.0$. In fact, it is quite interesting to have observed that when the hump radius is gradually increased from $b/L = 0.25$, the maximum relative wave amplitude continuously increases too. However, this monotonic increase terminates when the hump radius is further increased beyond $b/L = 0.75$. When $b/L = 1.0$, a double-peak relative wave amplitude structure is formed. A physical explanation for this phenomenon is that when the hump radius is increased, the total amount of disturbance is increased too

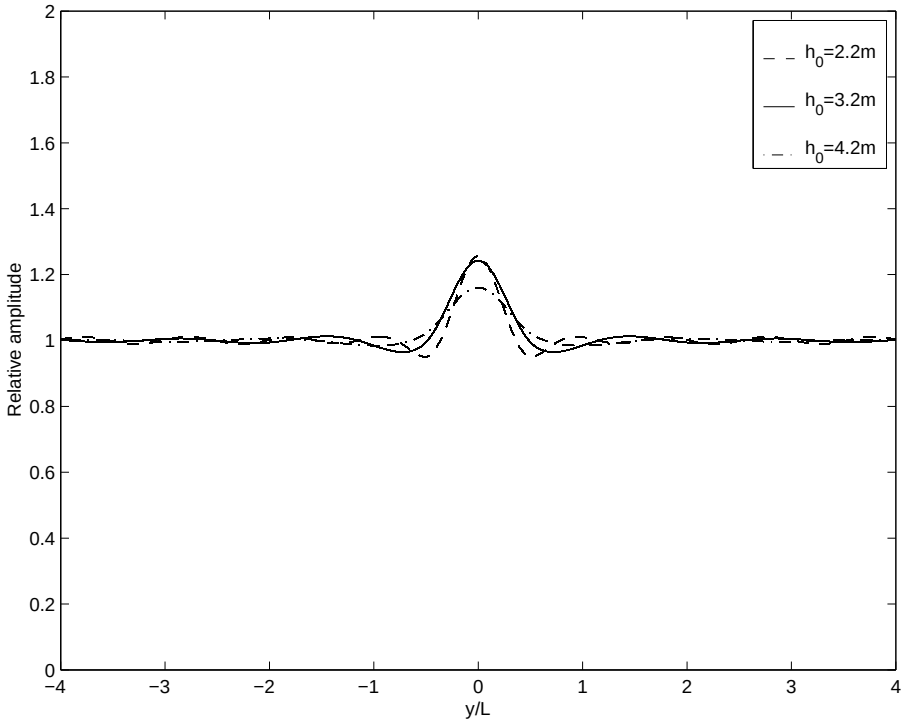

Figure 3.14: Comparison of relative wave amplitudes along the y-axis with different h_0 values

to produce a larger relative wave amplitude in the hump region. But, then such an increase in relative wave amplitude becomes unsustainable when the hump radius is further increased beyond a point where the gravitational force can no longer sustain such increase in wave amplitude; in other words, the gravity would eventually prevents any further increase of the relative wave amplitude. Therefore, as a result of the balance of the gravitational force and the free-surface reaction to the disturbance, one single peak breaks down to a double-peak structure in relative wave amplitude as shown in Fig. 3.16.

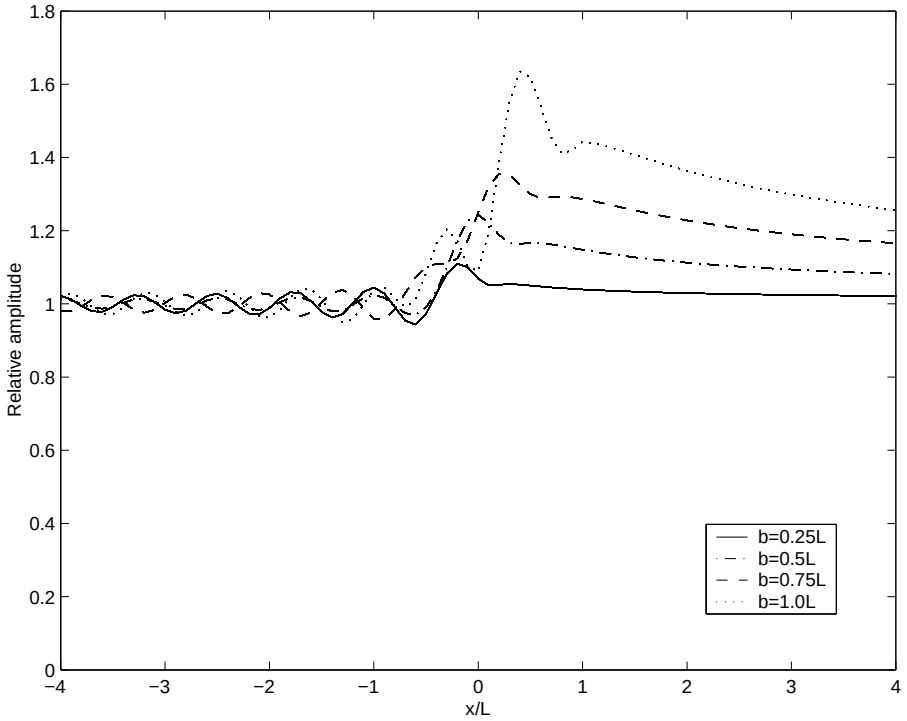

Figure 3.15: Comparison of relative wave amplitudes along the x-axis with different hump radius

3.4 Conclusions

We have constructed an analytic solution for the shallow water wave equation for long waves propagating over a circular hump located on the floor of an ocean with otherwise constant depth. This analytic solution was derived based on the analytic solution for the long waves propagating over a circular pit obtained by Suh. *et. al.* [32]. We make a comparison for both solutions, and found that along the $x-$axis, waves are amplified in front of the hump, whereas there is a relative calm region behind a pit. Along the $y-$axis, the relative wave amplitudes in these two distinct cases are out of phase.

To make a physically meaningful comparison between the cases of pit and hump, we designed a new set of parameters so that all the physical conditions

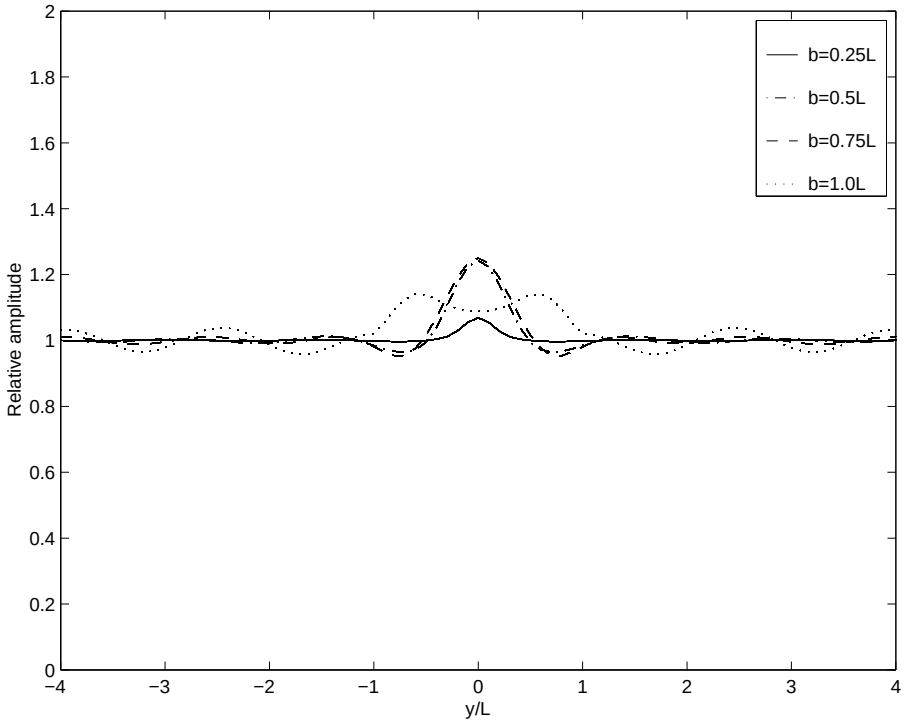

Figure 3.16: Comparison of relative wave amplitudes along the y-axis with different hump radius

such as the incident wavelength, the water depth at the infinity are the same, except a pit is replaced by a hump. Then, we found that the relative wave amplitudes are reversed by 180^o along the lateral line passing through the origin. In the longitudinal direction, the drop of the relative wave amplitude in the pit region is smaller than the rise of the relative wave amplitude right in front of the hump, in contrast with a huge drop of relative wave amplitude for the case Suh. *et. al.* [32] studied with the depth of the pit being of the same order as the water depth at infinity.

We have also verified our new analytical solutions by constructing a numerical solution for the purpose of validation. The two solutions were almost identical and hardly distinguishable.

Finally, we have examined and discussed the effects of the hump dimension when radius and minimum water depth are varied. While an increase of the hump height definitely induces a stronger response of the system with larger wave amplitude behind the hump, an increase in the radius of a hump also leads to an increase of the wave amplitude behind the hump as well. However, if the radius becomes too big while the height of the hump is held constant, eventually a double-peak relative amplitude will form behind the hump.

Chapter 4

Refraction of interfacial waves by a circular hump

4.1 Overview

Internal waves have been of great interest among the researchers since Ekman's theoretical explanation of "dead water" experience by slowly-moving vessels [36]. Internal waves just like surface waves that breaking on the beaches because they often have surface manifestation. Changes in the density of the water, temperature, topography, moving ship through highly stratified water, winds, air-pressure fluctuations, and surface swell are capable of creating internal waves in the ocean [37]. The study of internal waves has become significant because they carry a lot of energy, which may destroy structures, such as deep-sea drilling rigs, drillers, and vertical pipes when traveling in the interior of the ocean body [38].

In the ocean, there exists a thin layer of water, separating the warmer surface zone from the colder deep zone. This thin layer is called thermocline, across which the density as a function of the water temperature also

jumps significantly [37]. Hence, the two-layer ocean models with a sharp density interface separating fluids with two constant densities are very popular in modeling the dynamics of internal wave propagations in an ocean. The propagation of waves on the interface of two different fluid layers was first investigated by Stokes [39] and a description of internal waves in the form of linear motion can also be found in [33]. Since then, many authors have studied internal wave problems in which the upper fluid is either with the presence of a free surface or bounded by a rigid lid. Replacing the free surface with a rigid-lid approximation is reasonable in many cases, especially at the regional ocean scale, because "internal-wave mode" only induces small deformation on the free surface and thus a rigid-lid approximation would exclude the fast mode associated with barotropic free surface waves and greatly simplify the theoretical analysis without loss of a great deal of accuracy. Much work also has been done on internal solitary waves in two-layer fluids, pioneered by authors such as Keulegan [40], Long [41], and Benjamin [42].

The study of internal waves has become important because they are associated with the energy transfer mechanism across continental shelf edges. In addition, they cause strong localized departures from the surrounding ocean conditions, resulting in increased shear stresses on underwater structures and large variations in acoustic transmission properties of the ocean [43]. Therefore, the internal waves cause problems in many areas such as offshore oil recovery, acoustic propagation in the ocean, and deep water outfall. For example, in offshore recovery, the greater part of new offshore oil and gas fields are in deep waters, which are only economically viable due to the development of new recovery technologies that involve cable and wire moorings or long fragile structures such as riser pipes and drill columns. The energy contained in solitary internal waves can result in strong localized currents

which generate high level of shear stress on these structures, causing significant level of damage and representing a potential safety hazard to operations personnel [44].

The mild-slope equation which was firstly derived by Berkhoff [9] is a powerful tool to study the phenomenon of combined refraction-diffraction of ocean waves over a mild topography. The mild-slope equation has also been studied by many researchers since it was introduced, mainly due to its advantage in dimensionality reduction, i.e., by reducing a three-dimensional problem to a two-dimensional problem with the calculated velocity as an average velocity across the water column. For example, Jonsson *et al.* [10] solved the mild-slope equation numerically for the diffraction and refraction around the island and later on, Smith and Sprinks [1], gave a formal derivation of the equation.

Due to some seemingly tight restrictions on the bottom topography for the validity of the mild-slope equation, many researchers have tried to improve the versatility of this equation in terms of including some higher-order terms of the bottom slope. For instance, Massel's [2], used the Galerkin-Eigenfunction Method to derive the extension for mild-slope equation. His resulting equation contains higher-order terms proportional to bottom slope and bottom curvature, as well as the evanescent modes. Then in 1995, Chamberlain and Porter [45] constructed the modified mild-slope equation using the variational principle approach and the resulting equation was shown to be capable of describing scattering properties of singly and doubly periodic ripple beds, in which the Berkhoff's [9] original mild-slope equation fails. Furthermore, in the same year, using the same approach as Chamberlain and Porter [45], Porter and Staziker [46] came out with the extended mild-slope equation which contains the jump conditions to ensure the mass flow continu-

ity at the discontinuous bed slope. By using the original Berkhoff's equation [9] and the modified mild-slope equation derived by Chamberlain and Porter [45], Porter [47] has re-examined these two equations. By identifying the discrepancies between both solutions, he then derived an alternative form for the mild-slope equation, having the simplicity of the standard form [9] and also containing the essential features of the modified mild-slope equation [45] at the same time.

More recently, in 2005, by utilizing the modified mild-slope equation constructed previously by Chamberlain and Porter [45] in 1995, Chamberlain and Porter [48] then derived a mild-slope equation for a two-layer fluid model. Their derivation is based on the variational principle which removes the vertical coordinate, reducing the problem to a pair of coupled partial differential equations for the wave potential of depth-averaged velocity as a function of two horizontal variables. Their resulting equation, which contains the higher-order terms of bottom slope, is capable of accurately calculating wave scattering induced by singly and doubly periodic ripple beds, in which the Berkhoff's mild-slope equation fails. On the other hand, Massel's extended mild-slope equation [2] is based on the Galerkin-Eigenfunction Method, which is a more straightforward method for calculating all terms within the mild-slope approximation. His resulting equation also contains higher-order terms proportional to bottom slope and bottom curvature, in addition to retaining the evanescent modes. Therefore, this equation is capable of dealing with wave scattering over a relatively steep bed and yielding a smooth transition range of wave amplitude through the caustic line. Moreover, Massel's extended mild-slope equation can also be used to determine the waves propagating over a patch of sinusoidal ripples as well. Hence, Massel's approach appears to have led to a more versatile modified mild-slope equation; it is certainly

worthwhile to deduce an extended mild-slope equation for a two-layer fluid model based on Massel's approach, which is part of the objectives of this chapter.

In this chapter, a two-layer mild-slope wave equation is constructed for two-layer fluid model with the rigid-lid assumption being made at the free surface. In Section 4.2, the basic mild-slope equation is derived for the interfacial waves using the same approach used by Smith and Sprinks [1]. By utilizing this equation, we then constructed an analytic solution for long waves propagating over a circular hump located at the bottom of a two-layer ocean. Then, in Section 3, an example is given to compare our new analytic solution in a special case of the two-layer fluid model, i.e $\rho_1 = 0$ with the solution in a single-layer fluid model. As a part of the verification process, we also compared our analytic solution with a numerical solution. Using the new solution, we then discussed the effects of the hump dimensions on the wave refraction. Following Massel's [2] approach, we derived the extended version of mild slope equation, in Section 4.4, with the second-order terms of bottom topography being included. Results obtained from the newly-derived extended mild-slope equation were then compared with those obtained from the conventional one. Finally, the main findings in this chapter are briefly summarized in Section 4.5.

4.2 Analytic Solution

This section presents the derivation of mild-slope equation in two-layer fluid model. Then, we use the results to study long waves propagating in two-layer fluid over a circular hump.

4.2.1 *The Mild-slope equation for the propagation of interfacial waves in a two-layer fluid model*

Consider the stratified, two-layer bounded system depicted in Fig. 4.1, under a Cartesian Coordinate system in which x and y denote a pair of orthogonal horizontal coordinates and z denotes the vertical coordinate measured positively upwards from the interface. By assuming that the two fluids are immiscible, the flow within each layer is irrotational, the interfacial waves are of small amplitude[1] relative to their wavelength and the upper surfaces is bounded by a rigid wall, the velocity potential $\Phi(x, y, z, t)$ can be written as

$$\Phi(x, y, z, t) = \phi(x, y, z)e^{-i\sigma t} \tag{4.1}$$

where $i = \sqrt{-1}$, and σ is a angular velocity of the incident plane waves.

Upon assuming that each layer is irrotational, we can define independent

[1]Internal waves are usually associated with large amplitude and thus linear theory is not adequate to model internal waves. However, linear approximation is usually the first step in any modeling and thus we have made such an assumption, with an intention that our solution can be used at least as the first-order approximation when a second-order or even higher-order theory is developed in the future.

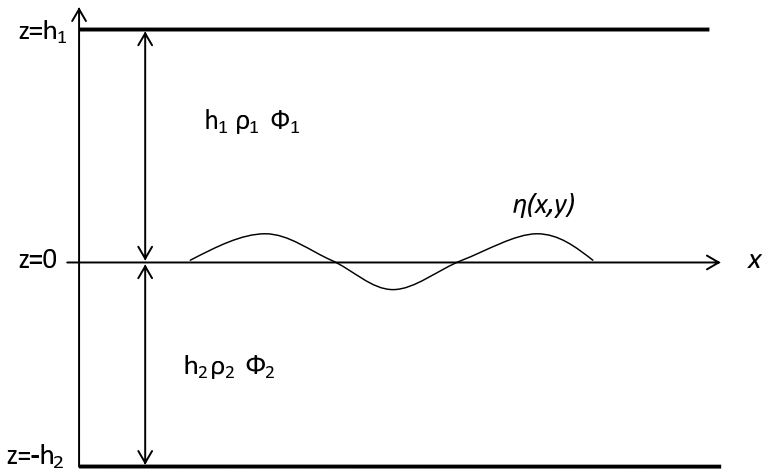

Figure 4.1: A definition sketch for bounded interfacial waves

velocity potentials in each layer; thus, our governing equations are

$$\frac{\partial^2\phi_1}{\partial z^2} + \nabla^2\phi_1 = 0, \qquad 0 \le z \le h_1 \tag{4.2}$$

$$\frac{\partial\phi_1}{\partial z} = -\nabla h_1 \nabla\phi_1, \qquad z = h_1 \tag{4.3}$$

$$\frac{\partial\phi_1}{\partial z} = \frac{\partial\phi_2}{\partial z}, \qquad z = 0 \tag{4.4}$$

$$\rho_1(\frac{\partial\phi_1}{\partial z} - \frac{\sigma^2}{g}\phi_1) = \rho_2(\frac{\partial\phi_2}{\partial z} - \frac{\sigma^2}{g}\phi_2), \qquad z = 0 \tag{4.5}$$

$$\frac{\partial\phi_2}{\partial z} = -\nabla h_2 \nabla\phi_2, \qquad z = -h_2 \tag{4.6}$$

$$\frac{\partial^2\phi_2}{\partial z^2} + \nabla^2\phi_2 = 0, \qquad -h_2 \le z \le 0 \tag{4.7}$$

where g is the gravitational acceleration, and the densities and the waves heights of the upper and lower fluid layer are denoted by ρ_1, h_1, and ρ_2, h_2 respectively, with $\rho_1 < \rho_2$.

By assuming that the variation of water depth is moderate, the velocity potential can be written as

$$\phi_1 = i\frac{\sigma}{k}\eta f_1 \tag{4.8}$$

$$\phi_2 = -i\frac{\sigma}{k}\eta f_2 \tag{4.9}$$

with k as a wave number and

$$f_1 = \frac{\cosh k(z-h_1)}{\sinh kh_1} \tag{4.10}$$

$$f_2 = \frac{\cosh k(z+h_2)}{\sinh kh_2} \tag{4.11}$$

$$\sigma^2 = \frac{gk(\rho_2-\rho_1)}{\rho_1\coth(kh_1)+\rho_2\coth(kh_2)} \tag{4.12}$$

with f_1 and f_2 satisfying

$$\frac{\partial^2 f_1}{\partial z^2} - k^2 f_1 = 0, \qquad 0 \le z \le h_1 \tag{4.13}$$

$$\frac{\partial f_1}{\partial z} = 0, \qquad z = h_1 \tag{4.14}$$

$$\frac{\partial f_1}{\partial z} = \frac{\partial f_2}{\partial z} = \frac{\sigma^2}{g}\frac{(f_2\rho_2 + f_1\rho_1)}{\rho_2-\rho_1}, \qquad z = 0 \tag{4.15}$$

$$\frac{\partial f_2}{\partial z} = 0, \qquad z = -h_2 \tag{4.16}$$

$$\frac{\partial^2 f_2}{\partial z^2} - k^2 f_2 = 0, \qquad -h_2 \le z \le 0 \tag{4.17}$$

One should note that the dispersion relation, Eq.(4.12), has only one positive solution for the wave number k. This is a natural consequence of the rigid-lid assumption, which has removed the "free-surface-wave mode". In other words, the wave number k obtained from Eq.(4.12) already represents the slow "internal-wave mode", which dominates ocean circulation.

Employing the Green's Identity

$$\int_0^{h_1}[f_1(\frac{\partial^2\phi_1}{\partial z^2}-k^2\phi_1)-\phi_1(\frac{\partial^2 f_1}{\partial z^2}-k^2 f_1)]dz$$
$$+\int_{-h_2}^{0}[f_2(\frac{\partial^2\phi_2}{\partial z^2}-k^2\phi_2)-\phi_2(\frac{\partial^2 f_2}{\partial z^2}-k^2 f_2)]dz$$
$$=[f_1\frac{\partial\phi_1}{\partial z}-\phi_1\frac{\partial f_1}{\partial z}]+[f_2\frac{\partial\phi_2}{\partial z}-\phi_2\frac{\partial f_2}{\partial z}] \tag{4.18}$$

we have

$$\int_0^{h_1}[f_1(\nabla^2\phi_1-k^2\phi_1)]dz+\int_{-h_2}^{0}[f_2(\nabla^2\phi_2-k^2\phi_2)]dz=$$
$$-[f_1\nabla h\cdot\nabla\phi_1]_{h_1}+[f_1\nabla h\cdot\nabla\phi_1]_{-h_2}-[\frac{\sigma^2}{g}(f_1\phi_2-f_2\phi_1)]_0 \tag{4.19}$$

By calculating $\nabla\phi_1, \nabla^2\phi_1, \nabla\phi_2$ and $\nabla^2\phi_2$ from Eqs. (4.8) and (4.9) and inserting them into Eq. (4.19), we have

$$\int_0^{h_1}[f_1^2\nabla^2\eta+2f_1\frac{\partial f_1}{\partial h_1}\nabla\eta\cdot\nabla h_1+\eta f_1\frac{\partial^2 f_1}{\partial h_1^2}(\nabla h_1)^2+\eta f\frac{\partial f_1}{\partial h_1}\nabla^2 h_1-k^2\eta f_1^2]$$
$$-\int_{h_2}^{0}[f_2^2\nabla^2\eta+2f_2\frac{\partial f_2}{\partial h_2}\nabla\eta\cdot\nabla h_2+\eta f_2\frac{\partial^2 f_2}{\partial h_2^2}(\nabla h_2)^2+\eta f\frac{\partial f_2}{\partial h_2}\nabla^2 h_1-k^2\eta f_2^2]$$
$$=-\nabla h_1\nabla\eta f_1^2|_{h_1}-\eta f_1\frac{\partial f_1}{\partial h_1}(\nabla h_1)^2|_{h_1}-\nabla h_2\nabla\eta f_2^2|_{-h_2}$$
$$-\eta f_2\frac{\partial f_2}{\partial h_2}(\nabla h_2)^2|_{-h_2} \tag{4.20}$$

From the Leibniz rule and using the assumption that the variation of water depth is moderate, we can ignore all the terms of order $(\nabla h_1)^2$, $(\nabla h_2)^2$, $\nabla^2 h_1$ and $\nabla^2 h_2$ and rewrite Eq. (4.20) as

$$\nabla\cdot(\int_0^{h_1}f_1^2dz-\int_{h_2}^{0}f_2^2dz)\nabla\eta+k^2(\int_0^{h_1}f_1^2dz-\int_{h_2}^{0}f_2^2dz)\eta=0 \tag{4.21}$$

which leads to

$$\nabla \cdot (CC_g \nabla \eta) + k^2 CC_g \eta = 0 \tag{4.22}$$

with

$$C = \sqrt{\frac{g}{k} \frac{(\rho_2 - \rho_1)}{\rho_1 \coth kh_1 + \rho_2 \coth kh_2}} \tag{4.23}$$

$$C_g = \frac{C}{2}\{1 + \frac{\sigma^2}{g(\rho_2 - \rho_1)}(\frac{\rho_1 h_1}{sinh^2 kh_1} + \frac{\rho_2 h_2}{sinh^2 kh_2})\} \tag{4.24}$$

being the phase velocity and the group velocity for two-layer mild-slope equation, respectively.

Eq. (4.22) is the mild-slope equation for our two-layer fluid model with the rigid-lid assumption being used as an approximation for the free surface. In the ocean, internal gravity waves generally have quite small amplitudes at the free surface [27]. Therefore, replacing the free surface with a rigid upper boundary is reasonable to simplify the theoretical analysis without great loss of accuracy [49].

Eq. (4.22) has the same form as the single-layer mild-slope equation derived by Smith and Sprinks [1], except with different group velocity, C_g and phase velocity, C. Because of the restoring force excited by the internal deformation of the water layers of equal density is much smaller than that in the case of surface waves, internal waves generally have smaller period and length, slower speed than surface waves. If we let $\rho_1 = 0$, then we see that the phase velocity, C, and the group velocity C_g for the two-layer waves reduces to C and C_g for the single-layer mild-slope equation. As a result, Eq. (4.22) also reduces to the single-layer mild-slope equation. Thus, the single-layer mild-slope equation is a special case for two-layer mild-slope equation, as we have expected.

4.2.2 *Long waves propagating over a circular hump*

Now, consider a train of plane long waves which propagates in two-layer fluids with constant water depth h_{10} and h_{20} and is refracted by an axi-symmetric hump-shaped shoal located on the ocean floor.

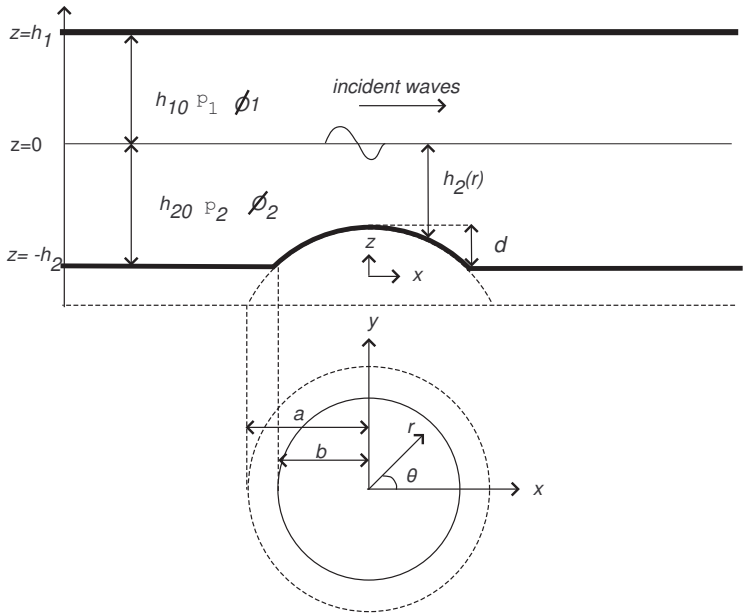

Figure 4.2: A definition sketch of a hump located on the floor in two-layer fluid systems

The cross-section of the hump is of the shape of a parabola and the surface of the hump is formed through revolving the parabola around the vertical axis of revolution, which is marked with the z coordinate of a Cartesian coordinate system chosen with its origin located at the center of the hump as demonstrated in Fig. 4.2. The parabolic hump surface intersects with the ocean floor at $z = -h_2$, resulting in a circle with its radius denoted as b, and the height of the hump is controlled by a parameter d as shown in Fig. 4.2. In the corresponding cylindrical coordinate system with r being the radial

distance from the origin and θ being the angle measured counterclockwise from the positive $x-$axis, the water depth for the lower layer is prescribed by a parabolic function

$$h_2 = \begin{cases} (h_{20} - d)(1 + \frac{r^2}{a^2}), & r < b \\ (h_{20} - d)(1 + \frac{b^2}{a^2}), & r \geq b \end{cases} \tag{4.25}$$

In Eq. (4.25), a is determined by $a = b\sqrt{\frac{(h_{20}-d)}{d}}$, for a given set of d and h_{20} and $a > b$. Therefore, geometrically, a is the radius of the cross-sectional circle of the paraboloid intersecting with a horizontal plane located below the seabed. While d is used to control the height of the hump, either b or a is used to control the horizontal dimension of the hump.

When the wavelength is much longer than the wave height, Eq. (4.22) can be reduced to a long (shallow water) wave equation which takes the form

$$\nabla \cdot (\frac{(\rho_2 - \rho_1)h_1 h_2}{\rho_1 h_2 + \rho_2 h_1} \nabla \eta) + \frac{\sigma^2}{g}\eta = 0 \tag{4.26}$$

under the assumptions $C \cong C_g \cong \sqrt{\frac{g(\rho_2-\rho_1)h_1h_2}{\rho_1 h_2+\rho_2 h_1}}$ and $\sigma^2 \cong \frac{gk^2(\rho_2-\rho_1)h_1h_2}{\rho_1 h_2+\rho_2 h_1}$, where g is the gravitational acceleration, h_1 and h_2 are the local water depth for the upper and lower layer respectively, σ is the angular velocity of the incident plane waves and k is the wave number. We shall now present an exact solution as Zhu and Harun [11] did for the refraction of progressive waves on the free surface of a single layer of fluid over an axi-symmetric hump-shaped shoal located on the ocean floor. The Frobenius series expansion approach we use here has also been used by Zhang and Zhu [25], and Suh *et. al.* [32].

It is convenient to adopt a cylindrical coordinate system (r, θ, z) with $x = r\cos(\theta)$ and $y = r\sin(\theta)$, because the bottom topography of this problem is axi-symmetric with respect to the $z-$axis. In this case, h_2 is a function of r only and a solution to Eq. (4.26) can be constructed via the separation of

variables as

$$\eta = \sum_{n=0}^{\infty} R_n(r)\cos(n\theta) \tag{4.27}$$

with $R_n(r)$ satisfying

$$\begin{aligned}(a^2+r^2)(\rho_1 h_2+\rho_2 h_1)r^2\frac{\mathrm{d}^2R_n}{\mathrm{d}r^2}+((a^2+r^2)(\rho_1 h_2+\rho_2 h_1)+2\rho_2 h_1 r^2)r\frac{\mathrm{d}R_n}{\mathrm{d}r}\\ +(\frac{(\rho_1 h_2+\rho_2 h_1)^2}{(\rho_2-\rho_1)h_1}v^2r^2-n^2(a^2+r^2)(\rho_1 h_2+\rho_2 h_1))R_n=0\end{aligned} \tag{4.28}$$

where v is defined as

$$v = \frac{\sigma a}{\sqrt{g(h_{21}-d)}} \tag{4.29}$$

The general solution of Eq. (4.28) can be obtained in terms of the Frobenius series [35]:

$$R_n(r) = \sum_{m=0}^{\infty} \alpha_{m,n} r^{m+c} \tag{4.30}$$

with $\alpha_{0,n}$ being unity and c being a constant to be determined by the indicial equation. As shown in [35], it should be emphasized here that convergence of the series solution is guaranteed at $r < a$. Therefore, the solution always converges in the hump region with $r < b$. Solving Eq. (4.28) using the method of Frobenius, we obtain the indicial equation, $c^2 - n^2 = 0$, which yields two roots:

$$c = \pm n \tag{4.31}$$

These two distinct roots of the indicial equation lead to two sets of linearly independent solutions:

$$R_{n,1} = \sum_{m=0}^{\infty} \alpha_{m,n} r^{m+n} \tag{4.32}$$

$$R_{n,2} = R_{n,1} \ln r + \beta_{m,n} r^{m-n} \tag{4.33}$$

Since $R_{n,2}$ becomes singular at $r = 0$, it has to be discarded, with the imposition of the condition that water surface elevation must be finite at the origin.

Now, substituting Eq. (4.30) with $c = n$ into Eq. (4.28) and collecting the terms of the same order of r, we obtain

$$\alpha_{1,n} = \alpha_{3,n} = \alpha_{5,n} = 0 \tag{4.34}$$

$$\begin{aligned} \alpha_{2,n} &= -\frac{\alpha_{0,n}}{a^4(\rho_1(h_{21}-d)+\rho_2 h_1)((n+1)(n+2)+n+2-n^2)} \\ &\quad (2a^2\rho_1(h_{21}-d)(n(n-1)+n-n^2)+ \\ &\quad \rho_2 h_1 a^2(n(n-1)+3n-n^2+\gamma_1+\gamma_2+\gamma_3)) \end{aligned} \tag{4.35}$$

$$\begin{aligned} \alpha_{4,n} &= -\frac{1}{a^4(\rho_1(h_{20}-d)+\rho_2 h_1)((n+4)(n+3)+n+4-n^2)} \\ &\quad [(\rho_1(h_{21}-d)(n(n-1)+n-n^2+\gamma_4+\gamma_5))\alpha_{0,n} \\ &\quad +(2a^2\rho_1(h_{21}-d)(n(n-1)(n+2)+n+2-n^2))\alpha_{2,n} \\ &\quad +(\rho_2 h_1 a^2((n+1)(n+2)+3(n+2)-n^2) \\ &\quad +\gamma_1+\gamma_2+\gamma_3)\alpha_{2,n}] \end{aligned} \tag{4.36}$$

$$\alpha_{m+6,n} = -\frac{\gamma_6\alpha_{m,n}+\gamma_7\alpha_{m+2,n}+\gamma_8\alpha_{m+4,n}}{\gamma_9}, \qquad \text{with } m = 0, 1, 2, ... \tag{4.37}$$

and

$$\gamma_1 = \frac{\mu^2((\rho_1)^2(h_{21}-d)a^4}{h_1(\rho_2-\rho_1)} \tag{4.38}$$

$$\gamma_2 = \frac{2a^4\mu^2\rho_1\rho_2}{\rho_2-\rho_1} \tag{4.39}$$

$$\gamma_3 = \frac{\mu^2(\rho_2)^2h_1a^4}{(h_{21}-d)(\rho_2-\rho_1)} \tag{4.40}$$

$$\gamma_4 = \frac{2\gamma_1}{a^2} \tag{4.41}$$

$$\gamma_5 = \frac{2\gamma_2}{a^2} \tag{4.42}$$

$$\gamma_6 = \frac{\gamma_1}{a^4} \tag{4.43}$$

$$\begin{aligned}\gamma_7 = {} & \rho_1(h_{21}-d)((m+n+2)(m+n+1)+m+n+2-n^2 \\ & +\gamma_4+\gamma_5)\end{aligned} \tag{4.44}$$

$$\begin{aligned}\gamma_8 = {} & 2a^2\rho_1(h_{20}-d)((m+n+4)(m+n+3)+m+n+4-n^2)+ \\ & a^2\rho_2h_1((m+n+4)(m+n+3)+3(m+n+4)-n^2)+ \\ & \gamma_1+\gamma_2+\gamma_3\end{aligned} \tag{4.45}$$

$$\begin{aligned}\gamma_9 = {} & a^4(\rho_1(h_{21}-d)+\rho_2h_1)((m+n+6)(m+n+5) \\ & +m+n+6-n^2)\end{aligned} \tag{4.46}$$

where m denotes the number of recurrence solutions for Frobenius series solution that we have to find until our solution is converged to a desire point,

while n corresponds to the wave propagation modes.

For the general solution in the finite region with variable depth $r < b$, the water surface elevation can be written as:

$$\eta_2 = \sum_{n=0}^{\infty} B_n R_n \cos n\theta \tag{4.47}$$

where B_n is a set of complex constants to be determined by matching the solution in this region with that in the region of constant water depth. The undisturbed long-crested incident waves propagate in the positive x-direction and its surface elevation is given by [4]:

$$\eta_0 = a_i e^{ikx} = a_i \sum_{n=0}^{\infty} i^n \varepsilon_n J_n(kr) \cos n\theta \tag{4.48}$$

where a_i is the incident wave amplitude and $i = \sqrt{-1}$, J_n is the Bessel function of the first kind of order n, and ε_n is the Jacobi symbol defined by

$$\varepsilon_n = \begin{cases} 1, & n = 0 \\ 2, & n \geq 1 \end{cases} \tag{4.49}$$

In the constant depth region ($r \geq b$), the solution is well known as given in [3],

$$\eta_1 = \eta_0 + \sum_{n=0}^{\infty} D_n H_n^{(1)}(kr) \cos n\theta \tag{4.50}$$

where D_n is some unknown coefficients to be determined later, and $H_n^{(1)}$ is the Hankel function of the first kind of order n.

The solutions in these two sub-regions must be matched on the common boundary $r = b$ to ensure the continuity of wave heights and the hydrodynamic pressure across it [5]. Thus, it requires that

$$\eta_1 = \eta_2 \tag{4.51}$$

$$\frac{\partial \eta_1}{\partial r} = \frac{\partial \eta_2}{\partial r} \tag{4.52}$$

Therefore, from Eqs. (4.47)-(4.52), the coefficients B_n and D_n can be determined as

$$B_n = a_i k i^n \varepsilon_n \frac{J_n(kb)H_n'^{(1)}(kb) - J_n'(kb)H_n^{(1)}(kb)}{kR_n(b)H_n'^{(1)}(kb) - R_n'(b)H_n^{(1)}(kb)} \tag{4.53}$$

$$D_n = a_i i^n \varepsilon_n \frac{kJ_n'(kb)R_n(b) - J_n(kb)R_n'(b)}{H_n^{(1)}(kb)R_n'(b) - kH_n'^{(1)}(kb)R_n(b)} \tag{4.54}$$

in which the primes denote the derivatives with respect to the argument. By substituting these coefficients back into Eqs. (4.47) and (4.50), the water surface elevation for the entire domain can be computed. Some results of specific calculations are presented in the next section.

4.3 Results and Discussions

In this section, we present an example to compare our new analytic solution for a special case of the mild-slope equation in two-layer fluid model i.e. taking $\rho_1/\rho_2 = 0$ with the single-layer mild-slope equation discussed in Zhu and Harun [11]. For $\rho_1/\rho_2 \neq 0$, we have compared our analytical solution with a numerical solution as part of the verification process. Then, we examine the effect of wave refraction when the ratio of the densities, ρ_1/ρ_2 and the ratio of upper and lower water depth, h_{10}/h_{20} are varied. Lastly, using the new solution, we discuss the effect of hump dimensions on the wave refraction process over a hump.

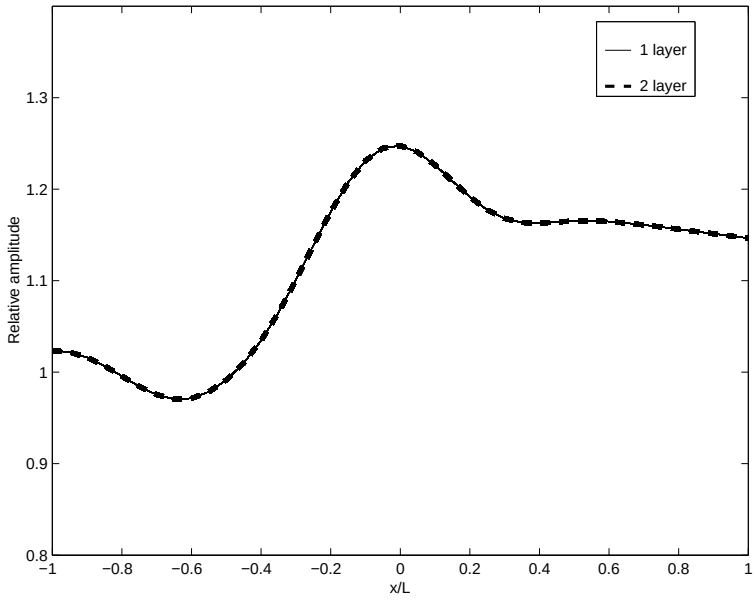

Figure 4.3: Comparison of relative wave amplitudes between single-layer and two-layer fluid models with $\rho_1 = 0$ along x-axis at y=0

4.3.1 *Comparison with the single-layer fluid model*

Since the mild-slope equation for a two-layer fluid model should reduce to that derived from a single-layer model when $\rho_1 = 0$, it would be interesting to compare both models, as part of the verification process.

We set $\rho_1 = 0$, $\rho_2 = 5$, $h_{10} = h_{20} = 4.8$, and take the remaining parameters exactly the same as those used in single-layer fluid model discussed in Zhu and Harun [11], i.e, $b/L = 0.5$, and the wave length, $L = 120.4$. Since, the analytic solution for η involves an infinite series, it must be truncated for the purpose of numerical solution, so we set $N = 70$ and $M = 30$, because the solution had already 100% converged with these values. The Bessel and Hankel functions in the analytical solution were computed using the built-in subroutines in MATLAB.

Fig. 4.3 and Fig. 4.4 show the comparison of the relative wave ampli-

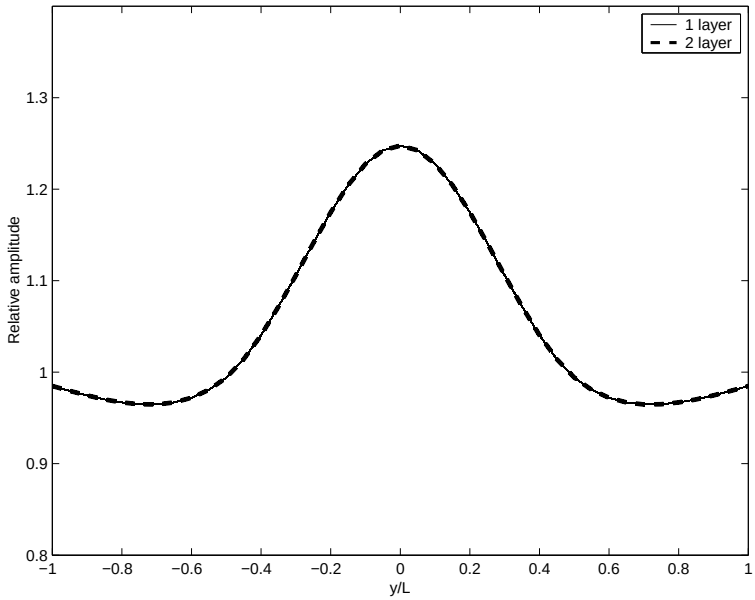

Figure 4.4: Comparison of relative wave amplitudes between single-layer and two-layer fluid models with $\rho_1 = 0$ along y-axis at x=0

tudes along the x- and y-axes respectively for the two- and single-layer fluid models. The results in this comparison are presented in terms of dimensionless coordinates, x/L and y/L, and the centers of the hump is located at the origin. As expected, both solutions are identical and became hardly distinguishable. With the excellent agreement between these solutions, we are confident that the derivation of our new analytical solution is correct.

4.3.2 *Comparison with the numerical solution*

In order to further verify the newly derived mild-slope equation for the case $\rho_1/\rho_2 \neq 0$, the new analytic solution is also compared with a numerical solution.

Eq. (4.28) is only the ordinary differential equation, which can be easily solved numerically using the 2*nd*-order central finite difference scheme, with

two boundary conditions being imposed at the center of the region $r = 0$ and the outer boundary of the region $r = b$. At $r = b$, the boundary condition can be easily obtained by the matching condition in Eqs. (4.51) and (4.52). The boundary condition at $r = 0$, can be determined by

$$\frac{dR_n}{dr} = 0 \tag{4.55}$$

which reflects the fact that the slope of the wave elevation at the origin must be continuous.

Figs. 4.5 and 4.6 show the comparison between the analytic and numerical solutions for the case of $h_{10} = h_{20} = 4.8$, $d = 1.6$, $a/L = \sqrt{0.5}$, $b/L = 0.5$. When the grid spacing was reduced to $\Delta r = 0.025$, the numerical solution and analytic solution became hardly distinguishable. Such an excellent agreement is manifested through Fig. 4.5 and Fig. 4.6. Therefore, this adds additional confidence on the correctness of our derivation.

4.3.3 *Effect of the density ratio*

In this section, we discuss the effect of the wave refraction when the ratio of the densities, ρ_1/ρ_2 is varied, while other parameters are held constant.

To examine this, we set $\rho_1/\rho_2 = 0$, $1/5$, $2/5$, $3/5$, and $4/5$ with the hump radius being fixed at $b/L = 0.5$ and $h_{10} = h_{20} = 4.8$. The comparisons for each value of ρ_1/ρ_2 along the x- and y-axes are shown in Fig. 4.7 and Fig. 4.8, respectively. It can be clearly seen that, an increase in the ratio of the densities, ρ_1/ρ_2 results in the smaller relative wave amplitudes. This phenomenon occurs because there is a smaller density difference between the two layers with the increase of the ratio, resulting in a weaker restoring force for both layers.

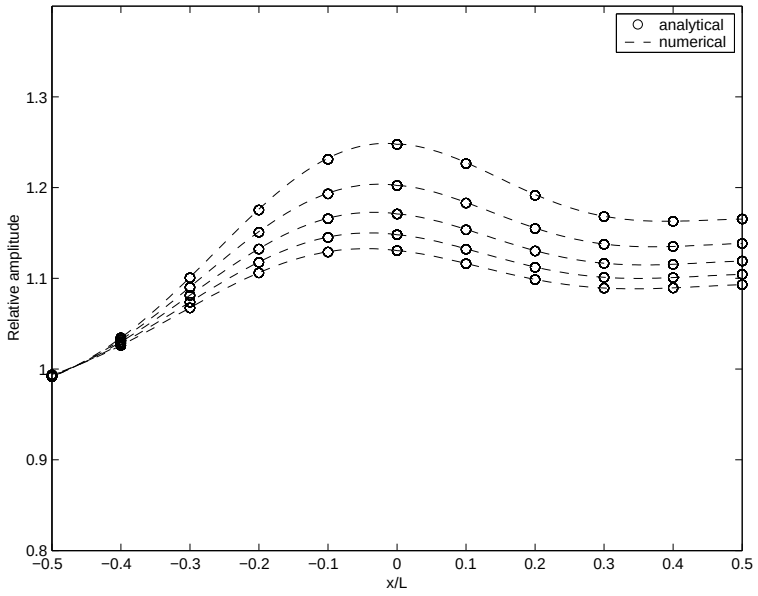

Figure 4.5: Comparison of relative wave amplitudes using numerical and analytical solution when ρ_1/ρ_2 are varied along the x-axis at y=0

4.3.4 *Effect of the Layer Thickness*

Next, we study the effect of the wave refraction when the ratio of the upper and lower water depth, h_{10}/h_{20} is varied, while the total water depth and other parameters remain unchanged.

Fig. 4.9 and Fig. 4.10 are the contour plots of the relative wave amplitudes for waves propagating over a hump with $\rho_1/\rho_2 = 3/5$ and $h_{10}/h_{20} = 1/2$ and $h_{10}/h_{20} = 2.0$, respectively. As can be seen, the wave patterns are quite different for these two cases especially near the hump area. To make a better comparison, we have also plotted out the relative wave amplitude along the x- and y-axis, respectively, in Figs. 4.11 and 4.12.

Figs. 4.11 and 4.12 illustrate the relative wave amplitude for three different values of h_{10}/h_{20}, with $\rho_1/\rho_2 = 3/5$ along the x- and y-axes to examine the effects of the layer thickness to the wave refraction. Here, we set the

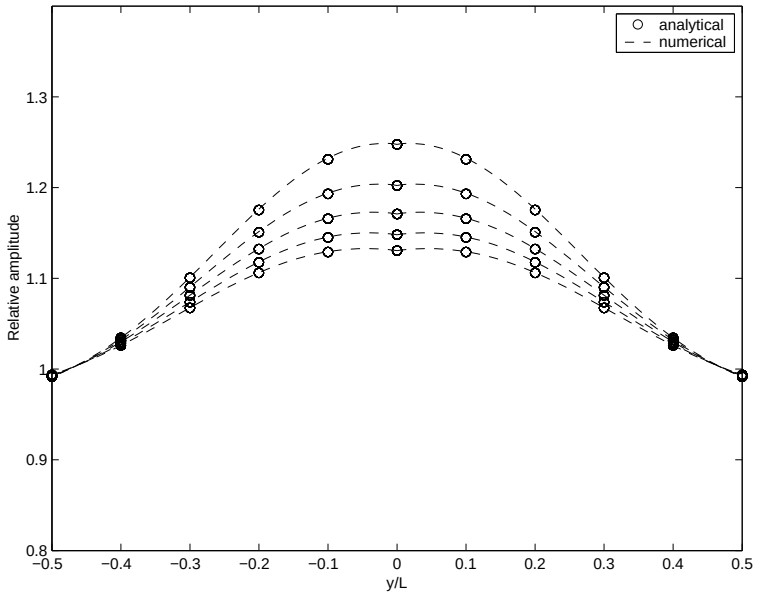

Figure 4.6: Comparison of relative wave amplitudes using numerical and analytical solution when ρ_1/ρ_2 are varied along the y-axis at x=0

others parameters as before and only vary the upper and lower water depth in such a way that the total water depth is kept the same.

As can be clearly seen from both figures, the relative wave amplitude has been amplified more when the upper layer is thicker than the lower layer, i.e $h_{10}/h_{20} = 2.0$. This is because, when the lower layer has less fluid than the upper layer, the incident waves can "feel" the bottom topography more, as the interface is closer to the seabed. Therefore, the interfacial waves can refract more, resulting in a bigger relative wave amplitude. As a contrast, when the lower layer is thicker than upper layer, i.e $h_{10}/h_{20} = 1/2$, there is more fluid in lower layer, and thus the influence of seabed is less, resulting in the smaller relative wave amplitude.

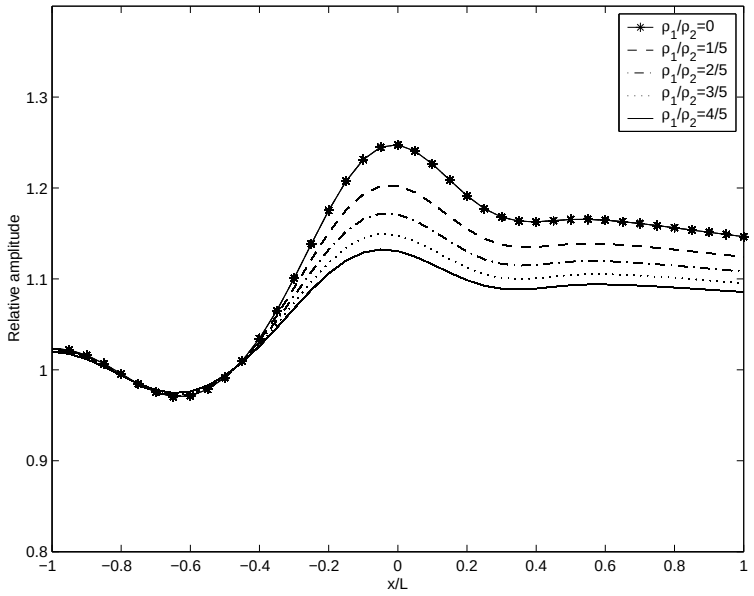

Figure 4.7: Comparison of relative wave amplitudes when ρ_1/ρ_2 are varied along the x-axis at y=0 by using the analytic solution

4.3.5 *Topographic Effects*

After observing the effects of the relative wave amplitude with the various values of ρ_1/ρ_2 and h_{10}/h_{20}, it is interesting to examine the effects of the wave refraction when the dimension of the bottom topography is varied.

In Figs. 4.13, and 4.14 we plot the relative wave amplitudes along the $x-$ and $y-$axes for different hump radii, $b/L = 0.25$, 0.5, 0.75 and 1.0 with a fixed $d = 1.6$ and $h_{20} = 4.8$ with $\rho_1/\rho_2 = 3/5$, respectively.

Along the $x-$axis, the relative wave amplitude increases with the increase of the hump radius. For a small hump radius, the maximum relative wave amplitude occurs in front of the hump (as shown by the dotted line in Fig. 4.13). As the radius of the hump, b/L is increased, the location of the maximum relative wave amplitude moves towards the center of the hump, passes it, and then continues to move into the lee region. This is due to the

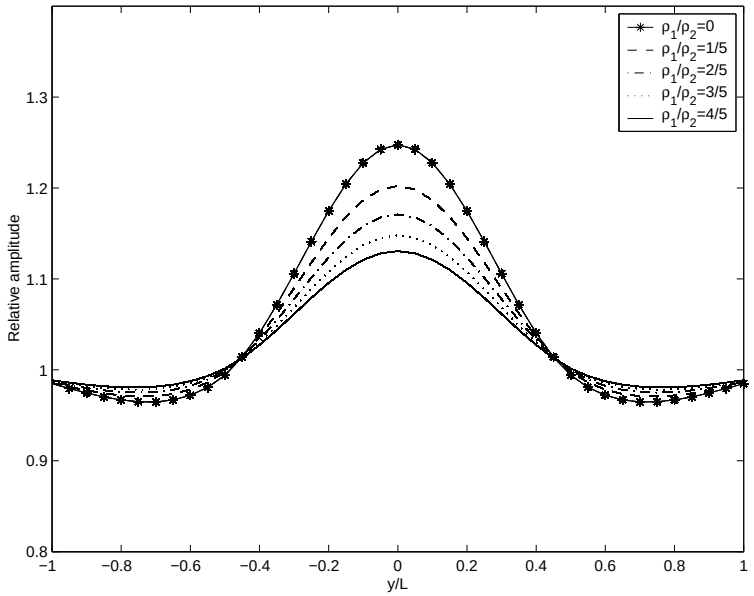

Figure 4.8: Comparison of relative wave amplitudes when ρ_1/ρ_2 are varied along the y-axis at x=0 by using the analytic solution

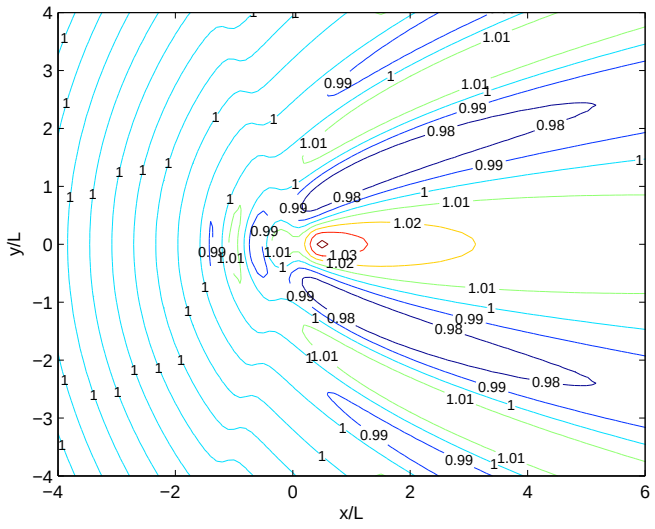

Figure 4.9: Contour plots of relative wave amplitude for waves propagating over a hump with $\rho_1/\rho_2 = 3/5$ and $h_{10}/h_{20} = 1/2$

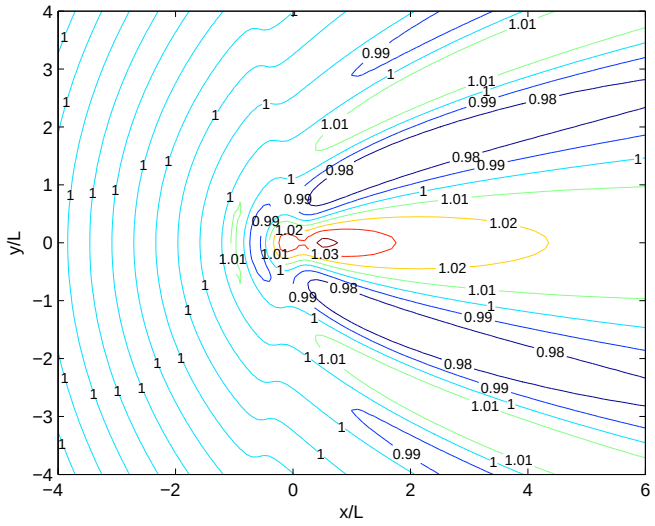

Figure 4.10: Contour plots of relative wave amplitude for waves propagating over a hump with $\rho_1/\rho_2 = 3/5$ and $h_{10}/h_{20} = 2$

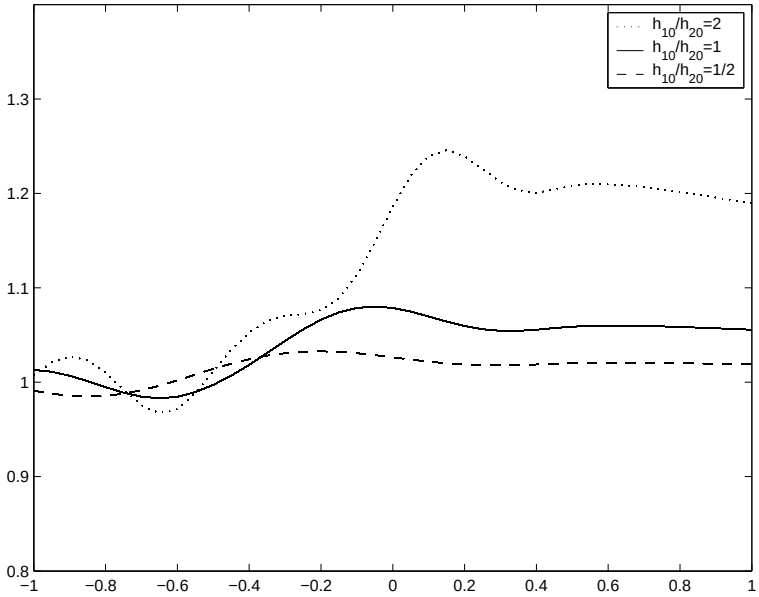

Figure 4.11: Comparison of relative wave amplitudes with $\rho_1/\rho_2 = 3/5$ along x-axis with h_{10}/h_{20} varied

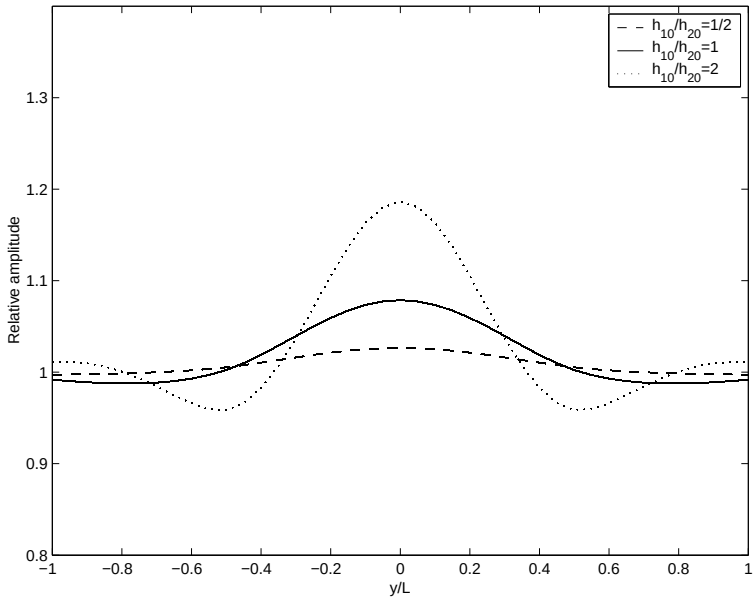

Figure 4.12: Comparison of relative wave amplitudes with $\rho_1/\rho_2 = 3/5$ along y-axis with h_{10}/h_{20} varied

concentration of wave energy in the lee region of an obstacle, as a result of refractive focusing, when the disturbance of the obstacle is sufficiently large. However, along the $y-$axis, as shown in Fig. 4.14, at the origin, the relative wave amplitude for the biggest hump size, $b/L = 1.0$, is lower than those with $b/L = 0.5$ and $b/L = 0.75$, as a result of maximum wave amplitude moves backward.

Next, we discuss the effects of the wave refraction when the height of the hump, d is varied. Fig. 4.15 and Fig. 4.16 show the relative wave amplitude along the $x-$ and y- axes, respectively, for the cases of $d = 0.5$, 1.0, 1.5, and 2.0 with the hump radius being fixed at $b/L = 0.5$, $\rho_1/\rho_2 = 3/5$, and $h_{10} = h_{20} = 4.8$. As can be clearly seen from Fig. 4.15 and Fig. 4.16, as the height of the hump increases, the relative wave amplitude becomes larger as expected.

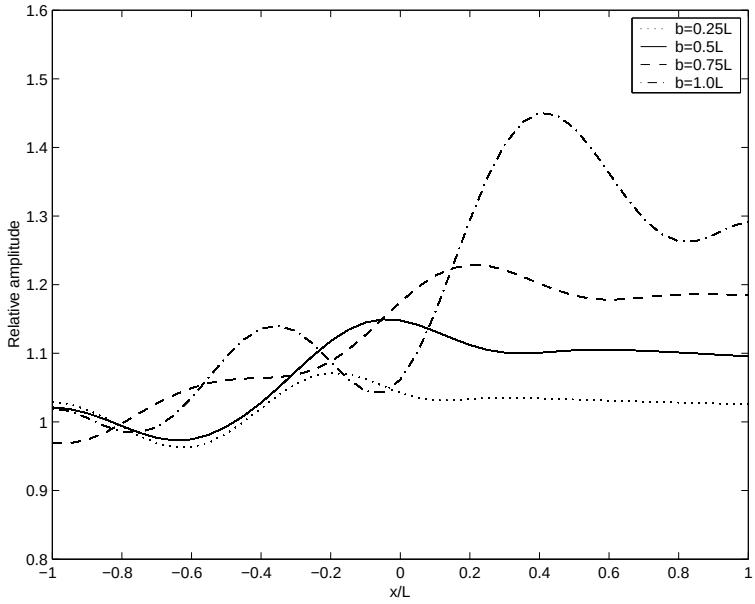

Figure 4.13: Comparison of relative wave amplitudes with $\rho_1/\rho_2 = 3/5$ along the x-axis with b/L varied

For a hump with a smaller hump height, d, the refraction effects are weak, resulting in an almost even distribution of wave heights across the hump. On the other hand, for a higher hump height, d, there is more refractive focusing and thus the reaction to the disturbances behind the hump is larger in comparison with the lower d. For example, along the $x-$axis, as we increase the height of the hump, from 0.5 to 1.0, the maximum value of relative wave amplitude obtained has increased too from 1.04 to 1.09, and if we further increase the hump height to 2.0, the maximum value of relative wave amplitude obtained is about 1.35. The same phenomenon is occurred along the y-axis, as we can see that the increasing of the hump height will increase the relative wave amplitude as well.

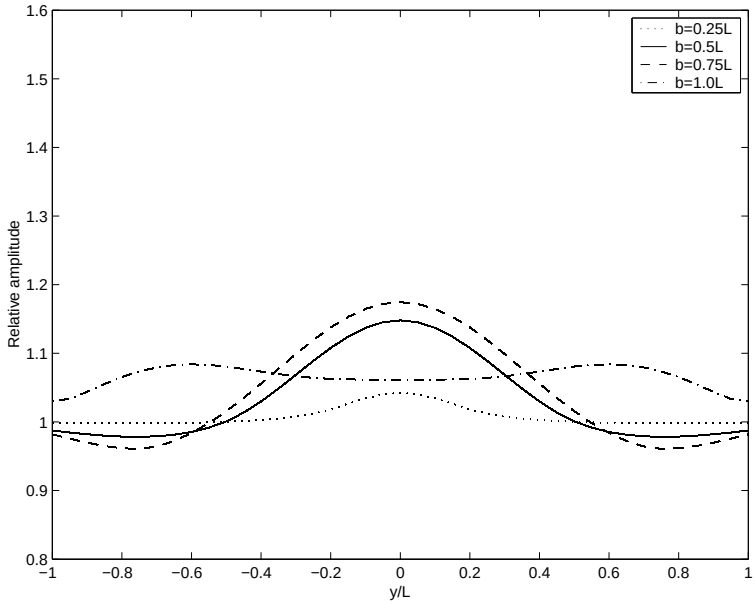

Figure 4.14: Comparison of relative wave amplitudes with $\rho_1/\rho_2 = 3/5$ along the y-axis with b/L varied

4.4 The Mild-slope Equation For The Propagation Of Interfacial Waves In A Two-layer Fluid Model With Higher-order Terms Included

In this Section, we follow Massel [2] and use Galerkin-Eigenfunction Method to derive the extended mild-slope equation with higher-order terms proportional to the bottom slope and bottom curvature included. Like Massel, we also focus our attention to the propagating waves only, leaving the discussion of the evanescent modes to the future work, because these modes only represent localized effect anyway and they disappear exponentially away from the disturbance.

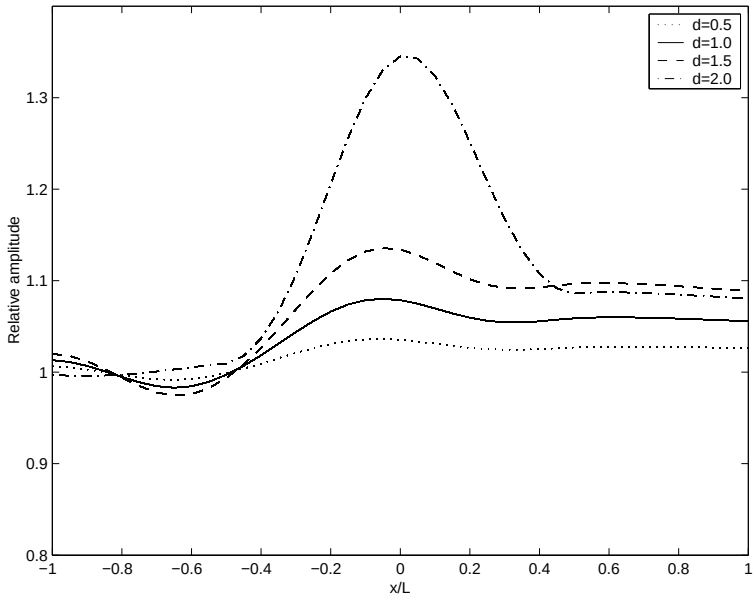

Figure 4.15: Comparison of relative wave amplitudes with $\rho_1/\rho_2 = 3/5$ along the x-axis with d varied

4.4.1 *Derivation for the extended two-layer fluid model*

Considering the solutions of Eqs. (4.2) - (4.7), we expand the $\phi_1(x, y, z)$ and $\phi_2(x, y, z)$ in terms of N depth-dependant functions $f_{1,n}(z)$ and $f_{2,n}(z)$. The functions of $f_{1,n}(z)$ and $f_{2,n}(z)$ are continously differentiable and satisfy the boundary conditions as shown in Eqs. (4.13) - (4.17). Thus, these functions can be written as:

$$f_{1,n}(z) = \frac{\cos(\alpha_n(z - h_1))}{\sin(\alpha_n h_1)} \tag{4.56}$$

$$f_{2,n}(z) = \frac{\cos(\alpha_n(z + h_2))}{\sin(\alpha_n h_2)} \tag{4.57}$$

where $f_{1,n}$ denotes the eigenfunction associated with the upper layer and $f_{2,n}$ denotes the eigenfunction associated with the lower layer as defined in

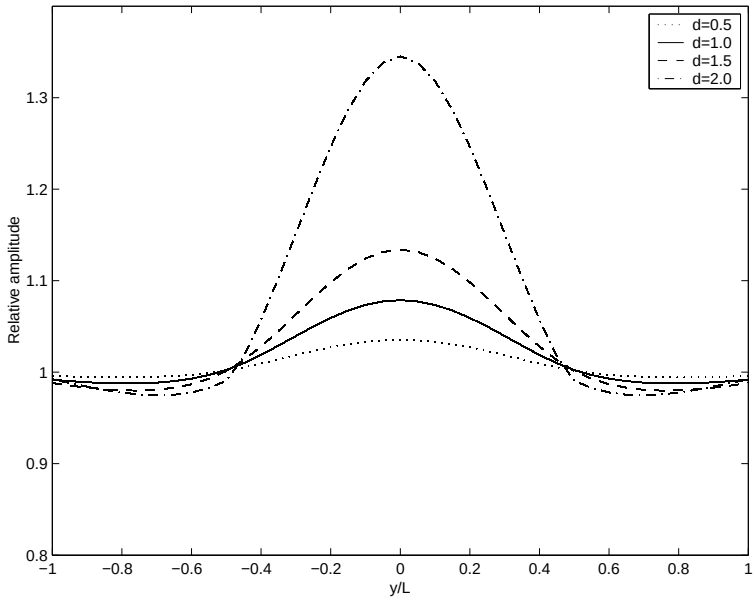

Figure 4.16: Comparison of relative wave amplitudes with $\rho_1/\rho_2 = 3/5$ along the y-axis with d varied

Eq. (4.10) and Eq. (4.11), respectively, and the wave numbers, α_n, are the solution of the following dispersion relation:

$$\lambda = \frac{\omega^2}{g} = \frac{\alpha_n(\rho_2 - \rho_1)}{\rho_1 \coth(\alpha_n h_1) + \rho_2 \coth(\alpha_n h_2)} \tag{4.58}$$

Dispersion relation in Eq. (4.58) has an infinite discrete set of real roots $\pm\alpha_n$ and a pair of imaginary roots $\alpha_0 = \pm ik$. The function with $n = 0$, corresponding to the propagating wave mode, while the function with $n \geq 1$, represent to the evanescent modes. However, as we stated before, the functions corresponding to the evanescent modes will not discussed here, because these modes only represent localized effects and they disappear exponentially away from the disturbance.

Thus, we define an inner product of two functions in the following manner

$$< f_{1,m}, f_{1,n} > \;=\; \int_0^{h_1} (f_{1,m} \cdot f_{1,n}) dz \tag{4.59}$$

$$< f_{2,m}, f_{2,n} > \;=\; \int_{-h_2}^{0} (f_{2,m} \cdot f_{2,n}) dz \tag{4.60}$$

Therefore, we have

$$< f_{1,m}, f_{1,n} > \;= \begin{cases} \frac{h_1}{2sin^2(\alpha_m h_1)}(1 + \frac{sin(2\alpha_m h_1)}{2\alpha_m h_1}), & m = n \\ 0, & m \neq n \end{cases} \tag{4.61}$$

$$< f_{2,m}, f_{2,n} > \;= \begin{cases} \frac{h_2}{2sin^2(\alpha_m h_2)}(1 + \frac{sin(\alpha_m h_2)}{2\alpha_m h_1}), & m = n \\ 0, & m \neq n \end{cases} \tag{4.62}$$

The Galerkin approach assumes that function $\phi_1(x, y, z)$ and $\phi_2(x, y, z)$ can be approximated by an expansion

$$\phi_1(x, y, z) \;=\; \sum_{n=0}^{N} \varphi_{1n}(x, y) f_{1,n}(z) \tag{4.63}$$

$$\phi_2(x, y, z) \;=\; \sum_{n=0}^{N} \varphi_{2n}(x, y) f_{2,n}(z) \tag{4.64}$$

in which the functions $\varphi_{1,n}$ and $\varphi_{2,n}$ should be found from the conditions of orthogonality of functions $f_{1,n}(z)$ and $f_{2,n}(z)$ and the left hand side of Eqs. (4.8) and (4.9) as:

$$\varphi_{1,n}(x, y) \;=\; i\frac{\sigma}{\alpha_n}\eta(x, y) \tag{4.65}$$

$$\varphi_{2,n}(x, y) \;=\; -i\frac{\sigma}{\alpha_n}\eta(x, y) \tag{4.66}$$

Using the orthogonality condition and after substitute Eqs. (4.61) and (4.63) into Eq. (4.2) for the upper layer case, we obtain

$$\sum_{n=0}^{N} < f_{1,m}(z), [\nabla^2(\varphi_{1,n}(x,y)f_{1,n}(z))] > \;\; = \;\; 0 \tag{4.67}$$

or can be written as

$$\int_0^{h_1} (f_{1,m}(z) \sum_{n=0}^{N} [f_{1,n}(z)\nabla^2\varphi_{1,n}\nabla^2 f_{1,n}(z) + 2\nabla\varphi_{1,n}\cdot\nabla f_{1,n}(z) + \varphi_{1,n}\frac{\partial^2 f_{1,n}(z)}{\partial z^2}]) \, dz = 0 \tag{4.68}$$

for $m = 0, 1, ...M$ and $n = 0, 1, ...N$.

Substituting Eq. (4.63) into Eq. (4.3), we then have:

$$\sum_{n=0}^{N} \frac{\partial f_{1,n}}{\partial z}\varphi_{1,n} + f_{1,n}\nabla h_1 \nabla\varphi_{1,n} + \nabla f_{1,n}\cdot\nabla h_1\varphi_{1,n} = 0, \quad at \quad z = h_1(x,y) \tag{4.69}$$

Using Green's formula

$$\int_0^{h_1} f_{1,m}\frac{\partial^2 f_{1,n}}{\partial z^2}dz = -\int_0^{h_1} \frac{\partial f_{1,m}}{\partial z}\frac{\partial f_{1,n}}{\partial z}dz + f_{1,m}\frac{\partial f_{1,n}}{\partial z}|_{z=0}^{z=h_1} \tag{4.70}$$

and the boundary conditions in Eqs. (4.6) and (4.69) into Eq. (4.68), we have

$$\sum_{n=0}^{N}\int_0^{h_1} f_{1,m}f_{1,n}\nabla^2\varphi_{1,n}dz + \int_0^{h_1} 2\nabla\varphi_{1,n}\cdot\nabla f_{1,m}(f_{1,n})dz + \int_0^{h_1}(f_{1,m}\nabla^2 f_{1,n} + f_{1,m}\frac{\partial^2 f_{1,n}}{\partial z^2})\varphi_{1,n}dz = 0 \tag{4.71}$$

This equation can be written in the following matrix form:

$$A_1\nabla^2\varphi_{1,n} + B_1\cdot\nabla\varphi_{1,n} + C_1\varphi_{1,n} = 0 \tag{4.72}$$

where elements of A_1, B_1, and C_1 are defined as:

$$A_1 = \int_0^{h_1} f_{1,m} f_{1,n}\, dz = < f_{1,m}, f_{1,n} > \tag{4.73}$$

$$B_1 = \int_0^{h_1} 2\nabla f_{1,m} f_{1,n} dz = 2\cdot < \nabla f_{1,m}, f_{1,n} > \tag{4.74}$$

$$C_1 = \int_0^{h_1} (f_{1,m}\nabla^2 f_{1,n} + f_{1,m}\frac{\partial^2 f_{1,n}}{\partial z^2})dz$$

$$= < f_{1,m}, \nabla^2 f_{1,n} > + < f_{1,m}, \frac{\partial^2 f_{1,n}}{\partial z^2} > \tag{4.75}$$

The diagonal terms of matrix A_1 ,B_1, and C_1 can be written as

$$a_{1,n,n} = < f_{1,n}, f_{1,n} > \tag{4.76}$$

$$b_{1,n,n} = \nabla(a_{1,n,n}),$$
$$= \frac{\partial a_{1,n,n}}{\partial h_1} + \frac{\chi_{1,n}}{\chi_n}\frac{\partial a_{1,n,n}}{\partial \alpha_n}\nabla h_1 + \frac{\chi_{2,n}}{\chi_n}\frac{\partial a_{1,n,n}}{\partial \alpha_n}\nabla h_2 \tag{4.77}$$

$$c_{1,n,n} = < f_{1,n}, \nabla^2 f_{1,n} > - < \frac{\partial f_{1,n}}{\partial z}, \frac{\partial f_{1,n}}{\partial z} > + f_{1,n}\frac{\partial f_{1,n}}{\partial z}|_{z=h_1}$$
$$- f_{1,n}\frac{\partial f_{1,n}}{\partial z}|_{z=0} \tag{4.78}$$

where

$$\chi_{1,n} = \alpha_n^2(\rho_1 - \rho_1 cot^2(\alpha_n h_1)) \tag{4.79}$$

$$\chi_{2,n} = \alpha_n^2(\rho_2 - \rho_2 cot^2(\alpha_n h_2)) \tag{4.80}$$

$$\chi_n = \rho_1 cot(\alpha_n h_1) + \rho_2 cot(\alpha_n h_2) - \alpha_n\rho_1 h_1 + \alpha_n\rho_1 h_1 cot^2(\alpha_n h_1)$$
$$- \alpha_n\rho_2 h_2 + \alpha_n\rho_2 h_2 cot^2(\alpha_n h_2) \tag{4.81}$$

$$
\begin{aligned}
< f_{1,n}, \nabla^2 f_{1,n} > &= < f_{1,n}, \frac{\partial^2 f_{1,n}}{\partial h_1^2} > (\nabla h_1)^2 + < f_{1,n}, \frac{\partial^2 f_{1,n}}{\partial \alpha_n^2} > (\nabla \alpha_n)^2 \\
&+ 2 < f_{1,n}, \frac{\partial^2 f_{1,n}}{\partial h_1 \partial \alpha_n} > (\nabla h_1)(\nabla \alpha_n) + < f_{1,n}, \frac{\partial f_{1,n}}{\partial h_1} > (\nabla^2 h_1) \\
&+ < f_{1,n}, \frac{\partial f_{1,n}}{\partial \alpha_n} > (\nabla^2 \alpha_n) \qquad (4.82)
\end{aligned}
$$

$$
< \frac{\partial f_{1,n}}{\partial z}, \frac{\partial f_{1,n}}{\partial z} > = \frac{\alpha_n^2 h_1}{2 sin^2(\alpha_n h_1)} (1 - \frac{sin(2\alpha_n h_1)}{2\alpha_n h_1}) \qquad (4.83)
$$

$$
\begin{aligned}
f_{1,n} \frac{\partial f_{1,n}}{\partial z}|_{z=h_1} - f_{1,n} \frac{\partial f_{1,n}}{\partial z}|_{z=0} &= f_{1,n} (\nabla f_{1,n} \nabla h_1)_{z=h_1} \\
&- \lambda cot(\alpha_n h_1) \frac{\rho_2 coth(\alpha_n h_2) + \rho_1 cot(\alpha_n h_1)}{\rho_2 - \rho_1} \qquad (4.84)
\end{aligned}
$$

By using the same approach, we can obtain the equation for the lower layer as:

$$
\begin{aligned}
A_2 &= a_{2,n,n} \\
&= < f_{2,n}, f_{2,n} > \\
&= \frac{h_2}{2sin^2(\alpha_n h_2)}(1 + \frac{sin(2\alpha_n h_2)}{2\alpha_n h_2}) \qquad (4.85)
\end{aligned}
$$

$$
\begin{aligned}
B_2 &= b_{2,n,n} \\
&= \nabla(a_{2,n,n}) \\
&= \frac{\partial a_{2,n,n}}{\partial h_2} + \frac{\chi_{2,n}}{\chi_n}\frac{\partial a_{2,n,n}}{\partial \alpha_n}(\nabla h_2) + (\frac{\chi_{1,n}}{\chi_n}\frac{\partial a_{2,n,n}}{\partial \alpha_n})(\nabla h_1) \qquad (4.86)
\end{aligned}
$$

$$
\begin{aligned}
C_2 &= c_{2,n,n} \\
&= < f_{2,n}, \nabla^2 f_{2,n} > - < \frac{\partial f_{2,n}}{\partial z}, \frac{\partial f_{2,n}}{\partial z} > \\
&+ f_{2,n}\frac{\partial f_{2,n}}{\partial z}|_{z=-h_2} + f_{2,n}\frac{\partial f_{2,n}}{\partial z}|_{z=0} \qquad (4.87)
\end{aligned}
$$

where

$$
\begin{aligned}
< f_{2,n}, \nabla^2 f_{2,n} > &= < f_{2,n}, \frac{\partial^2 f_{2,n}}{\partial h_2^2} > (\nabla h_2)^2 + < f_{2,n}, \frac{\partial^2 f_{2,n}}{\partial \alpha_n^2} > (\nabla \alpha_n)^2 \\
&+ 2 < f_{2,n}, \frac{\partial^2 f_{2,n}}{\partial h_2 \partial \alpha_n} > (\nabla h_2)(\nabla \alpha_n) + < f_{2,n}, \frac{\partial f_{2,n}}{\partial h_2} > (\nabla^2 h_2) \\
&+ < f_{2,n}, \frac{\partial f_{2,n}}{\partial \alpha_n} > (\nabla^2 \alpha_n) \qquad (4.88)
\end{aligned}
$$

$$
< \frac{\partial f_{2,n}}{\partial z}, \frac{\partial f_{2,n}}{\partial z} > = \frac{\alpha_n^2 h_2}{2sin^2(\alpha_n h_2)}(1 - \frac{sin(2\alpha_n h_2)}{2\alpha_n h_2}) \qquad (4.89)
$$

$$
\begin{aligned}
f_{2,n}\frac{\partial f_{2,n}}{\partial z}|_{z=-h_2} + f_{2,n}\frac{\partial f_{2n}}{\partial z}|_{z=0} &= f_{2,n}(\nabla f_{2,n} \nabla h_2)_{z=-h_2} \\
&- \lambda cot(\alpha_n h_2)\frac{\rho_2 cot(\alpha_n h_2) + \rho_1 cot(\alpha_n h_1)}{\rho_2 - \rho_1} \qquad (4.90)
\end{aligned}
$$

Thus, we have two set of equations

$$A_1\nabla^2\varphi_{1,n} + B_1 \cdot \nabla\varphi_{1,n} + C_1\varphi_{1,n} = 0 \tag{4.91}$$

$$A_2\nabla^2\varphi_{2,n} + B_2 \cdot \nabla\varphi_{2,n} + C_2\varphi_{2,n} = 0 \tag{4.92}$$

By letting $n = m = 0$ for propagating wave modes and substituting back Eqs. (4.65) and (4.66) into Eqs. (4.91) and (4.92) and after some algebraic manipulations, we have

$$(A_1 + A_2)\nabla^2\eta + (B_1 + B_2) \cdot \nabla\eta + (C_1 + C_2)\eta = 0 \tag{4.93}$$

where

$$\begin{aligned}(A_1 + A_2) &= g[\frac{\rho_1(kh_1 + coth(kh_1)sinh^2(kh_1))}{ksinh^2(kh_1)(\rho_1 coth(kh_1) + \rho_2 coth(kh_2))} \\ &+ \frac{\rho_2(kh_2 + coth(kh_2)sinh^2(kh_2))}{ksinh^2(kh_2)(\rho_1 coth(kh_1) + \rho_2 coth(kh_2))}] \\ &= CC_g\end{aligned} \tag{4.94}$$

$$\begin{aligned}(B_1 + B_2) &= \nabla(A_1 + A_2) \\ &= \nabla CC_g\end{aligned} \tag{4.95}$$

$$\begin{aligned}(C_1 + C_2) &= k^2CC_g + [\beta_1^{(1)}(\nabla h_1)^2 + \beta_1^{(2)}(\nabla^2 h_1) \\ &\quad +\beta_2^{(1)}(\nabla h_2)^2 + \beta_2^{(2)}(\nabla^2 h_2) + \beta^{(3)}(\nabla h_1 \nabla h_2)]\end{aligned} \tag{4.96}$$

in which $\beta_1^{(1)}, \beta_1^{(2)}, \beta_2^{(1)}, \beta_2^{(2)}$, and $\beta^{(3)}$ are the complicated expressions involving the evaluations of the inner products and products of wave numbers. These expressions are defined as:

$$\beta_1^{(1)} = I_1^{(1)} + (\frac{\chi_{1,0}}{\chi_0^3})^2 I_1^{(2)} + 2(\frac{\chi_{1,0}}{\chi_0^3}) I_1^{(3)} + (\frac{\chi_{3,0}}{\chi_0^3}) I_1^{(4)} + (\frac{\chi_{1,0}}{\chi_0^3})^2 I_2^{(5)} + (\frac{\chi_{3,0}}{\chi_0^3}) I_2^{(4)} - \frac{coth(kh_1)}{sinh^2(kh_1)}(k + h_1 \frac{\chi_{1,0}}{\chi_0}) \quad (4.97)$$

$$\beta_1^{(2)} = I_1^{(5)} + (\frac{\chi_{1,0}}{\chi_0^3}) I_1^{(4)} + (\frac{\chi_{1,0}}{\chi_0^3}) I_2^{(4)} \quad (4.98)$$

$$\beta_2^{(1)} = I_2^{(1)} + (\frac{\chi_{2,0}}{\chi_0^3})^2 I_2^{(2)} + 2(\frac{\chi_{2,0}}{\chi_0^3}) I_2^{(3)} + (\frac{\chi_{4,0}}{\chi_0^3}) I_2^{(4)} + (\frac{\chi_{2,0}}{\chi_0^3})^2 I_1^{(5)} + (\frac{\chi_{4,0}}{\chi_0^3}) I_1^{(4)} - \frac{coth(kh_2)}{sinh^2(kh_2)}(k + h_2 \frac{\chi_{2,0}}{\chi_0}) \quad (4.99)$$

$$\beta_2^{(2)} = I_2^{(5)} + (\frac{\chi_{2,0}}{\chi_0^3}) I_2^{(4)} + (\frac{\chi_{2,0}}{\chi_0^3}) I_1^{(4)} \quad (4.100)$$

$$\beta^{(3)} = 2(\frac{\chi_{1,0}}{\chi_0^3}) I_2^{(3)} + (\frac{\chi_{5,0}}{\chi_0^3}) I_2^{(4)} - h_2 (\frac{\chi_{1,0}}{\chi_0}) \frac{coth(kh_2)}{sinh^2(kh_2)} + 2(\frac{\chi_{2,0}}{\chi_0^3}) I_1^{(3)} + (\frac{\chi_{5,0}}{\chi_0^3}) I_1^{(4)} - h_1 (\frac{\chi_{2,0}}{\chi_0}) \frac{coth(kh_1)}{sinh^2(kh_1)} \quad (4.101)$$

in which $I_1^{(1)}$, $I_1^{(2)}$, $I_1^{(3)}$, $I_1^{(4)}$, $I_1^{(5)}$, $I_2^{(1)}$, $I_2^{(2)}$, $I_2^{(3)}$, $I_2^{(4)}$, and $I_2^{(5)}$ are some inner products while χ_0, $\chi_{1,0}$, $\chi_{2,0}$, $\chi_{3,0}$, $\chi_{4,0}$, and $\chi_{5,0}$ are products of wave numbers, defined in the Appendix A.

If we omit all the terms that contain the higher-order terms, $(\nabla h_1)^2$, $(\nabla^2 h_1)$, $(\nabla h_2)^2$, $(\nabla^2 h_2)$, and $(\nabla h_1 \nabla h_2)$, our results, (Eq. (4.93)), reduce to the mild-slope equations for the two-layer fluid model discussed in Section 4.2 (Eq. (4.22)). And, if we set $\rho_1 = 0$, this equation reduces to the Massel's extended mild-slope equation, as a special case.

4.4.2 *Numerical Solution and Results*

In this section, we shall show some numerical solution results obtained from the extended mild-slope equation for a two-layer fluid model. In order to verify the extended mild-slope equation with higher-order terms included, the new solution is compared with the mild-slope equation with-out the higher-order terms included which is already discussed in the earlier section.

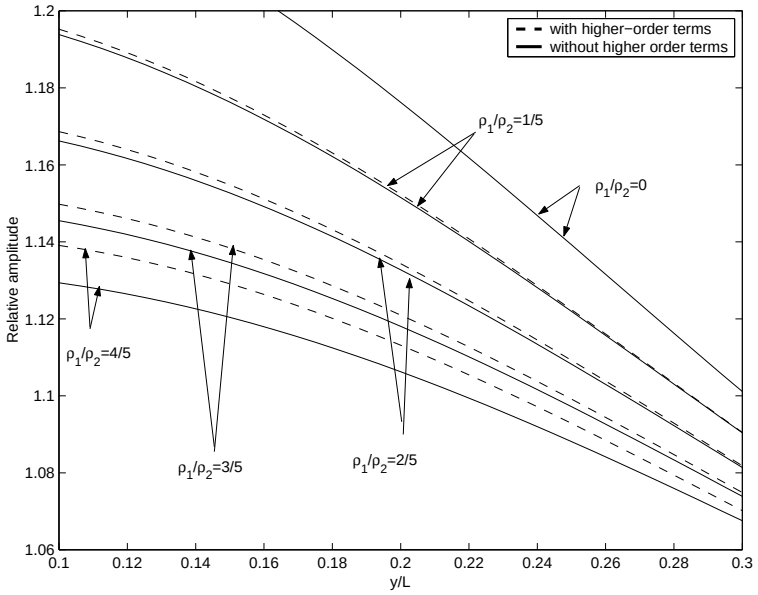

Figure 4.17: Comparison of relative wave amplitudes with high-order terms included(- -) and without high-order terms included (-)

The numerical solution in this section is obtained exactly by following the solution approach described in Section 4.3, except with the higher-order terms included in this solution. Therefore, we set $\rho_1/\rho_2 = 0$, 1/5, 2/5, 3/5, and 4/5 with the hump radius being fixed at $b/L = 0.5$ and $h_{10} = h_{20} = 4.8$. In Fig. 4.17, we display the comparison of relative wave amplitude with and without the higher-order terms included, while Table 4.1 shows the percentage difference between each graph at r=0.1, for each ρ_1/ρ_2 value.

ρ_1/ρ_2	with higher-order	without higher-order	difference percentage%
0	0	0	0
1/5	1.195	1.192	0.086
2/5	1.168	1.160	0.171
3/5	1.150	1.142	0.696
4/5	1.139	1.129	0.878

Table 4.1: Comparison of relative wave amplitude with higher-order and without higher-order terms

From the table, we can obviously seen that, for the special case, i.e $\rho_1/\rho_2 = 0$, the extended mild-slope equation with higher-order terms included reduces to the Massel's extended mild-slope equation, thus no difference is observed. Therefore, the relative wave amplitude for this case is shown to be identical to each other. When the ρ_1/ρ_2 is increased gradually from zero to 4/5, we can see that the relative wave amplitude with the higher-order terms included also becomes larger than that obtained from the mild-slope equation without the higher-order terms as shown in Fig. 4.17 and Table 4.1. This shows that higher-order terms indeed induces more albeit small refraction. However, as can be seen in Table 4.1, the contribution of higher-order terms for the parameter we have chosen here, is very small, usually less than 1%.

4.5 Conclusions

We have derived the mild-slope equation for a two-layer fluid model with the rigid-lid approximation used on the free surface. This analytic solution was derived based on the single-layer mild-slope equation obtained by Smith and

Sprinks [1], and we have found that the single-layer mild-slope equation is the special case for a two-layer mild-slope equation when the density of the upper layer, ρ_1 equal to zero, meaning that the two-layer mild-slope equation should reduce to a single-layer mild-slope equation when $\rho_1 = 0$. We then made a comparison for both solutions, by letting $\rho_1 = 0$ for the two-layer fluid equation, and found that the two solutions were identical and hardly distinguishable, as expected.

Furthermore, we have also examined and discussed the effects of the wave refraction when the ratio of densities, ρ_1/ρ_2 and the ratio of the upper and lower layer water depths, h_{10}/h_{20} are varied. When the ratio of the densities, ρ_1/ρ_2 is increased, the relative wave amplitude decreases. This is because, when ρ_1/ρ_2 increases, the density difference between each layer became smaller, resulting in a weaker restoring force. Thus, the weaker restoring force induces a smaller relative wave amplitude. For the test of the h_{10}/h_{20}, the relative wave amplitude increases with the increasing of h_{10}/h_{20}.

We have also observed and discussed the effect of the hump dimension when the radius, b/L and the height of the hump, d are varied. Here, we found that an increase in the radius and the height of the hump led to an increase of the relative wave amplitude behind the hump as well.

Finally, we have derived an extended the mild-slope equation for the propagation of interfacial waves with higher-order terms proportional to the bottom slope and bottom curvature included. We found that the amplitude of the refracted waves calculated from the equation with the higher-order terms included is slightly higher than that calculated without the higher-order terms.

Chapter 5

Wave diffraction around floating structures

5.1 Overview

In recent years, there has been a great deal of interest in renewable energy resources with regards to combatting climate changes. One of the renewable energy resources comes from ocean waves. Many researchers are astounded by the force and energy extracted from the ocean waves. Renewable analysts believe that the global power potential represented by waves that hit all coastlines worldwide is estimated to provide up to 1 TW (1 terawatt=10^{12} watt) [50]. Therefore, ocean waves represent an enormous source of renewable energy as it is believed that the market potential for energy from the waves is in a very high demand if the technology to extract the energy from waves are successfully developed [51].

A variety of technologies have been proposed to capture the energy from the waves. These technologies can be installed either in onshore or offshore locations. Offshore systems are situated in deep water, typically of more than

40 meters water depth. Whereas, onshore systems are built along shorelines and extract the energy in breaking waves. One of the technologies to extract the energy from ocean waves that is becoming popular among the researchers in the recent years is oscillating water column (OWC) [16]. The OWC consists of a partially submerged concrete or steel structure that has an opening to the sea below the waterline. It encloses a column of air above a column of water. As waves enter the air column, they cause the water column to rise and fall. This alternately compresses and depressurizes the air column. As the wave retreats, the air is drawn back through the turbine as a result of the reduced air pressure on the ocean side of the turbine. Fig. 5.1 is one of the example of an OWC prototype installed by Oceanlinx Limited Australia at Port Kembla, NSW, Australia. This device has successfully converted ocean wave energy into electricity in a number of tests being conducted since it was installed.

Early theories for OWC is introduced by Garret [52], who solved the first-order diffraction problem for a suspended cylinder in ocean of a finite depth. Since then, various mathematical approaches of problems relating to OWC devices have been discussed in the literature over the years. For examples, many authors had presented their work related to a simple two-dimensional OWC models, such as Evans [53, 54], Smith [55], and Sarmento and Falc$\widetilde{a}$o [56]. Recently, Falc$\widetilde{a}$o and Rodrigues [57] and Falc$\widetilde{a}$o [58] had developed a stochastic model to evaluate the average performance of an OWC energy device equipped with Wells turbine.

More recently, Martin-rivas and Mei [15] have carried out a theoretical study of a single OWC being installed at the tip of a breakwater, with vertical circular cylinder open in all direction. In the same year, they also presented the linearized theory of an OWC installed on a straight coast with the vertical

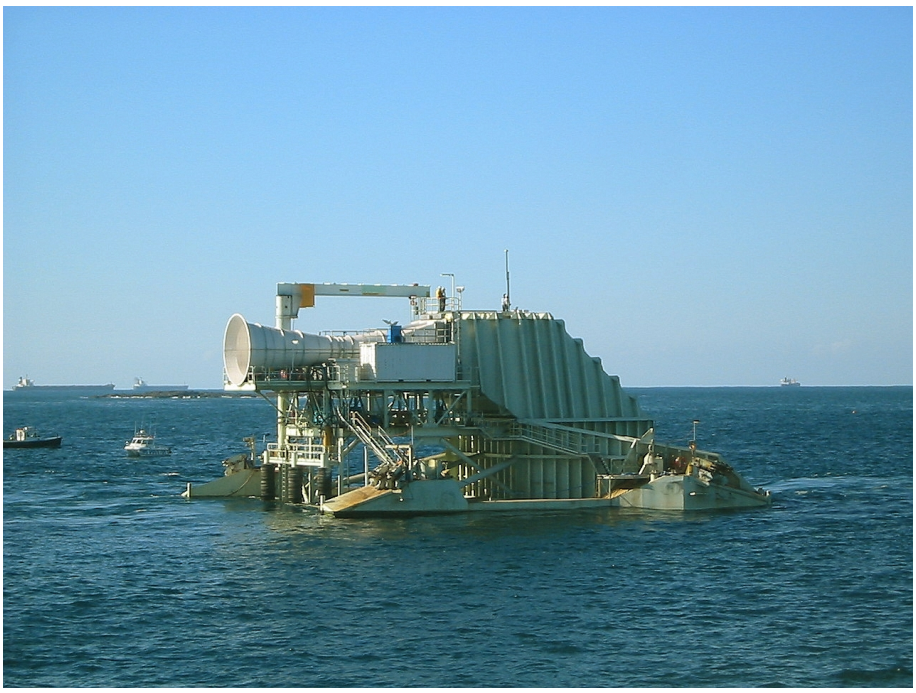

Figure 5.1: An OWC prototype locate at Port Kembla, NSW, Australia

cylinder half embedded in the cliff and open on the seaside [14].

As the last object in this thesis, in this chapter, the mild-slope equation is further extended to be applied to the OWC problem. By removing the rigid lid approximation that we have used in Chapter 4 (for readers information, much of the work described in Chapter 4 have been discussed in Zhu and Harun [12, 13]), the two-layer mild-slope equation for two-layer fluid with free surface on the top is derived. By utilizing this equation, we then construct an analytic solution for long waves propagating over a circular hump located at the bottom of an ocean with a hollow circular cylinder floating on the top of the free surface. Then, in Section 5.3.1, an example is given to compare our new analytic solution in a special case of the two-layer fluid model, i.e $h_2 = 0$ with the solution obtained by Mac Camy and Fuchs [3]. To further verified our solution, we have also compared our solution when the hump

height, d is small enough with the flat bottom in Section 5.3.2. Then, by using the new solution, we then discuss the effects of the hump dimensions and the hollow cylinder structures on the wave diffraction. Finally, the main findings in this chapter will be briefly summarized at the end of this chapter.

5.2 Analytic Solution

In Chapter 4, we have already discussed and presented the analytical solution for two-layer fluid propagating over a circular hump with rigid lid approximation being imposed at the free surface. By using what we have developed before for the two-layer model in the earlier chapter, we then presented the derivation of the mild-slope equation in a two-layer fluid model with free surface on the top by removing the rigid lid approximation that have been discussed earlier in Chapter 4. For the OWC problem, we will treat our case as for a single layer problem. Then, we will used the results that we have derived for the mild-slope equation in a two-layer fluid to solve an OWC problem. The reason that we have solved our problem using the two-layer model is, we need to satisfy all the boundary conditions that exist in this case. By using the two-layer fluid model, it is much easier to determine the boundary condition in both layers. Hence, in this section, first, the two-layer fluid model is presented. Then, we use the result to derive an analytic solution for long waves that are propagating over a circular hump and also over a flat bottom with a hollow cylinder located at the free surface.

5.2.1 *The two-layer fluid model*

Considering a two-layer system depicted in Fig. 5.4, under a Cartesian Coordinate system in which x and y denote a pair of orthogonal horizontal

coordinates and z denotes the vertical coordinate measured positively upwards from the free surface. By assuming that the two fluids are immiscible, the flow within each layer is irrotational, the free surface and the interfacial waves are of small amplitude relative to their wavelength, the velocity potential $\Phi(x, y, z, t)$ can be written as

$$\Phi(x, y, z, t) = \begin{cases} \Phi_1(x, y, z, t), & -h_1 \leq z \leq 0, \\ \Phi_2(x, y, z, t), & -h \leq z \leq -h_1 \end{cases} \tag{5.1}$$

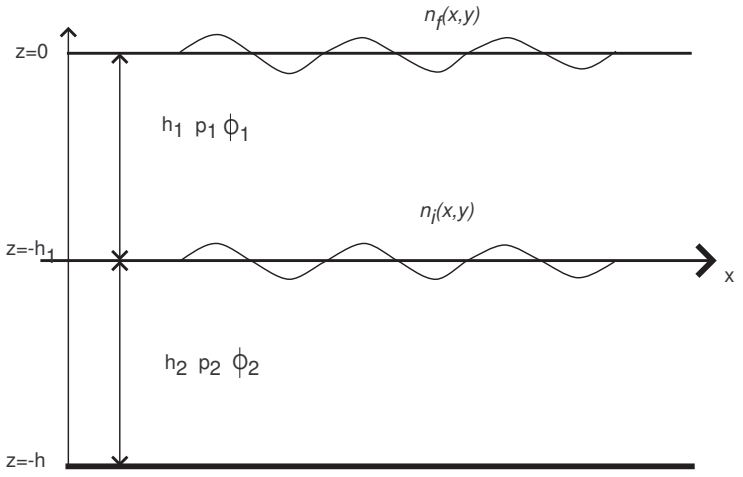

Figure 5.2: A definition sketch for a two-layer fluid with free surface on top

The usual assumptions of the the linearized theory and removal of the harmonic time dependant $e^{-i\omega t}$ lead to the equations for the time dependant velocity potential, $\phi(x, y, z)$

$$\phi(x, y, z) = \begin{cases} \phi_1(x, y, z), & -h_1 \leq z \leq 0, \\ \phi_2(x, y, z), & -h \leq z \leq -h_1 \end{cases} \tag{5.2}$$

These equations therefore can be solved by using the following conditions on all the boundaries of the domain:

$$\frac{\partial^2\phi_1}{\partial z^2} + \nabla^2\phi_1 = 0, \qquad -h_1 \le z \le 0 \tag{5.3}$$

$$\frac{\partial\phi_1}{\partial z} - K\phi_1 = 0, \qquad z = 0 \tag{5.4}$$

$$\frac{\partial\phi_1}{\partial z} = \frac{\partial\phi_2}{\partial z}, \qquad z = -h_1 \tag{5.5}$$

$$\rho_1(\frac{\partial\phi_1}{\partial z} - K\phi_1) = \rho_2(\frac{\partial\phi_2}{\partial z} - K\phi_2), \qquad z = -h_1 \tag{5.6}$$

$$\frac{\partial\phi_2}{\partial z} + \nabla h \cdot \nabla\phi_2 = 0, \qquad z = -h \tag{5.7}$$

$$\frac{\partial^2\phi_2}{\partial z^2} + \nabla^2\phi_2 = 0, \qquad -h \le z \le -h_1 \tag{5.8}$$

where $K = \omega^2/g$, $\nabla = (\partial/\partial x, \partial/\partial y)$, g is the gravitational acceleration, and the densities and the waves heights of the upper and lower fluid layers are denoted by ρ_1, h_1, and ρ_2, h_2 respectively, with $\rho_1 \le \rho_2$ and $h = h_1 + h_2$.

Using the separation of variables, we set $\phi_j(x, y, z) = X_j(x, y)Z_j(z)$, in the equations above, where j= 1,2, and we obtained

$$\frac{\partial^2 Z_1}{\partial z^2} - k^2 Z_1 = 0, \qquad -h_1 \le z \le 0 \tag{5.9}$$

$$\frac{\partial Z_1}{\partial z} - K Z_1 = 0, \qquad z = 0 \tag{5.10}$$

$$\frac{\partial Z_1}{\partial z} = \frac{\partial Z_2}{\partial z}, \qquad z = -h_1 \tag{5.11}$$

$$\rho_1(\frac{\partial Z_1}{\partial z} - K Z_1) = \rho_2(\frac{\partial Z_2}{\partial z} - K Z_2), \qquad z = -h_1 \tag{5.12}$$

$$\frac{\partial Z_2}{\partial z} = 0, \qquad z = -h \tag{5.13}$$

$$\frac{\partial^2 Z_2}{\partial z^2} - k^2 Z_2 = 0, \qquad -h \le z \le -h_1 \tag{5.14}$$

a direct solution for these equations are

$$Z_1 = k\ \cosh(kz) + K\ \sinh(kz), \qquad -h_1 \le z \le 0 \tag{5.15}$$

$$Z_2 = \frac{K\cosh(kh_1) - k\ \sinh(kh_1)}{\sinh(kh_2)}\cosh(k(z+h)), \qquad -h \le z \le -h_1 \tag{5.16}$$

with the wave number k satisfying the dispersion relation

$$\omega^4(\rho_1 + \rho_2\coth(kh_1)\coth(kh_2)) - \omega^2 gk\rho_2(\coth(kh_1) + \coth(kh_2) + g^2k^2(\rho_2 - \rho_1) = 0 \tag{5.17}$$

Since Eq. (5.17) is a quadratic in ω^2, there are two possible roots of ω. These two roots correspond to each layer of the fluids, one is for the upper layer and another one is for the lower layer. Eq. (5.17) can also be reduced to a single-layer fluid when $\rho_1 = \rho_2$ [33].

5.2.2 *The Mild-slope equation in a two-layer fluid model*

By assuming that the variation of water depth is moderate, the velocity potential can be written as

$$\phi_1(x,y,z) = i\frac{g}{\omega}\eta_f Z_1, \qquad -h_1 \le z \le 0 \tag{5.18}$$

$$\phi_2(x,y,z) = i\frac{g}{\omega}\eta_i Z_2, \qquad -h \le z \le -h_1 \tag{5.19}$$

and the relationship between η_f and η_i is given by

$$\frac{\eta_f}{\eta_i} = \frac{K}{k\sinh(kh_1) - K\cosh(kh_1)} \tag{5.20}$$

with η_f and η_i are the free surface waves elevation and interfacial waves elevation, respectively (the full derivation for Eq. (5.20) can be find in Appendix C). Then, η_f and η_i can be written as

$$\eta_f = a_i e^{i(kx-\omega t)}, \qquad -h_1 \leq z \leq 0 \tag{5.21}$$

$$\eta_i = b_i e^{i(kx-\omega t)}, \qquad -h \leq z \leq -h_1 \tag{5.22}$$

where a_i and b_i are the incident wave amplitudes for the free and interfacial waves respectively.

Considering Eq. (5.9) and Eq. (5.14) as an ordinary differential equation in z, and applying the integration by substitution, we have

$$\begin{aligned} &\int_{-h_1}^{0} (k^2\phi_1 Z_1 + Z_1\nabla^2\phi_1)dz + \int_{-h}^{-h_1} (k^2\phi_2 Z_2 + Z_2\nabla^2\phi_2)dz \\ &= -(Z_1\nabla h_1 \cdot \nabla\phi_1)_{z=0} - (Z_2\nabla h \cdot \nabla\phi_2)_{-h} \end{aligned} \tag{5.23}$$

By calculating $\nabla\phi_1$, $\nabla^2\phi_1$, $\nabla\phi_2$, and $\nabla^2\phi_2$ from Eqs. (5.18) and (5.19), then substituting back into Eq. (5.23), we have obtained by neglecting the higher-order terms, the equation for the free surface waves as

$$\nabla \cdot (A_1 \cdot \nabla\eta_f) + k^2 A_1\eta_f + \nabla \cdot (A_2 \cdot \nabla\eta_i) + k^2 A_2\eta_i = 0 \tag{5.24}$$

where

$$\begin{aligned} A_1 &= \int_{-h}^{0} Z_1^2 dz \\ &= \frac{1}{2k^3}(k^2\cosh(kh_1)\sinh(kh_1) + k^3h_1 - 2Kk(\cosh(kh_1))^2 \\ &\quad +K^2\cosh(kh_1)\sinh(kh_1) - K^2kh_1 + 2Kk) \end{aligned} \tag{5.25}$$

$$\begin{aligned} A_2 &= \int_{-h}^{-h_1} Z_2^2 dz \\ &= \frac{(\cosh(kh_2)\sinh(kh_2) + kh_2)}{2\ k^3(\sinh(kh_2))^2}(k\sinh(kh_1) - K\cosh(kh_1))^2 \end{aligned} \tag{5.26}$$

At the interface, by utilizing Eq.(5.19), and following the derivation for mild-slope equation just as we did before, we have

$$\nabla\cdot[(\int_{-h}^{-h_1} Z_2^2 dz)\nabla\cdot\eta_i] + k^2(\int_{-h}^{-h_1} Z_2^2 dz)\eta_i = 0 \tag{5.27}$$

or can be written as

$$\nabla\cdot A_2\nabla\cdot\eta_i + k^2A_2\eta_i = 0 \tag{5.28}$$

Eqs. (5.24) and (5.28) are the mild-slope equation for the two-layer fluid model with the free surface on the top. These equations can be reduced to a single-layer mild-slope equation derived by Smith and Sprinks [1], when $\rho_1 = \rho_2$. Thus, the single-layer mild-slope equation is a special case for two-layer mild-slope equation, as we have expected.

5.2.3 *Wave diffraction around floating structure over a variable water depth*

Now, consider a train of plane long waves which propagates in two-layer fluids with constant water depth h_{10} and h_{20} and is refracted by an axi-symmetric

hump-shaped shoal located on the ocean floor and diffracted by a hollow cylinder located at the free surface of the upper layer.

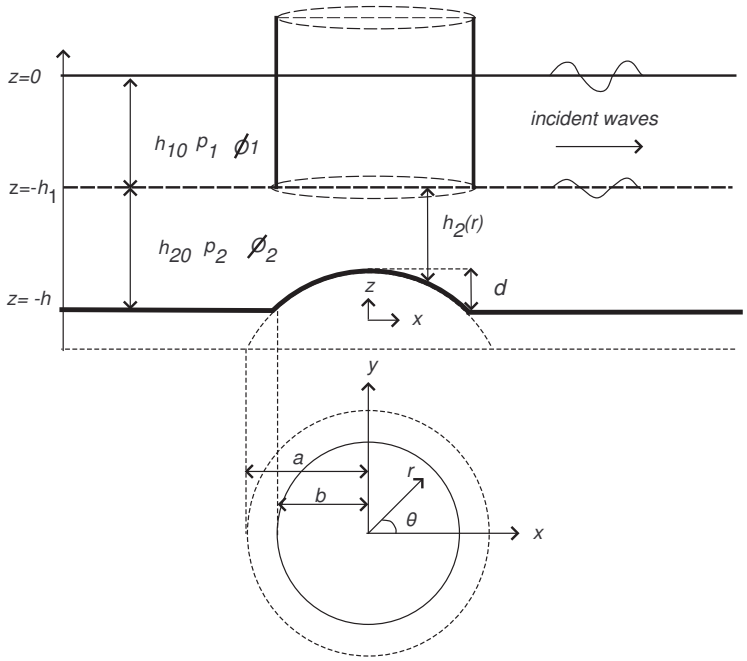

Figure 5.3: A definition sketch of a hump located on the floor in a two-layer fluid system

The cross-section of the hump is of the shape of a parabola and the surface of the hump is formed through revolving the parabola around the vertical axis of revolution, which is marked with the z coordinate of a Cartesian coordinate system chosen with its origin located at the center of the hump as demonstrated in Fig. 5.7. The parabolic hump surface intersects with the ocean floor at $z = -h$, resulting in a circle with its radius denoted as b, and the height of the hump is controlled by a parameter d as shown in Fig. 5.7. In this figure, we assume that the radius of the cylinder is the same as the radius of the hump. This assumption is made to simplify the calculation of this problem. However, the same methodology can be expanded by

making the hump radius bigger or smaller than the radius of the cylinder. In the corresponding cylindrical coordinate system with r being the radial distance from the origin and θ being the angle measured counterclockwise from the positive $x-$axis, the water depth for the lower layer is prescribed by a parabolic function

$$h_2 = \begin{cases} (h_{20} - d)(1 + \frac{r^2}{a^2}), & r < b \\ h_{20}, & r \geq b \end{cases} \tag{5.29}$$

In Eq. (5.29), a is determined by $a = b\sqrt{\frac{(h_{20}-d)}{d}}$, for a given set of d and h_{20} and $a > b$. Therefore, geometrically, a is the radius of the cross-sectional circle of the paraboloid intersecting with a horizontal plane located below the seabed. While d is used to control the height of the hump, either b or a is used to control the horizontal dimension of the hump.

As we have already mentioned at the beginning of this section, in order to solve the OWC problem, we have treated our case as a single-layer fluid problem. The reason that we have solved our problem using the two-layer model is, we need to satisfy all the boundary conditions that exist in this case. By using the two-layer fluid model, it is much easier to determine the boundary condition in both layers. Then, we used the two-layer fluid equation that we have derived above, to determine all the boundary conditions that have being imposed in this case.

By setting $\rho_1 = \rho_2$, for the lower layer, the solution that we have here is similar to the solution that we have already discussed in Chapter 3. Therefore, in this chapter, we only present the final solution as all the calculation details already presented in Chapter 3. So, for the lower layer, we have the

solution of the form

$$\eta_i^{out} = \sum_{n=0}^{\infty}(b_i\ i^n\ \epsilon_n J_n(kr) + D_n H_n^{(1)}(kr))\cos n\theta, \tag{5.30}$$

$$\eta_i^{in} = \sum_{n=0}^{\infty} B_n R_n(r)\cos n\theta, \tag{5.31}$$

where

$$R_n(r) = \sum_{n=0}^{\infty}\alpha_{m,n}\ r^{m+n} \tag{5.32}$$

$$B_n = b_i k i^n \varepsilon_n \frac{J_n(kb)H_n'^{(1)}(kb) - J_n'(kb)H_n^{(1)}(kb)}{kR_n(b)H_n'^{(1)}(kb) - R_n'(b)H_n^{(1)}(kb)}, \tag{5.33}$$

$$D_n = b_i i^n \varepsilon_n \frac{kJ_n'(kb)R_n(b) - J_n(kb)R_n'(b)}{H_n^{(1)}(kb)R_n'(b) - kH_n'^{(1)}(kb)R_n(b)}, \tag{5.34}$$

and the solution for $\alpha_{m,n}$ is obtained by using the Frobenius series solution and is in the form of

$$\alpha_{0,n} = 1, \tag{5.35}$$

$$\alpha_{1,n} = 0, \tag{5.36}$$

$$\alpha_{m+2,n} = \frac{-[(m+n)(m+n+2)+v^2-n^2]}{a^2(m+2)(m+2n+2)}\alpha_{m,n}, \tag{5.37}$$

and $m = 0,\ 1,\ 2,\ ...$

For the upper layer, by using the separation of variables and writing Eq. (5.24) in a cylindrical coordinate systems (r, θ, z) with $x = r\cos(\theta)$ and $y = r\sin(\theta)$, we have

$$\begin{aligned} &A_1(r^2R_{1,n}''(r) - rR_{1,n}'(r) + (k^2r^2 - n^2)R_{1,n}(r)) + \\ &A_2(R_n''(r) + \frac{1}{r}R_n'(r) - \frac{n^2}{r^2}R_n(r)) + \frac{dA_2}{dr}R_n'(r) + k^2A_2R_n(r) = 0 \end{aligned} \tag{5.38}$$

or can be written as

$$A_1(r^2R''_{1,n}(r) - rR'_{1,n}(r) + (k^2r^2 - n^2)R_{1,n}(r)) =$$
$$-(A_2(R''_n(r) + \frac{1}{r}R'_n(r) - \frac{n^2}{r^2}R_n(r)) + \frac{dA_2}{dr}R'_n(r)$$
$$+k^2A_2R_n(r)) \tag{5.39}$$

Eq. (5.39) is the non-homogeneous ordinary differential equation with variable coefficients. This equation can be solved using the method of variations parameters. By finding the complementary solution and the particular solution for Eq. (5.39), and utilizing the solution obtained from the lower region, we then have the solution for $R^{in}_{1,n}$ inside the cylinder as

$$\begin{aligned} R^{in}_{1,n} \quad &= C_{9,n}J_n(kr) + C_{10,n}Y_n(kr) - Y_n(kr)\int_0^r \frac{\pi r B_n R_n(r) J_n(kr)}{2} dr \\ &+ J_n(kr)\int_0^r \frac{\pi r B_n R_n(r) Y_n(kr)}{2} dr \end{aligned} \tag{5.40}$$

We know that, at the origin, $Y_n(kr)$ is infinite, so we choose $C_{10,n} = 0$. Thus, Eq. (5.40) becomes

$$\begin{aligned} R^{in}_{1,n} \quad &= C_{9,n}J_n(kr) - Y_n(kr)\int_0^r \frac{\pi r B_n R_n(r) J_n(kr)}{2} dr \\ &+ J_n(kr)\int_0^r \frac{\pi r B_n R_n(r) Y_n(kr)}{2} dr \end{aligned} \tag{5.41}$$

where $B_nR_n(r)$ is the result from the lower layer. At $r = b$, in the upper layer, we have the solid wall, therefore, this condition is required

$$\frac{\partial \eta^{in}_f}{\partial r} = 0 \tag{5.42}$$

implying that

$$\frac{dR^{in}_{1,n}}{dr} = 0. \tag{5.43}$$

By differentiating Eq. (5.41) and substituting it into Eq. (5.43), we then can determine $C_{9,n}$ as

$$C_{9,n} = \frac{Y_n'(kb)}{J_n'(kb)} \int_0^b \frac{\pi r B_n R_n(r) J_n(kr)}{2} dr - \int_0^b \frac{\pi r B_n R_n(r) Y_n(kr)}{2} dr \quad (5.44)$$

By substituting back Eq.(5.44) into Eq. (5.41), the solution for the inner region of the upper layer, can now be solved. However, we have noticed from Eq. (5.41), that the term involving $Y_n(kr)$ is singular at the origin. But by taking the limit of this term using the L'hophital rules, we can show that, this term approaches zero when $r = 0$. The detailed calculation is shown in Appendix B.

For the region outside the cylinder in the upper layer, the solution is

$$\begin{aligned} R_{1,n}^{out} \quad &= D_{1,n} J_n(kr) + D_{2,n} H_n(kr) - H_n(kr) \int_b^r \frac{i\pi r D_n H_n(kr) J_n(kr)}{2} dr \\ &+ J_n(kr) \int_b^r \frac{i\pi r D_n H_n(kr) H_n(kr)}{2} dr \end{aligned} \quad (5.45)$$

at $r = \infty$, Eq. (5.45) should satisfies the Sommerfeld radiation condition [59], which is in the form of

$$\lim_{r\to\infty} \sqrt{kr} \{ \frac{dR_{1,n}^{out}}{dr} - ikR_{1,n}^{out} \} = 0 \quad (5.46)$$

As already known, the terms involving Hankel Function, $H_n(kr)$ with any constant, i.e $D_{2,n}$ already satisfies the radiation condition [59]. Therefore, by

substituting Eq.(5.45) into Eq. (5.46), we then have

$$\begin{aligned}
\lim_{r\to\infty}\sqrt{kr}\{\frac{dR^{out}_{1,n}}{dr}-ikR^{out}_{1,n}\} &= \lim_{r\to\infty}\sqrt{kr}\{D_{1,n}J'_n(kr) \\
&\quad - H'_n(kr)\int_b^r \frac{i\pi r D_n H_n(kr)J_n(kr)}{2}dr \\
&\quad + J'_n(kr)\int_b^r \frac{i\pi r D_n H_n(kr)H_n(kr)}{2}dr \\
&\quad - i\ k\ (D_{1,n}J_n(kr) \\
&\quad -H_n(kr)\int_b^r \frac{i\pi r D_n H_n(kr)J_n(kr)}{2}dr \\
&\quad + J_n(kr)\int_b^r \frac{i\pi r D_n H_n(kr)H_n(kr)}{2}dr)\} \\
&= \lim_{r\to\infty}\sqrt{kr}\{[J'_n(kr)-ikJ_n(kr)] \\
&\quad (D_{1,n}+\int_b^r \frac{i\pi r D_n H_n(kr)H_n(kr)}{2}dr) \\
&\quad - [H'_n(kr)+ikH_n(kr)] \\
&\quad \int_b^r \frac{i\pi r D_n H_n(kr)J_n(kr)}{2}dr\} \\
&= 0 \qquad (5.47)
\end{aligned}$$

Knowing that

$$\lim_{r\to\infty}\sqrt{kr}[H'_n(kr)-ikH_n(kr)]=0 \qquad (5.48)$$

implying that only terms associated to $J_n(kr)$ is left. Thus, these terms also should go to zero in order to satisfy the radiation condition at the infinity. So then, we have

$$\lim_{r\to\infty}\sqrt{kr}[J'_n(kr)-ikJ_n(kr)](D_{1,n}+\int_b^r \frac{i\pi r D_n H_n(kr)H_n(kr)}{2}dr)=0 \qquad (5.49)$$

Thus,

$$D_{1,n}=-\int_b^\infty \frac{i\pi r D_n H_n(kr)H_n(kr)}{2}dr \qquad (5.50)$$

In the upper layer, at $r=b$, once again, the condition

$$\partial\eta_f^{out}/\partial r=0 \qquad (5.51)$$

is applied, because there is a solid cylinder wall being placed in here. Using this condition and substituting back Eq. (5.50) into Eq. (5.45) we then determined

$$D_{2,n} = -(a_i i^n \epsilon_n + D_{1,n}) \frac{J'_n(kr)}{H'_n(kr)} \tag{5.52}$$

By substituting back these coefficients into Eq. (5.45), the water surface elevation for the upper layer now can be solved. If we set $h_{20} = 0$, for $d \geq 0$, in Eq. (5.45), we found that the inhomogeneous terms in this equation and the lower layer equation are vanished, resulting in only the Hemholtz equation. As a result, Eq. (5.45) also reduces to Mac Camy and Fuchs [3] solution. Thus, the Mac Camy and Fuchs solution [3] is a special case for our solution when $h_{20} = 0$, as we have expected.

5.2.4 *Wave diffraction around floating structure over a flat bottom*

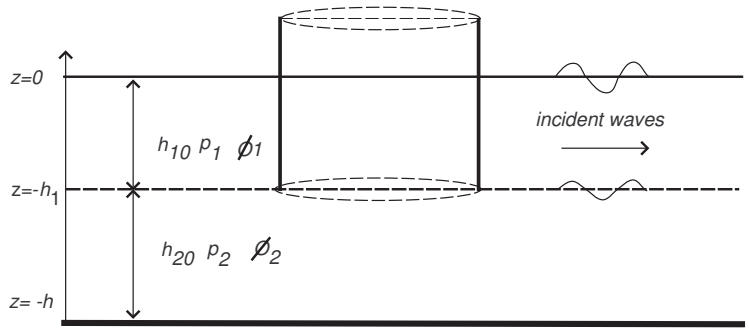

Figure 5.4: A definition sketch of a hollow circular cylinder floating on the upper layer in a two-layer fluid system

When the hump is being removed from the ocean floor, there is no more obstacle or barrier in the lower layer region, making it a special case for

variable water depth. Hence, the equation for the lower layer region can be simplified to the constant water depth or Hemholtz equation, making it a lot more easier to be solved. Thus, our lower layer equation now is in the form of

$$\nabla^2\eta + k^2\nabla\eta = 0 \tag{5.53}$$

For the inner region, $r < b$, the solution for this equation is given by [3]

$$\eta_i^{in} = \sum_{n=0}^{\infty}(C_{1,n}J_n(kr) + C_{2,n}Y_n(kr))\cos(n\theta) \tag{5.54}$$

where $Y_n(kr)$ is the Bessel function of the second kind, because $Y_n(kr)$ is singular at the origin, we set $C_{2,n} = 0$. Therefore, for the inner region of the lower layer, our solution is

$$\eta_i^{in} = \sum_{n=0}^{\infty} C_{1,n}J_n(kr)\cos(n\theta) \tag{5.55}$$

For the outer region, our solution is given by

$$\eta_i^{out} = \sum_{n=0}^{\infty}(b_i i^n \epsilon_n J_n + C_{3,n}H_n(kr))\cos(n\theta) \tag{5.56}$$

where $C_{1,n}$ and $C_{3,n}$ are constants to be determined.

At $r = b$ in the lower layer, the matching condition required, thus, by using the equation of continuity like we did in Chapter 3 and 4, we obtained

$$C_{1,n} = b_i i^n \epsilon_n \tag{5.57}$$

$$C_{3,n} = 0 \tag{5.58}$$

By substituting these coeeficients back into Eqs. (5.55)and (5.56), we have

$$\eta_i = \sum_{n=0}^{\infty} b_i i^n \epsilon_n J_n \cos(n\theta) \tag{5.59}$$

which is the equation for the plane waves. On the other hand, for the upper layer of the inner region (inside the cylinder), we have

$$\begin{aligned} R_{1,n}^{in} \quad &= C_{5,n}J_n(kr) + C_{6,n}Y_n(kr) - Y_n(kr)\int_0^r \frac{\pi r C_{1,n}(J_n(kr))^2}{2}dr \\ &+ J_n(kr)\int_0^r \frac{\pi r C_{1,n}J_n(kr))Y_n(kr)}{2}dr \end{aligned} \tag{5.60}$$

Once again, we set $C_{6,n} = 0$, because $Y_n(kr)$ is singular at the origin. Therefore, we have

$$\begin{aligned} R_{1,n}^{in} \quad &= C_{5,n}J_n(kr) - Y_n(kr)\int_0^r \frac{\pi r C_{1,n}(J_n(kr))^2}{2}dr \\ &+ J_n(kr)\int_0^r \frac{\pi r C_{1,n}J_n(kr))Y_n(kr)}{2}dr \end{aligned} \tag{5.61}$$

For the upper layer, at $r = b$, as already known, there is a solid cylinder wall. Hence, the condition that we have to satisfy is $dR_{1,n}/dr = 0$. Thus, we obtained the coefficient for $C_{5,n}$ as

$$C_{5,n} = \frac{Y_n'(kr)}{J_n'(kr)}\int_0^r \frac{\pi r C_{1,n}(J_n(kr))^2}{2}dr - \int_0^r \frac{\pi r C_{1,n}J_n(kr))Y_n(kr)}{2}dr \tag{5.62}$$

For the outer region ($r \geq b$), following the steps that we obtained for Eq. (5.45), we have

$$\begin{aligned} R_{1,n}^{out} \quad &= C_{7,n}J_n(kr) + C_{8,n}H_n(kr) - H_n(kr)\int_0^r \frac{\pi r C_{3,n}H_n(kr))J_n(kr)}{2}dr \\ &+ J_n(kr)\int_0^r \frac{\pi r C_{3,n}H_n(kr))H_n(kr)}{2}dr \end{aligned} \tag{5.63}$$

From Eq. (5.58), we know that $C_{3,n} = 0$, implying that $C_{7,n} = 0$. Thus, the only coefficient left is

$$R_{1,n}^{out} = C_{8,n}H_n(kr) \tag{5.64}$$

Therefore, the water surface elevation, for the free surface in the outer region can be written as

$$\eta_f^{out} = \sum_{n=0}^{\infty}((a_i i^n \epsilon_n J_n(kr) + C_{8,n} H_n(kr))\cos(n\theta) \tag{5.65}$$

Once again, for the upper layer, at $r = b$, this condition

$$\partial \eta_f^{out}/\partial r = 0 \tag{5.66}$$

is applied. Therefore, we can determine $C_{8,n}$ as

$$C_{8,n} = -a_i i^n \epsilon_n \frac{J_n'(kr)}{H_n'(kr)} \tag{5.67}$$

Having obtained all the coefficients that need to be determined, the entire domain now can be computed. Some results of specific calculations are presented in the next section.

5.3 Results and Discussions

In this section, an example is presented to compare the new analytic solution for a special case of our solution, that is taking $h_2 = 0$, with the solution for plane waves diffracted by a large surface-piercing vertical circular cylinder in an open sea of constant depth discussed in Mac Camy and Fuchs [3]. Then, we compare our solution with the very tiny little hump with a flat bottom on the seafloor, as part of the verification process. Finally, using the new solution, the effects of the cylinder and hump dimensions on the wave refraction and diffraction process is discussed.

5.3.1 *Comparison with the Mac Camy and Fuchs Solutions*

Since the mild-slope equation for a two-layer fluid model should be reduced to the Hemholtz Equations model when $h_{20} = 0$, it would be interesting to

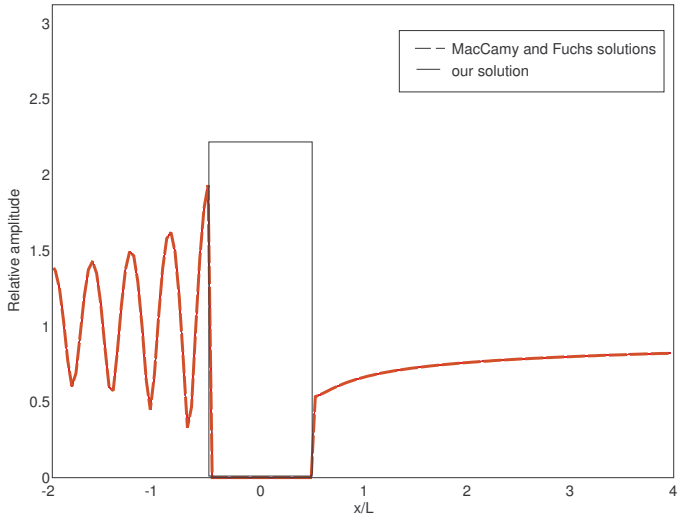

Figure 5.5: Comparison of relative wave amplitudes between MacCamy and Fuchs solution and our solution when $h_{20} = 0$ along x-axis

compare both models, as part of the verification process.

We set $h_{10} = 2.4$ and $h_{20} = 0$, and take the remaining parameters exactly the same as those used in single-layer fluid model discussed in Zhu and Harun [11], i.e, $b/L = 0.5$, and the wave length, $L = 120.4$. Since, the analytic solution for η involves an infinite series, it must be truncated for the purpose of numerical solution, so we set $N = 70$ and $M = 30$, because the solution had already converged with these values. The Bessel and Hankel functions in the analytical solution were computed using the built-in subroutines in MATLAB.

Fig. 5.5 and Fig. 5.6 show the comparison of the relative wave amplitudes along the x- and y-axes respectively for the two and single-layer fluid models. The results in this comparison are presented in terms of dimensionless coordinates, x/L and y/L and the center of the hump is located at the origin. As expected, both solutions are identical and hardly distinguishable.

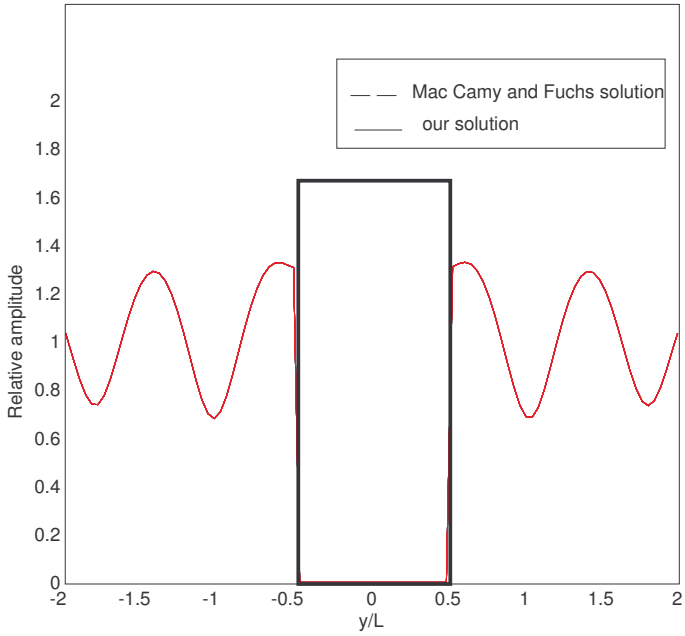

Figure 5.6: Comparison of relative wave amplitudes between MacCamy and Fuchs solution and our solution when $h_{20} = 0$ along y-axis

With the excellent agreement between these solutions, we are confident that the derivation of our new analytical solution is correct.

5.3.2 *Comparison with the flat bottom*

As we already know, the flat bottom is the special case for the variable water depth with hump is located on the sea floor. Therefore, to gain confidence for the non-flat-bottom solution, and in order to further verify the newly derived equation, we have compared the solution that we obtained from the flat bottom with the solution with a very small size hump, $d = 10^{-6}$ being placed on the seabed.

The comparison for these two problems is shown in Figs. 5.8 and 5.9 respectively. As can been seen, both figures are identical and can't be dis-

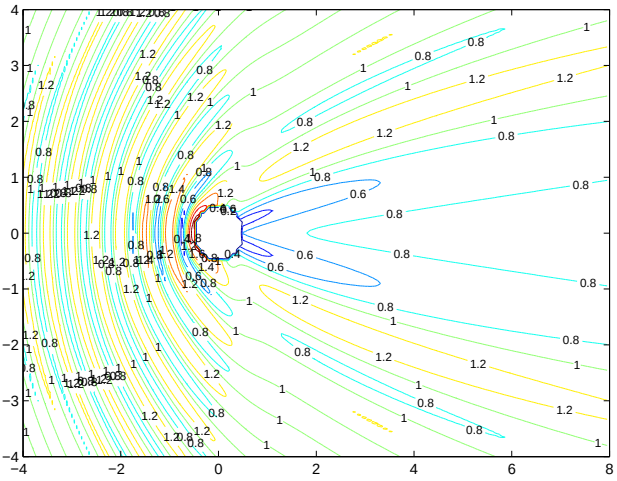

Figure 5.7: A definition sketch of a hump located on the floor in a two-layer fluid system

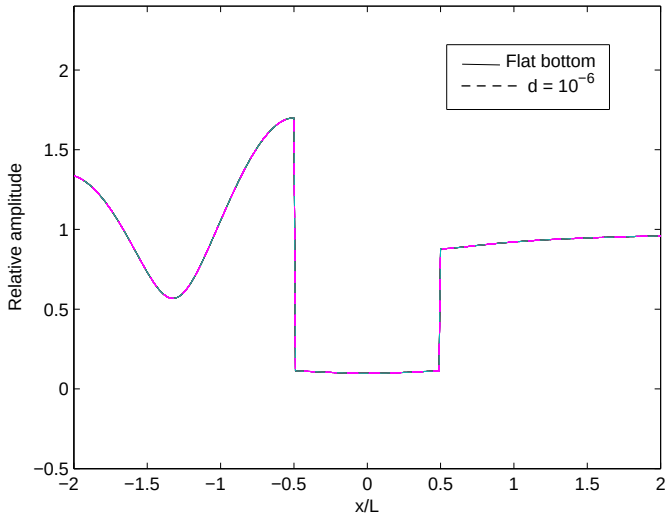

Figure 5.8: Comparison of relative wave amplitudes between the flat sea bottom and tiny little hump along the x-axis

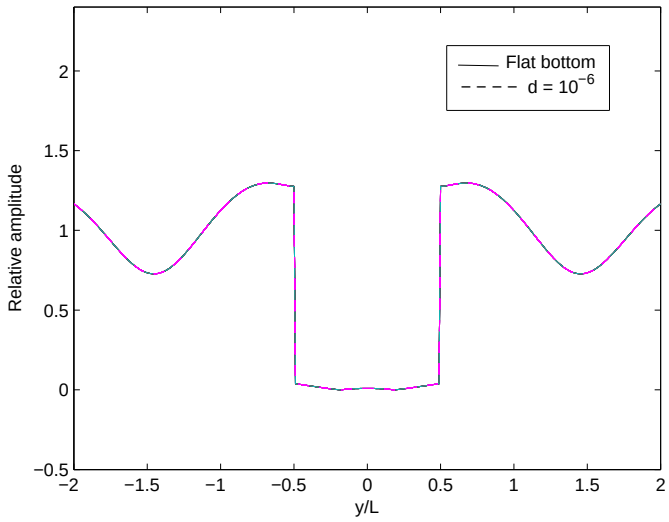

Figure 5.9: Comparison of relative wave amplitudes between the flat sea bottom and tiny little hump along the y-axis

tinguished. Therefore, this adds to our confidence that our derivation was derived correctly. In addition, for the flat bottom case, we discovered that it seemed like there was a plane wave propagating inside the cylinder because based on our derivation, the lower layer is presented by the plane waves (cf. Eq. (5.59)).

5.3.3 *Effect of the cylinder height*

In this section, we discuss the effect of the wave refraction when the height of the cylinder, h_{10}, is varied, while other parameters are held constant.

To examine this, we set $h_{10} = 2.4$, 4.8, and 7.2 with the hump radius being fixed at $b/L = 0.5$, $d/L = 0.5$ and $h_{20} = 4.8$. The comparisons for each value of h_{10} along the x- and y-axes are shown in Fig. 5.10 and Fig. 5.11, respectively. It can be obviously seen that, an increase in the height of the cylinder, h_{10}, results in a larger relative wave amplitudes. From both figures,

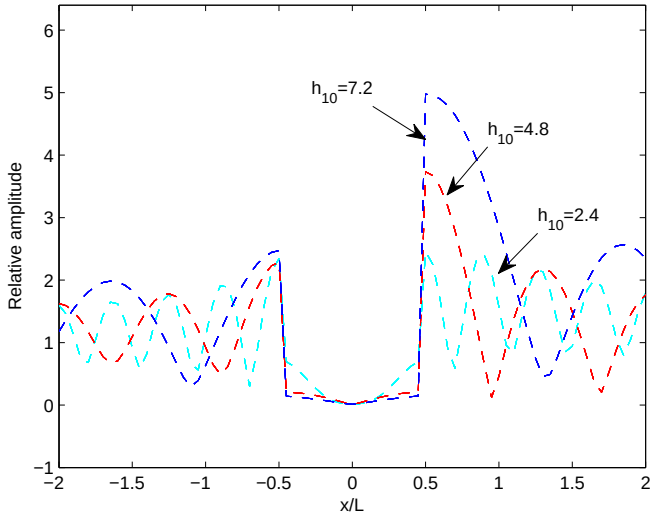

Figure 5.10: Comparison of relative wave amplitudes when h_{10} are varied along the x-axis

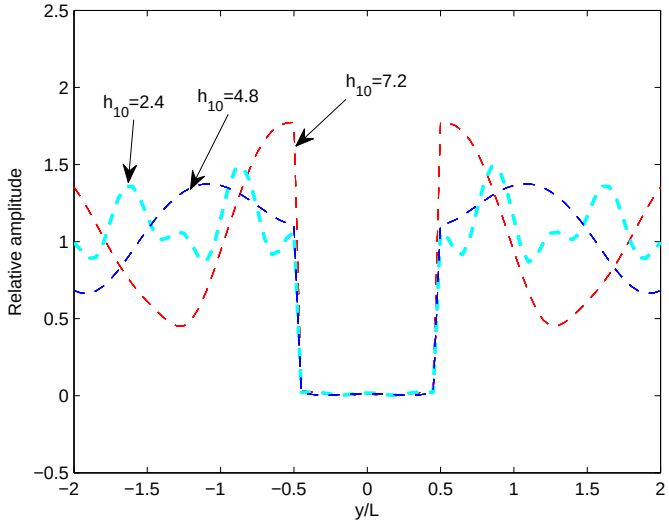

Figure 5.11: Comparison of relative wave amplitudes when h_{10} are varied along the y-axis

when we set $h_{10} = 2.4$, half of the reference cylinder height, $h_{10} = 4.8$, we can see that, the relative wave amplitude was decreasing with the decrease of the cylinder height. On the other hand, when the height of the cylinder is 1/2 times higher than the reference cylinder, the relative amplitude also becomes bigger in the disturbance area. This shows that, the refractive and diffractive effects become stronger when we place a bigger obstacle in front of the waves, resulting in a bigger relative amplitude in the lee region.

5.3.4 *Topographic and radius Effects*

After observing the effects of the relative wave amplitude with various values of h_{10}, it is interesting to examine the effects of the wave refraction when the dimension of the bottom topography and the radius of the cylinder are varied.

In Figs. 5.12, and 5.13 we plot the relative wave amplitudes along the $x-$ and $y-$axes for different hump and cylinder radii, $b/L = 0.25$, 0.5, and 1.0 with a fixed $d = 0.25$ and $h_{10} = h_{20} = 4.8$, respectively.

As the radius of the hump, b/L is increased, the relative wave amplitude inside and outside the cylinder also increased as can be seen along the x- and y- axes. This is due to the concentration of wave energy in the lee region of an obstacle, as a result of refractive and diffractive focusing, when the disturbance of the obstacle is sufficiently large. However, for a small hump radius no waves are found inside the cylinder because the latter is smaller than the wavelength, as can be clearly seen in both figures.

Next, we discuss the effects of the wave refraction when the height of the hump, d is varied. Fig. 5.14 and Fig. 5.15 show the relative wave amplitude along the $x-$ and y- axes, respectively, for the cases of $d = 0.05$, 0.25, and 0.5 with the hump radius being fixed at $b/L = 0.5$, and $h_{10} = h_{20} = 4.8$. As

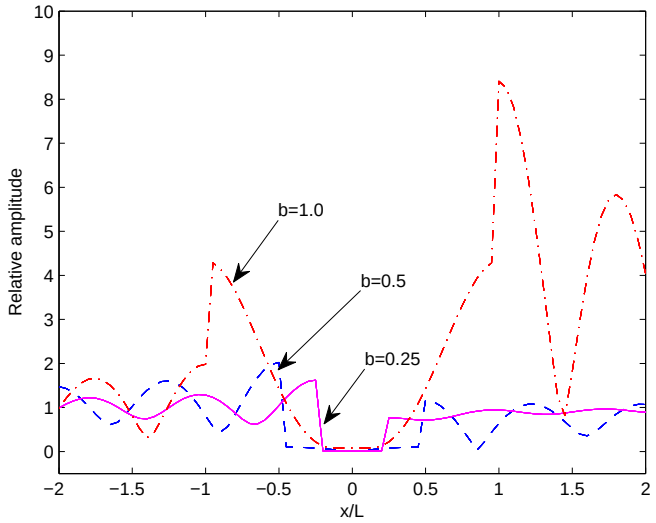

Figure 5.12: Comparison of relative wave amplitudes along the x-axis with b/L varied

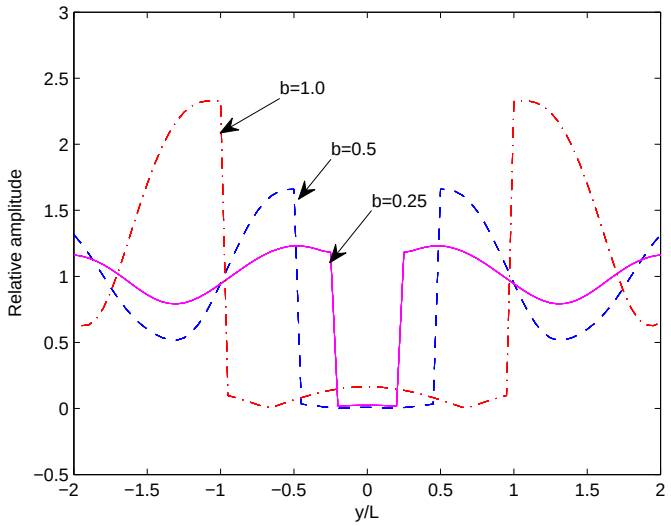

Figure 5.13: Comparison of relative wave amplitudes along the y-axis with b/L varied

can be clearly seen from Fig. 5.14 and Fig. 5.15, as the height of the hump increases, the relative wave amplitude becomes larger as expected.

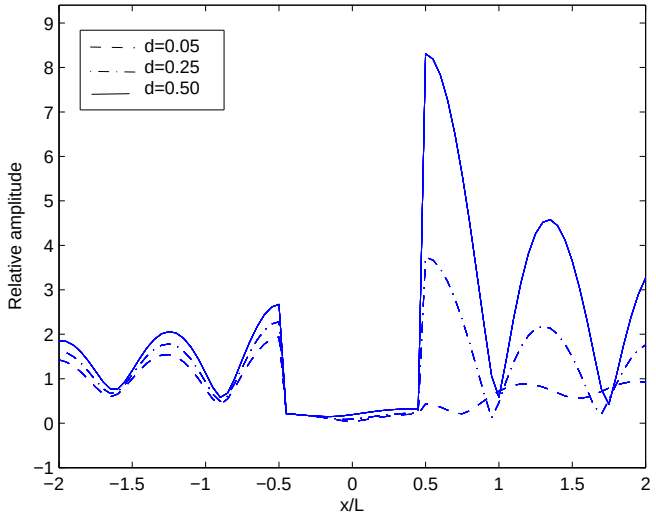

Figure 5.14: Comparison of relative wave amplitudes along the x-axis with d varied

For a hump with a smaller hump height, d, the refraction effects are weak, resulting in a smaller wave heights inside and outside the cylinder. On the other hand, for a higher hump height, d, there is more refractive focusing and thus the reaction to the disturbances behind the hump is larger in comparison with the lower d. For example, along the $x-$axis, as we increase the height of the hump, from 0.05 to 0.25, the maximum value of relative wave amplitude outside the cylinder obtained has increased too from 0.5 to 4.1, and if we further increase the hump height to 0.5, the maximum value of relative wave amplitude obtained is about 8.5. The same phenomenon occurs along the y-axis, as we can see that the increase of the hump height will also increase the relative wave amplitude outside the cylinder as well. Therefore, we can conclude that, the higher the hump high is, the bigger

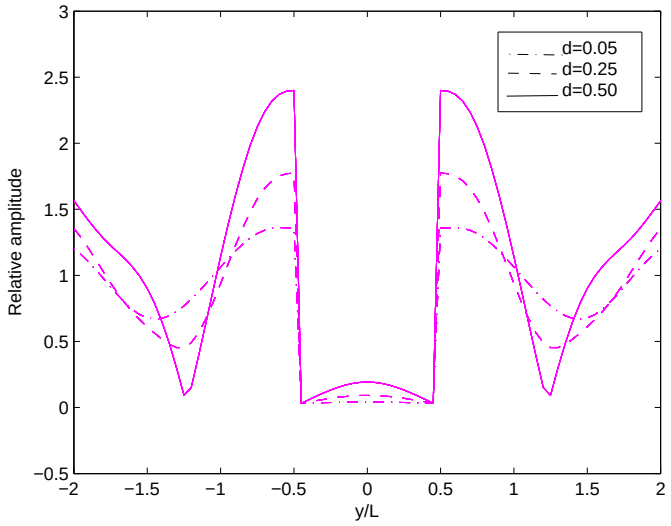

Figure 5.15: Comparison of relative wave amplitudes along the y-axis with d varied

is relative waves amplitude will observed. Hence, the OWC device should be installed in the shallow water, where waves would produce more energy through the diffraction, refraction and shoaling processes.

5.4 Conclusions

The two-layer mild-slope equation with free surface on the top has been derived and presented in this chapter. Utilizing this equation, we then solved the problem for circular hollow cylinder floating over a variable water depth. This analytic solution was derived based on the analytic solution of long waves propagating over a circular hump that have been presented earlier in Chapter 3 and Chapter 4.

To verify our solution, we have compared our solution with MacCamy and Fuchs solution [3] when our solutions were reduced to their case when $h_{20} = 0$.

The two solutions were identical and hardly distinguishable. To further verify our solution, we have also compared the solution for the flat bottom and the solution with very small hump size. Once again, both solutions were identical.

Furthermore, we have also examined and discussed the effects of the height of the cylinder, hump dimensions and cylinder radius to the wave refraction and diffraction when they are varied. When there is an increase in the obstacle, the diffraction and refraction effects become stronger, resulting in a bigger relative amplitudes. This is important for OWC industry because from this results, we can find the best place to install the OWC device.

Chapter 6

Conclusions

In this thesis, we have discussed and presented the analytic solutions for linear waves propagating in an ocean with variable bottom topography and their applications in renewable wave energy. We focus on the mild-slope equation, which is known as a powerful tool to study the diffraction and refraction problem in a linear wave theory. As already mentioned in Chapter 1 and 2, this equation has an advantage of reducing the three-dimensional model to a two-dimensional model. It also reduces to Hemholtz equation in a deep or constant water depth while in a shallow water, it reduces to the linear shallow water equation.

Therefore, in Chapter 3 of this thesis, we have presented an analytical solution for long waves refraction over a circular hump based on the mild-slope equation that has been reduced to the shallow water equation presented by Suh *et. al* [32] for the long waves propagating over a circular pit. We have made a comparison for both solutions, and found that along the $x-$axis, waves are amplified in front of the hump, whereas there is a relative calm region behind the pit. Numerical solution for this analytical solution is also constructed for the purpose of validation, and the comparisons between the

analytical and numerical solution were almost identical and hardly distinguishable. Using the new model, we were able to examine and discuss the effects of the hump dimension when the radius and the water depth are varied. From these tests, we can conclude that, the bigger or the higher the barrier or obstacle being placed, the bigger relative waves amplitude would be produced, meaning that there is a significantly large amount of energy presents in that area.

Furthermore, in Chapter 4, we have derived the mild-slope equation for a two-layer fluid model with the rigid-lid approximation used on the free surface. This analytic solution was derived based on the single-layer mild-slope equation obtained by Smith and Sprinks [1], and we have found that the single-layer mild-slope equation is the special case for a two-layer mild-slope equation when the density of the upper layer, ρ_1, equal to zero, meaning that the two-layer mild-slope equation should reduce to a single-layer mild-slope equation when $\rho_1 = 0$. The two-layer mild-slope equations is derived because, in the ocean, there exists a thin layer of water, separating the warmer surface zone and the colder deep zone. This thin layer is called the thermocline, across which the density as a function of the water temperature also jumps significantly [37]. Hence, two-layer ocean models with a sharp density interface separating fluids with two constant densities are very popular in modeling the dynamics of internal wave propagations in an ocean. Replacing the free surface with a rigid-lid approximation is reasonable in many cases, especially at the regional ocean scale, because "internal-wave mode" only induces small deformation on the free surface and thus a rigid-lid approximation would exclude the fast mode associated with barotropic free surface waves and greatly simplify the theoretical analysis without loss of a great deal of accuracy.

By using our new analytic solution, we then solved the problem as already discussed in Chapter 3, but now in a two-layer fluid. As what already been discovered in the earlier chapter, the bigger the hump size being placed on the ocean floor, the bigger relative waves amplitude will be induced. Furthermore, we have also examined and discussed the effects of the wave refraction when the ratio of densities, ρ_1/ρ_2, and the ratio of the upper and lower layer water depths, h_{10}/h_{20} are varied. Here, we found that when the ratio of densities, ρ_1/ρ_2, is increased, the relative waves amplitude decreases, while for the test of the h_{10}/h_{20}, the relative wave amplitude increases with the increase of h_{10}/h_{20}. Thus, in order to find a suitable location to install an OWC device in the ocean, the place must have a low water density, because high level water density can't produce a bigger waves. In the other words, the water that has more density level, has a weaker restoring force, resulting in a smaller waves amplitude.

We have also derived an extended mild-slope equation for the propagation of interfacial waves with higher-order terms proportional to the bottom slope and bottom curvature included in Chapter 4. Here, we found that the amplitude of the refracted waves calculated using the equation with the higher-order terms included is slightly higher than that calculated with the classical mild-slope equation.

Lastly in Chapter 5, we further extended the mild-slope equation by deriving the two-layer mild-slope equation with a free surface on the top. By utilizing this equation, we then solved the problem for a simple OWC problem, a circular hollow cylinder floating over a variable water depth. This analytic solution was derived based on the analytic solution for long waves propagating over a circular hump that has been presented earlier in Chapter 3 and Chapter 4, which also included in our papers [11, 12, 13]. To verify our

solution, we have compared our solution with MacCamy and Fuchs solution [3] when our solution reduced to their case when $h_{20} = 0$. The two solutions were identical and hardly distinguishable. To further verify our solution, we have also compared the solution with the flat bottom and the solution with a very small hump size. Once again, both solutions were identical. Furthermore, we have also examined and discussed the effects of the height of the cylinder, hump dimensions and cylinder radius to the wave refraction and diffraction when they are varied. When there is an increase in the obstacle, the diffraction and refraction effects become stronger, resulting in a bigger relative amplitude in the disturbance area.

As already known, waves in the ocean are random and nonlinear. But, the linear model is a good approximation in understanding the ocean waves, before deriving the nonlinear model. This is because the nonlinear model requires more complicated equations. However, in the near future, it is possible to solve the nonlinear mild-slope equation using the same problem as we have done with the linear regime. It is also possible to make another bottom topography and floating object both in linear and nonlinear regime to solve the refraction and diffraction problem using analytical solution.

Appendix A

Elevations of the Inner Products

Some evaluations of the inner products and products of wave numbers in Chapter 3 are listed here:

$$\begin{aligned} I_1^{(1)} &= < f_{1,0}, \frac{\partial^2 f_{1,0}}{\partial h_1^2} > \\ &= \frac{1}{2(sinh^2(kh_1))^2}[kcosh(kh_1)(sinh(kh_1) - sinh(kh_1)cosh(2kh_1) \\ &\quad cosh(kh_1)sinh(2kh_1) + 2kh_1 cosh(kh_1))] \end{aligned} \tag{A.1}$$

$$\begin{aligned} I_1^{(2)} &= < f_{1,0}, \frac{\partial^2 f_{1,0}}{\partial k^2} > \\ &= \frac{1}{8k^3(sinh^2(kh_1)^2}[sinh(kh_1)(sinh(2kh_1) - 2kh_1 cosh(2kh_1)) \\ &\quad + \frac{(2kh_1)^3}{3}(1 + 2cosh^2(kh_1)) \\ &\quad + kh_1 sinh(2kh_1)(2kh_1 + sinh(2kh_1))] \end{aligned} \tag{A.2}$$

$$
\begin{aligned}
I_1^{(3)} &= < f_{1,0}, \frac{\partial^2 f_{1,0}}{\partial h_1 \partial k} > \\
&= \frac{1}{16k(sinh^2(kh_1)^2}[-2kh_1 sinh(2kh_1) + 2 - 2cosh^2 2(kh_1) \\
&\quad +12(kh_1 cosh(kh_1))^2 + (2kh_1)^2 - 2cosh(2kh_1) \\
&\quad -(sinh(2kh_1)^2 + 8kh_1 cosh^2(kh_1) sinh(2kh_1) \\
&\quad -4kh_1 sinh(2kh_1) cosh(2kh_1) + 2cosh^2(kh_1) cosh(2kh_1)] \qquad \text{(A.3)}
\end{aligned}
$$

$$
\begin{aligned}
I_1^{(4)} &= < f_{1,0}, \frac{\partial f_{1,0}}{\partial k} > \\
&= -\frac{1}{8k^2 sinh^3(kh_1)}(-2kh_1 sinh(kh_1) cosh(2kh_1) + 4k^2 h_1^2 cosh(kh_1) \\
&\quad +sinh(kh_1) sinh(2kh_1) + 2kh_1 cosh(kh_1) sinh(2kh_1)) \qquad \text{(A.4)}
\end{aligned}
$$

$$
\begin{aligned}
I_1^{(5)} &= < f_{10}, \frac{\partial f_{1,0}}{\partial h_1} > \\
&= -\frac{1}{4sinh^3(kh_1)}(-sinh(kh_1) cosh(2kh_1) + cosh(kh_1) cosh(2kh_1) \\
&\quad +sinh(kh_1) + 2kh_1 cosh(kh_1)) \qquad \text{(A.5)}
\end{aligned}
$$

$$
\begin{aligned}
I_2^{(1)} &= < f_{2,0}, \frac{\partial^2 f_{2,0}}{\partial h_2^2} > \\
&= \frac{1}{2(sinh^2(kh_2))^2}[kcosh(kh_2)(sinh(kh_2) - sinh(kh_2) cosh(2kh_2) \\
&\quad cosh(kh_2) sinh(2kh_2) + 2kh_2 cosh(kh_2))] \qquad \text{(A.6)}
\end{aligned}
$$

$$
\begin{aligned}
I_2^{(2)} &= < f_{2,0}, \frac{\partial^2 f_{2,0}}{\partial k^2} > \\
&= \frac{1}{8k^3(sinh^2(kh_2)^2}[sinh(kh_2)(sinh(2kh_2) - 2kh_2 cosh(2kh_2)) \\
&\quad +\frac{(2kh_2)^3}{3}(1 + 2cosh^2(kh_2)) \\
&\quad +kh_2 sinh(2kh_2)(2kh_2 + sinh(2kh_2))] \qquad \text{(A.7)}
\end{aligned}
$$

$$
\begin{aligned}
I_2^{(3)} &= < f_{2,0}, \frac{\partial^2 f_{2,0}}{\partial h_2 \partial k} > \\
&= \frac{1}{16k(sinh^2(kh_2)^2}[-2kh_2 sinh(2kh_2) + 2 - 2cosh^2 2(kh_2) \\
&\quad +12(kh_2 cosh(kh_2))^2 + (2kh_2)^2 - 2cosh(2kh_2) \\
&\quad -(sinh(2kh_2)^2 + 8kh_2 cosh^2(kh_2) sinh(2kh_2) \\
&\quad -4kh_2 sinh(2kh_2) cosh(2kh_2) + 2cosh^2(kh_2) cosh(2kh_2)] \qquad \text{(A.8)}
\end{aligned}
$$

$$
\begin{aligned}
I_2^{(4)} &= < f_{2,0}, \frac{\partial f_{2,0}}{\partial k} > \\
&= -\frac{1}{8k^2 sinh^3(kh_2)}[-2kh_2 sinh(kh_2) cosh(2kh_2) + 4(kh_2)^2 cosh(kh_2) \\
&\quad +sinh(kh_2) sinh(2kh_2) + 2kh_2 cosh(kh_2) sinh(2kh_2)] \qquad \text{(A.9)}
\end{aligned}
$$

$$
\begin{aligned}
I_2^{(5)} &= < f_{2,0}, \frac{\partial f_{2,0}}{\partial h_2} > \\
&= \frac{1}{4sinh^3(kh_2)}[sinh(kh_2)(1 - cosh(2kh_2)) \\
&\quad +cosh(kh_2)(2 + sinh(2kh_2))] \qquad \text{(A.10)}
\end{aligned}
$$

$$\chi_{1,0} = k^2(\rho_1 - \rho_1 coth^2(kh_1)) \tag{A.11}$$

$$\chi_{2,0} = k^2(\rho_2 - \rho_2 coth^2(kh_2)) \tag{A.12}$$

$$\begin{aligned}
\chi_{3,0} &= \frac{2k^3\rho_1}{sinh^2(kh_1)}(kh_1\rho_1^2q_1^4 + 2\rho_1^2q_1^3 + 3\rho_1\rho_2q_1^2q_2 - \rho_1\rho_2k^2h_2^2q_1^2q_2 \\
&+ \rho_1\rho_2k^2h_2^2q_1^2q_2^3 - 3\rho_1\rho_2kh_2q_1^2 + 3\rho_1\rho_2kh_2q_1^2q_2^2 \\
&- 2\rho_1^2kh_1q_1^2 - 2\rho_2^2k^2h_2^2q_1q_2^2 - 2\rho_2^2kh_2q_1q_2 + \rho_2^2q_1q_2^2 \\
&+ k^2\rho_2^2h_2^2q_1 + \rho_2^2k^2h_2^2q_1q_2^4 + 2kh_2\rho_2^2q_1q2^3 - \rho_1^2q_1 + \rho_1\rho_2k^2h2^2q_2 + \rho_1\rho_2kh_2 \\
&+ \rho_1^2kh_1 - \rho1\rho_2kh_2q_2^2 - \rho_1\rho_2k^2h_2^2q_2^3 - \rho_1\rho_2q_2)
\end{aligned} \tag{A.13}$$

$$\begin{aligned}
\chi_{4,0} &= \frac{2k^3\rho_2}{sinh^2(kh_1)}(kh_2\rho_2^2q_2^4 + 2\rho_2^2q_2^3 + 3\rho_1\rho_2q_2^2q_1 - \rho_1\rho_2k^2h_1^2q_2^2q_1 \\
&+ \rho_1\rho_2k^2h_1^2q_2^2q_1^3 - 3\rho_1\rho_2kh_2q_2^2 + 3\rho_1\rho_2kh_1q_1^2q_2^2 \\
&- 2\rho_2^2kh_2q_2^2 - 2\rho_1^2k^2h_1^2q_2q_1^2 - 2\rho_1^2kh_1q_1q_2 + \rho_1^2q_2q_1^2 \\
&+ k^2\rho_1^2h_1^2q_2 + \rho_1^2k^2h_1^2q_2q_1^4 + 2kh_1\rho_1^2q_2q1^3 - \rho_2^2q_2 + \rho_1\rho_2k^2h1^2q_1 + \rho_1\rho_2kh_1 \\
&+ \rho_2^2kh_2 - \rho1\rho_2kh_1q_1^2 - \rho_1\rho_2k^2h_1^2q_1^3 - \rho_1\rho_2q_1)
\end{aligned} \tag{A.14}$$

$$\begin{aligned}
\chi_{5,0} &= \frac{4k^3\rho_1\rho_2}{\sinh^2(kh_1)\sinh^2(kh_2)}(\rho_1k^2h_1h_2q_1^2q_2 \\
&+ \rho_2h_1h_2k^2q_1q_2^2 + \rho_2kh_1q_1q2 + \rho_1kh_2q_1q2 - \rho_1q_1 \\
&- \rho_2k^2h_1h_2q_1 - \rho_1k^2h_1h_2q_2 - \rho_2q_2 + k(\rho_1h_1 + \rho_2h_2))
\end{aligned} \tag{A.15}$$

$$\begin{aligned}
\chi_0 &= \rho_1coth(kh_1) + \rho_2coth(kh_2) - k\rho_1h_1 + k\rho_1h_1coth^2(kh_1) \\
&- k\rho_2h_2 + k\rho_2h_2coth^2(kh_2)
\end{aligned} \tag{A.16}$$

where

$$q_1 = coth(kh_1) \tag{A.17}$$

$$q_2 = coth(kh_2) \tag{A.18}$$

Appendix B

Calculation of the Limit

The calculation of limit involving in Chapter 5 is presented here.

For small r, the argument for the Bessel Function of the first kind $J_n(kr)$ and Bessel Function for the second kind $Y_n(kr)$ is given by [60]

$$Y_0(kr) \sim \frac{2}{\pi}\ln r \tag{B.1}$$

$$Y_n(kr) \sim \frac{-2^n(n-1)!}{\pi r^n} \tag{B.2}$$

$$J_n(kr) \sim \frac{r^n}{2^n n!} \tag{B.3}$$

We want to show that,

$$\lim_{r\to 0} \quad Y_n(kr)\int_0^r \frac{\pi r B_n R_n(r) J_n(kr)}{2} dr = 0 \tag{B.4}$$

$$J_n(kr)\int_0^r \frac{\pi r B_n R_n(r) Y_n(kr)}{2} dr = 0 \tag{B.5}$$

But, we know that the limit for these equations are

$$\lim_{r\to 0} Y_n(kr)\int_0^r \frac{\pi r B_n R_n(r) J_n(kr)}{2} dr = \infty \cdot 0 \tag{B.6}$$

$$\lim_{r\to 0} J_n(kr)\int_0^r \frac{\pi r B_n R_n(r) Y_n(kr)}{2} dr = 0 \cdot \infty \tag{B.7}$$

By using the L'hopital rule, and substituting Eq. (B.2), into Eq. (B.6), and let $f(r) = \int_0^r \frac{\pi r B_n R_n(r) J_n(kr)}{2}$, we have

$$\begin{aligned}
\lim_{r\to 0} Y_n(kr) \int_0^r \frac{\pi r B_n R_n(r) J_n(kr)}{2} dr &= \lim_{r\to 0} \frac{-2^n(n-1)!}{\pi r^n} \int_0^r f(r)dr \\
&= \frac{-2^n(n-1)!}{\pi} \lim_{r\to 0} \frac{1}{r^n} \int_0^r f(r)dr \\
&= \frac{-2^n(n-1)!}{\pi} \lim_{r\to 0} \frac{\int_0^r f(r)dr}{r^n} \\
&= \frac{-2^n(n-1)!}{\pi} \lim_{r\to 0} \frac{D[\int_0^r f(r)dr]}{D[r^n]} \\
&= \frac{-2^n(n-1)!}{\pi} \lim_{r\to 0} \frac{f(r)dr}{nr^{n-1}} \\
&= \frac{-2^n(n-1)!}{\pi} \lim_{r\to 0} \frac{B_n R_n(r) r^{n+1} \frac{\pi}{2\cdot 2^n n!}}{nr^{n-1}} \\
&= \frac{-2^n(n-1)!}{\pi} \lim_{r\to 0} B_n R_n(r) r^2 \frac{\pi}{2\cdot 2^n n! n} \\
&= 0 \qquad \text{(B.8)}
\end{aligned}$$

Utilizing the same approach as we use in Eq. (B.6, in Eq. (B.7 and let $F(r) = \int_0^r \frac{\pi r B_n R_n(r) Y_n(kr)}{2}$, we obtain

$$
\begin{aligned}
\lim_{r\to 0} J_n(kr)\int_0^r F(r)dr &= \lim_{r\to 0}\frac{r^n}{2^n n!}\int_0^r F(r)dr \\
&= \frac{1}{2^n n!}\lim_{r\to 0} r^n \int_0^r F(r)dr \\
&= \frac{1}{2^n n!}\lim_{r\to 0}\frac{r^n}{\frac{1}{\int_0^r F(r)dr}} \\
&= \frac{1}{2^n n!}\lim_{r\to 0}\frac{D[r^n]}{D[\frac{1}{\int_0^r F(r)dr}]} \\
&= \frac{1}{2^n n!}(\frac{B_n(-2^n(n-1)!)}{2})\lim_{r\to 0} r^{n-1}\frac{r}{r^n}R_n(r) \\
&= \frac{1}{2^n n!}(\frac{B_n(-2^n(n-1)!)}{2})\lim_{r\to 0} R_n(r) \\
&= [\frac{1}{2^n n!}(\frac{B_n(-2^n(n-1)!)}{2})][0] \\
&= 0 \qquad\qquad (B.9)
\end{aligned}
$$

Appendix C

Derivation for Equation (5.20)

The derivation of Eq. (5.20) in Chapter 5 is presented here.

From Eq. (5.15) and (5.16) we know that

$$Z_1 = k\ \cosh(kz) + K\ \sinh(kz), \qquad -h_1 \leq z \leq 0 \tag{C.1}$$

$$Z_2 = \frac{K\cosh(kh_1) - k\ \sinh(kh_1)}{\sinh(kh_2)}\cosh(k(z+h)), \qquad -h \leq z \leq -h_1 \tag{C.2}$$

At the interface, we have

$$\phi_1(x,y,z) = \phi_2(x,y,z), \qquad z = -h_1 \tag{C.3}$$

Substituting Eqs. (5.18) and (5.19) into Eq. (C.3), we have

$$\frac{\eta_f}{\eta_i} = \frac{K}{k\sinh(kh_1) - K\cosh(kh_1)} \tag{C.4}$$

which is the relationship between η_f and η_i.

Appendix D

Publications of the Author

1. S.-P. Zhu and F.N. Harun, An analytical solution for long wave refraction over a circular hump, *J. Appl. Math Comput* (2009) 30: 315-333

2. S.-P. Zhu and F.N. Harun, Refraction of interfacial waves by a circular hump, *Journal of Engineering and Computational Mechanics* (2009) (Accepted and In Press)

3. F.N. Harun and S.-P. Zhu, A study of the propagation of interfacial waves over a circular hump, *Proceedings of the 5th Asian Mathematical Conference, Malaysia* (2009) (In Press)

4. F.N. Harun and S.-P. Zhu, An analytical solution for a hollow cylinder floating in a variable water depth. (In preparation)

Bibliography

[1] R. Smith and T. Sprinks. Scattering of surface waves by a conical island. *J. Fluid Mech.*, 72:373–384, 1975.

[2] S.R. Massel. Extended refaraction-diffraction equation for surface waves. *Coastal Eng.*, 19:97–126, 1993.

[3] R.C. MacCamy and R.A. Fuchs. Wave forces on piles: A diffraction theory. *US Army Corps of Engineering, Beach erosion Board, Washington DC, Technical Memorandum*, 69, 1954.

[4] C.C. Mei. *The Applied Dynamics of Ocean Surface Waves.* World Scientific, Singapore, 1989.

[5] R.G. Dean and R.A. Dalrymble. *Water Wave Mechanics for Engineers and Scientists.* Singapore ; Teaneck, NJ : World Scientific, 1991.

[6] H.W. Liu. *Numerical modeling of the propagation of ocean waves.* PhD thesis, University of Wollongong, 2001.

[7] E.L Geist, V.V. Titov, and C.E. Synolakis. Tsunami: Wave of change. *Scientific American*, pages 56–63, 2005.

[8] C.E Synolakis and Bernard E.N. Tsunami science before and beyond boxing day 2004. *Phil. Trans. R. Soc. A*, 364:2231–2265, 2006.

[9] J.C.W. Berkhoff. Computational of combined refraction-diffraction. *Proc. 13th Coastal Engng Conf., Vancouver, A.S.C.E.*, 1:471–490, 1972.

[10] I.G Jonsson, O. Skovgaard, and O. Brink-Kjaer. Diffraction and refraction calculations for waves incident on an island. *J. Marine Res.*, 34-3:469–494, 1976.

[11] S.-P. Zhu and F.N. Harun. An analytical solution for long wave refraction over a circular hump. *J. Appl. Maths. and Comput*, 30:315–333, 2009.

[12] S.-P. Zhu and F.N. Harun. Refraction of interfacial waves by a circular hump. *Journal of Engineering and Computational Mechanics, (Accepted and In Press)*, 2009.

[13] F.N. Harun and S.-P. Zhu. A study of the propagation of interfacial waves over a circular hump. *Proceedings of the 5th Asian Mathematical Conference, Malaysia (In Press)*, 2009.

[14] H. Martin-rivas and C.C. Mei. Wave power extraction from an oscillating water column along a straight coast. *Ocean Engineering*, 36:429–433, 2009.

[15] H. Martin-rivas and C.C. Mei. Wave power extraction from an oscillating water column at the tip of a break water. *Journal of Fluid mechanics*, 626:395–414, 2009.

[16] N. Sharmila, P. Jalihal, A.K. Swamy, and M. Ravindran. Wave powered desalination system. *Energy*, 29:1659–1672, 2004.

[17] G. Benassai. *Introduction to coastal dynamics and shoreline protection.* WIT Press, 2006.

[18] C. Eckart. The propagation of gravity waves fromm deep to shallow water. *National Bureau of Standards, Circular*, 20:165–173, 1952.

[19] I.A Svendsen. The wave equation for gravity waves in water of gradually varying depth. *ISVA, Techn. Univ. of Denmark, Basic Research Progress Report*, 15:2–7, 1967.

[20] J.C. Schonfeld. Propagation of two dimensional short waves. *Delft University of Technology Manuscript (in Dutch)*, 1972.

[21] C.J. Lozana and R.E. Meyer. Leakage and response of waves trapped round islands. *Phys. Fluids*, 19:1075–1088, 1976.

[22] N. Booij. A note on the accuracy of the mild-slope equation. *Coastal Engineering*, 7:191–203, 1983.

[23] S. Homma. On the behaviour of seismic sea waves around circular island. *Geophys. Mag.*, XXI:199–208, 1950.

[24] P. Bettess and O.C. Zienkiewicz. Diffraction and refraction of surface waves using finite and infinite elements. *Int. J. Numer. Methods Eng.*, 11:1271–1290, 1977.

[25] Y. Zhang and S.-P. Zhu. New solutions for the propagation of long water waves over variable depth. *J. Fluid Mech.*, 278:391–406, 1994.

[26] S.-P. Zhu and Y. Zhang. Scattering of long wave s around a circular island mounted on a conical shoal. *Wave Motion*, 23:353–362, 1996.

[27] Y.Z. Miropol'sky. *Dynamics of Internal Gravity Waves in the Ocean*. Springer, 2001.

[28] Y. Ito and K. Tanimoto. A method of numerical analysis of wave propagation-application to wave diffraction and refraction. *Proc. 13th Coastal Engng Conf., Vancouver, A.S.C.E.*, 1, 1972.

[29] R.G. Williams, J. Darbyshire, and Holmes P. Wave refraction and diffraction in a caustic region: A numerical solution and experimental validation. *Proc. Instn. Civ. Engrs, Part 2*, 69:635–649, 1980.

[30] V. G. Panchang, B.R. Pearce, and M.J. Briggs. Numerical simulations of irregular waves propagating over shoal. *J. Waterway, Port, Coastal and Ocean Engng*, 116(3):324–340, 1990.

[31] A. Chawla, H.T. Ozkan-Heller, and J.T. Kirby. Experimental study of breaking waves over a shoal. *Proc. Int. Coastal Eng., Orlando, Florida*, 25:2–15, 1996.

[32] K.-D. Suh, T.-H. Jung, and M.C. Haller. Long waves propagating over a circular pit. *Wave Motion*, 42:143–154, 2005.

[33] H. Lamb. *Hydrodynamics*. Cambridge : Cambridge University Press, sixth edition, 1993.

[34] G.J.M. Copeland. A practical alternative to the mild slope equations. *Coast. Eng*, 9:125–149, 1985.

[35] F.B. Hildebrand. *Advanced Calculus for Applications*. Prentice-Hall, Englewood Cliff, New Jersey, second edition, 1976.

[36] V.W. Ekman. On dead water. *Scientific Results of the Norwegian North Polar Expedition 1893-1896*, 5(15):1–152, 1904.

[37] J. Roberts. *Internal Gravity Waves in the Ocean*. Marcel Dekker, Inc., 1975.

[38] Y. Yutang, L. Jiachun, and Youliang C. Validity ranges of interfacial wave theories in a two-layer fluid system. *Acta. Mech. Sin.*, 23:597–607, 2007.

[39] G G. Stokes. On the theory of oscillatory waves. *Trans. Camb. Phil. Soc. (Reprinted in Mathematical and Physical Papers 1, 314-326)*, 8:441–455, 1847.

[40] G.H. Keulegan. Characteristic of internal solitary waves. *J. Res. Natl. Bur. Stand*, 51:133, 1953.

[41] R.R. Long. Solitary waves in one- and two-fluid systems. *Tellus*, 8:460, 1956.

[42] T.B. Benjamin. Internal waves of permanent form in fluids of great depth. *J. Fluid Mech*, 146:559–592, 1967.

[43] D. Kelly. Waves beneath the sea. *Association of Science Teachers Journal*, 3, 2002.

[44] C. Garret and W. Munk. Internal waves in the ocean. *Ann. Rev. Fluid Mech*, 11:339–69, 1979.

[45] P.G. Chamberlain and D. Porter. The modified mild-slope equation. *J. Fluid Mech*, 291:393–407, 1995.

[46] D. Porter and D.J. Staziker. Extensions of the mildslope equation. *J. Fluid Mech*, 300:367–382, 1995.

[47] D. Porter. The mild-slope equation. *J. Fluid Mech*, 494:51–63, 2003.

[48] P.G. Chamberlain and D. Porter. Wave scattering in a two-layer fluid of varying depth. *J. Fluid Mech.*, 524:207–228, 2005.

[49] C.M. Liu. Parametric study on random internal waves in a two-fluid system. *Symposium on Underwater Technology and Workshop on Scientific Use of Submarine Cables and Related Technologies*, pages 83–86, 2007.

[50] N.N. Panicker. Power resource potential of ocean surface waves, 1976.

[51] J. Falnes. A review of wave-energy extraction. *Marine Structures*, 20:185–201, 2007.

[52] C.J.R. Garret. Bottomless harbour. *Journal of Fluid Mechanics*, 43(3):433–449, 1970.

[53] D.V. Evans. The oscillating water column wave energy device. *J. Inst. Math. Appl*, 22:423–433, 1978.

[54] D.V. Evans. Wave-power absorption by sytems of oscillating surface pressure distributions. *Journal of Fluid Mechanics*, 114:481–99, 1982.

[55] C.M. Smith. *Some problems in linear water waves*. PhD thesis, University of Bristol, 1983.

[56] A.J.N.A Sarmento and A.F De O. Falc$\widetilde{a}$o. Wave generation by an oscillating surface-pressure and its application in wave-energy extraction. *Journal of Fluid Mechanics*, 150:467–485, 1985.

[57] A.F. de O. Falc$\widetilde{a}$o and R.J.A. Rodrigues. Stocastic modelling of owc wave power plant performance. *Applied Ocean Research*, 24:59–71, 2002.

[58] A.F. de O. Falc$\widetilde{a}$o. Control of an oscillating-water-column wave power plant for maximum energy production. *Applied Ocean Research*, 24:73–82, 2002.

[59] A. Sommerfeld. *Partial Differential Equations in Physics*, volume 4. Academic Press INC, 1964.

[60] M. Abramowitz and I.A. Stegun. *Handbook of mathematical functions, with formulas, graphs, and mathematical tables*. Washington, U.S. Govt. Print. Off, 1964.